

Emission reduction by targeted transient λ operations in three-way catalysts for heavy-duty natural gas applications

Présentée le 18 août 2022

Faculté des sciences de base
Groupe Kröcher
Programme doctoral en chimie et génie chimique

pour l'obtention du grade de Docteur ès Sciences

par

Moyu WANG

Acceptée sur proposition du jury

Prof. A. Züttel, président du jury
Prof. O. Kröcher, Dr P. Dimopoulos Eggenschwiler, directeurs de thèse
Prof. G. Groppi, rapporteur
Dr D. Tsinoglou, rapporteur
Prof. C. Onder, rapporteur

Acknowledgements

This PhD thesis was conducted in the laboratory for Automotive Powertrain Technologies at Empa, Swiss Federal Laboratories for Materials Science and Technology.

First of all, I would like to express my gratitude to my supervisor Dr. Panayotis Dimopoulos Eggenschwiler for giving me this excellent opportunity and supervising my entire work. His life and work philosophies have influenced me a lot during the years. Also, I would like to give my special thank to Prof. Krocher for accepting me as a PhD candidate. His dedication to details has pushed the work forward in scientific aspects. I would like to thank Christian Bach, our laboratory head for his support and trust.

I would like to give special thanks to my colleague Roland Graf. His expertise and dedication to the engine test bench has made the complex measurements possible. I would also like to thank Dr. Norbert Zsiga for his support on experiments planning and engine controllers. Special thanks to Daniel Schreiber, whose expertise in engineering design and implementation has helped me through all my experiments. I also thank Jacqueline Tschudin, who helped me with catalyst preparation and microscopy images. My thanks also go to Roland Spühler and Hugo Ehrensperger, who supported on gas supply and setup installations. My special thanks go to all scientific collaborators I have worked with, Dr. Tanja Franken, Dr. Davide Ferri and Dr. Miren Agote Arán for their support in lab-scale experiments and fruitful discussions.

I would like to thank my office mates: Justin Plogmann, Arthur Couteau and Viola Papetti, for supporting each other in office talks, in ski areas and in bouldering halls. I thank also my roommates at Dietikon for many cheerful dinners and discussions on our PhD life. My special thanks to my boyfriends, who accompanied me in many extreme trips. Last but not least, I would like to thank my family for their support and encouragement through all my study years.

Abstract

To curb the severe effects of climate change, our society needs to radically reduce its CO₂ footprint. For the heavy-duty sector, where electrification is difficult, alternative fuels can be the solution. Methane-fueled engines have lower energy-specific CO₂ emissions than conventional Diesel-fueled engines. Furthermore, they have the potential of becoming carbon-neutral, when combined with bio-methane/synthetic methane. However, oxidation of unburnt methane in the exhaust gas poses a challenge for after-treatment systems. The aim of this thesis is to investigate the mechanism of methane abatement and to reveal methods to reduce methane and other hazardous gas emissions. The majority of the experiments were conducted directly on an engine test bench, which is rarely seen in studies focusing on catalytic reaction pathways.

Initial investigations focused on methane abatement under steady state and λ -step transitions. Under steady state, the presence of oxygen was identified as a prerequisite for methane conversion. Reacting with oxygen is the only methane conversion pathway. However, after step transition from oxygen excess conditions (slightly lean) to oxygen-poor conditions (slightly rich), high methane conversion was observed under rich conditions with no oxygen available. This high conversion was attributed to steam reforming (SR), which was activated by the step transition. The SR reaction rate decreased over time when staying at rich conditions, until full deactivation. Investigations in the lab-scale model gas reactor confirmed this analysis. In addition, the reason for SR deactivation was identified by DRIFTS measurements as the accumulation of carbonates on the catalytic surface, blocking the active sites.

Based on the identified importance of the SR reaction, targeted λ oscillations across stoichiometry were introduced, in order to repeatably activate SR and achieve sustainable high methane conversion. During the rich parts of the oscillations, methane was converted via SR, while, during lean parts, the carbonates were periodically removed from the catalyst surface. With these oscillations, methane conversion has been significantly improved, in comparison to steady state. In parallel, a numerical model has been developed in order to simulate the catalyst behavior under oscillating conditions. The model provided insights on the reaction pathways and their distribution along the catalyst axis.

The catalytic activity of the different Platinum-group metals has been investigated for the identified reactions. Various catalysts of different compositions were tested under cold start, λ oscillations and quasi-steady state conditions. Both Pt and Pd activated SR reactions, however SR attenuation was faster in Pt catalysts. In lean conditions, Pt exhibited higher methane oxidation. Rh was identified as important for enhancing NO_x reduction and lowering NH₃ emissions. The combination of all three metals has improved the overall catalyst performances.

In the final part of the thesis, a special aftertreatment system was investigated. It combines a Pd/Rh catalyst subject to stoichiometric conditions with a Pt oxidation catalyst subject to lean conditions. In the Pd/Rh catalyst, methane was removed via λ oscillations. In the Pt catalyst, the remaining CO, H₂ and NH₃ were oxidized. The setup provided a novel perspective in reducing the overall environmental impacts.

Keywords

Natural gas engine, three-way catalyst, methane oxidation, steam reforming, lean/rich oscillations, Palladium, Platinum, Rhodium

Zusammenfassung

Um die gravierenden Auswirkungen des Klimawandels einzudämmen, muss der CO₂-Fußabdruck radikal reduziert werden. Für den Schwerlastsektor, wo die Elektrifizierung schwierig ist, können alternative Kraftstoffe eine gute Lösung darstellen. Mit Methan betriebene Motoren haben geringere energiespezifische CO₂-Emissionen als Dieselmotoren. Außerdem haben sie das Potenzial, CO₂-neutral zu sein, wenn sie mit Biomethan/synthetischem Methan kombiniert werden. Allerdings stellt die Oxidation von unverbranntem Methan im Abgas eine Herausforderung dar. Ziel dieser Arbeit ist es, die Mechanismen der Methanreduktion zu untersuchen und Methoden zur Verringerung von Methan- und anderen Schadstoffemissionen aufzuzeigen. Die meisten Experimente wurden direkt auf einem Motorprüfstand durchgeführt, was bei Studien, die sich mit katalytischen Reaktionswegen befassen, selten der Fall ist.

Zunächst wurde die Methanreduktion beim stationären Motorbetrieb und bei definierten λ -Sprungübergängen untersucht. Im stationären Betrieb wurde die Anwesenheit von Sauerstoff als Voraussetzung für Methanumwandlung identifiziert. Die Reaktion mit Sauerstoff ist der einzige Methanumwandlungspfad. Beim Übergang vom Betrieb mit (leichtem) Sauerstoffüberschuss (mager) zu (leichtem) Sauerstoffmangel (fett) wurde jedoch eine hohe Methanumwandlung unter fetten Bedingungen ohne verfügbaren Sauerstoff festgestellt. Dieser erhöhte Umsatz wurde auf die Dampfreformierung (SR) zurückgeführt, die durch den Übergang aktiviert wurde. Die SR-Reaktionsrate nahm mit der Zeit ab, bis zur vollständigen Deaktivierung, wurde der Betrieb mit fettem Gemisch beibehalten. Untersuchungen in einem Modellgasreaktor bestätigten diese Analyse. Darüber hinaus wurde der Grund für die SR-Deaktivierung durch DRIFTS-Messungen auf die Bildung von Karbonaten auf der Oberfläche des Katalysators identifiziert.

Die festgestellte Bedeutung der SR Reaktion resultierte in der Auslegung von gezielten λ -Oszillationen, damit SR wiederholt aktiviert, und nachhaltig hohe Methanumsetzung erreicht werden können. In den fetten Abschnitten der Oszillationen wurde Methan über SR umgesetzt, während in den mageren die Karbonate von der Katalysatoroberfläche periodisch entfernt wurden. Durch diese Oszillationen wurde die Methanumwandlung im Vergleich zum stationären Zustand deutlich verbessert. Parallel dazu wurde ein numerisches Modell für das Verhalten des Katalysators unter oszillierenden Bedingungen entwickelt. Das Modell ermöglichte die Analyse von Reaktionswegen und deren Verteilung entlang der Katalysatorachse.

Die katalytische Aktivität von verschiedenen Platingruppenmetallen wurde bei den identifizierten Reaktionsmechanismen untersucht. Verschiedene Katalysatoren unterschiedlicher Zusammensetzung wurden unter Kaltstart-, λ -Oszillations- und Quasi-Stationärbedingungen getestet. Sowohl Pt als auch Pd haben die SR-Reaktion aktiviert, allerdings schwächte sich die SR bei Pt-Katalysatoren schnell ab. Unter mageren Bedingungen zeigte Pt eine stärkere Methan-Oxidation. Rh wurde als wichtig für die Verbesserung der NO_x-Reduktion und die NH₃ Senkung identifiziert. Die Kombination aller drei Metalle hat die Gesamtleistung des Katalysators verbessert.

Abschliessend wurde ein spezielles Nachbehandlungssystem untersucht. Es kombiniert einen Pd/Rh-Katalysator unter stöchiometrischen Bedingungen mit einem Pt-Oxidationskatalysator unter mageren Bedingungen. Im Pd/Rh-Katalysator wurde Methan mit λ -Oszillationen entfernt. Im Pt-Katalysator wurden die verbleibenden CO, H₂ und NH₃ oxidiert. Die Anordnung bietet eine neue Perspektive für die Verringerung der gesamten Umweltauswirkungen.

Schlüsselwörter

Erdgasmotor, Drei-Wege-Katalysator, Methanoxidation, Dampfreformierung, Mager/Fett-Oszillationen, Palladium, Platin, Rhodium

Contents

Acknowledgements	v
Abstract.....	vi
Keywords.....	vi
Zusammenfassung	vii
Schlüsselwörter	vii
List of Figures.....	xi
List of Tables.....	15
Chapter 1 Introduction	16
1.1 Engine emissions	16
1.1.1 Regulated and unregulated exhaust emissions.....	16
1.1.2 Current Emission standards (Europe, US and China) for heavy duty on-road vehicles	17
1.2 Catalytic emission abatement	17
1.2.1 Layouts of aftertreatment system.....	17
1.2.2 CH ₄ oxidation under lean conditions	18
1.2.3 CH ₄ direct oxidation and steam reforming at near stoichiometric conditions	18
1.2.4 N ₂ O and Ammonia formation.....	19
1.3 Modeling of catalytic processes.....	19
1.4 Aim and scope of the thesis.....	20
Chapter 2 Reaction pathways of methane abatement under steady and λ-step conditions	21
2.1 Experimentals	21
2.1.1 Engine test bench setup	21
2.1.2 SEM/EDX catalyst characterization	22
2.1.3 Steady state λ -sweep measurements	22
2.1.4 Transient λ -step measurements.....	22
2.1.5 Model gas reactor λ -step measurements	23
2.2 Results and Discussion.....	24
2.2.1 SEM/EDX characterization	24
2.2.2 Steady state λ -sweep	24
2.3 Conversion characteristics in lean to rich transitions	26

2.3.1	Engine test bench study	26
2.3.2	Model gas study	30
2.4	Conversion characteristics in rich to lean transitions	32
2.5	Conclusions	34
Chapter 3	Sustainable high methane conversion under periodic lean/rich oscillations	36
3.1	Experimental.....	36
3.2	Results of engine test bench measurements.....	36
3.2.1	General characteristics.....	36
3.2.2	Reaction schemes during a single oscillation period.....	38
3.2.3	Reaction schemes over multiple oscillation periods	40
3.2.4	Oscillations entirely on the rich side	40
3.2.5	Influence of different oscillation periods	41
3.3	Analysis of the chemical processes during the oscillations by means of simulations.....	45
3.3.1	Model setup	45
3.3.2	Modeling result of λ oscillations	48
3.4	Conclusions	50
Chapter 4	Roles of different noble metals	52
4.1	Experimental.....	52
4.1.1	Catalysts	52
4.1.2	Measurements on the engine test bench	52
4.1.3	Measurements on the model gas reactor	52
4.2	Results and Discussions	53
4.2.1	SEM washcoat characterization	53
4.2.2	λ ramp in the mid temperature range.....	53
4.2.3	λ ramp at low and high temperature	57
4.2.4	Analysis of low temperature behavior based on cold start and temperature ramps	58
4.2.5	Slow λ oscillation.....	60
4.2.6	Conversion characteristics of Pt/Pd/Rh catalyst	61
4.2.7	Optimization of λ oscillation in Pt/Pd/Rh catalyst.....	62
4.2.8	Optimized λ oscillation for the WHSC cycle	64
4.3	Conclusions	65
Chapter 5	Investigation of special catalysts layout in combination with pressure-wave charger.....	67
5.1	Experimentals	67
5.2	Results and discussions.....	68
5.3	Conclusions.....	70
Chapter 6	Conclusions and outlook	73
6.1	Achieved results	73

6.2	Future development	74
References.....		75
Curriculum Vitae.....		82

List of Figures

Figure 2:1 Scheme of transient λ -step measurements. Top: engine operation λ targets over time. Bottom: scheme of sliced catalyst system and measurement points 1 to 8.	23
Figure 2:2 a) SEM image of stage 2 ceramic catalyst, b) EDX Zirconium mapping, c) cerium mapping, and d) aluminum mapping of the marked area in a).	24
Figure 2:3 Concentration profiles of major species at different λ values recorded at measurement points numbered from 1 to 8 (Figure 2:1).	25
Figure 2:4 Relation between CH_4 conversion rate and a) oxygen concentration at the measurement points 2 and 3 and b) hydrogen concentration at measurement points 2, 3 and 4.	26
Figure 2:5 THC conversion rate of the complete aftertreatment system at different inlet temperatures (430°C, 520°C, 590°C and 660°C).	26
Figure 2:6 Concentration profiles at measurement points 1 to 8 during a λ -step from 1.03 to 0.98.	27
Figure 2:7 Transient λ -step from 1.03 to 0.98. a) Response of corrected λ , b)-d) transient concentration profiles and THC conversion rates for slices of the first stage catalyst.	28
Figure 2:8 Transient λ -step from 1.03 to 0.98. a) Response of corrected λ , b)-d) transient concentration profiles and THC conversion rate for slices of second stage catalyst.	28
Figure 2:9 THC conversion rate of stage 1 catalyst and the complete system (stage 1 and 2 catalysts) for different engine operating points with different inlet temperatures. The inlet temperature and mass flow rate of each operating points are listed as follow b) 430 °C, 63.1 kg/h, c) 520 °C, 103.1 kg/h, d) 590 °C, 144.2 kg/h, e) 660 °C, 251.0 kg/h, and f) 720 °C, 287.5 kg/h.	30
Figure 2:10 a) CH_4 conversion rates and concentrations of b) H_2 , c) O_2 and d) CO in the transient λ -steps in the model gas reactor.	31
Figure 2:11 a) DRIFTS spectra obtained during transient λ -step from lean to rich feed at 430°C, b) temporal signal intensities at 1595 cm^{-1} , 2053 cm^{-1} and 2169 cm^{-1} (after λ -step change at $t = 0$).	32
Figure 2:12 Concentration profiles at measurement points 1 to 8 during a λ -step from 0.98 to 1.03.	33
Figure 2:13 Transient λ -step from 0.98 to 1.03. a) Response of corrected λ , b)-d) transient concentration profiles and THC conversion rate for the slices of the second stage catalyst, e) H_2 concentration, and f) CO concentration.	34
Figure 3:1 a) λ sensor signal at measurement points 1 and 4, b-f) concentration of various species at measurement point 4 during periodic oscillation at $\lambda = 0.990 \pm 0.025$, with period = 10 s (lean/rich duration 5 s). The average concentration of species after 750 s are tabulated on the right side of each plot.	37
Figure 3:2 a) λ sensor signals and b) THC, c) CO, d) H_2 , and e) NH_3 concentration evolution in cycles after stabilization during periodic oscillation at $\lambda = 0.990 \pm 0.025$, with period = 10 s.	38
Figure 3:3 Scheme of typical THC concentration profile (W shape) with explanation. The rich to lean transition occurs at $t_{\text{norm}} = 0.5$	39
Figure 3:4 THC concentration profiles during one cycle (after stabilization at $t > 700$ s in Figure 3:1 at different measurement points during periodic oscillation at $\lambda = 0.990 \pm 0.025$, with period = 10 s (lean/rich duration 5 s).	39
Figure 3:5 THC concentration profiles at different times after the start of oscillations at $\lambda = 0.990 \pm 0.025$, with period = 10 s (lean/rich duration 5 s).	40
Figure 3:6 Inlet (m.p.1) and outlet (m.p.4) THC concentrations of oscillations with different average λ : a) $\lambda_{\text{avg}} = 0.980$ and b) $\lambda_{\text{avg}} = 0.970$. The other oscillation parameters are the same for a) and b) with an amplitude of 0.025.	41

Figure 3:7 a) THC and b) CO concentrations during one oscillation with $\lambda = 0.970 \pm 0.025$ shown in Figure 3:6b.	41
Figure 3:8 THC concentration profiles at m.p.4 during oscillations at a) $\lambda = 0.990 \pm 0.025$ and b) $\lambda = 1.000 \pm 0.025$ with period lengths from 4 s to 14 s.	42
Figure 3:9 THC concentration profiles at m.p.4 during oscillations at $\lambda = 1.000 \pm 0.025$ with period lengths from 14 s to 40 s.	43
Figure 3:10 a) λ sensor signals and b-f) concentrations of various species at measurement points (m.p.1-4) during one oscillation with period length 40 s.	43
Figure 3:11 a) λ sensor signal at measurement points 1 and 4, b-d) concentrations of various species at measurement point 4 during lean/rich oscillations with period length 40 s.	44
Figure 3:12 Predicted and measured concentrations of various species at m.p.4 during steady state λ -sweep.	47
Figure 3:13 Predicted and measured concentrations of CO and THC during one oscillation at $\lambda = 0.990 \pm 0.025$, period = 14 s.	48
Figure 3:14 Reaction pathways of CH_4 via direct oxidation and SR during one oscillation at $\lambda = 0.990 \pm 0.025$, period = 14 s.	49
Figure 3:15 Model-predicted THC concentration profiles during oscillations with a period length from 4 s to 14 s ($\lambda = 0.990 \pm 0.025$).	49
Figure 3:16 Model-predicted surface coverage of different ceria species along the catalyst length with oscillations at $\lambda = 0.990 \pm 0.025$ and a period length of a) 4 s, b) 10 s and c) 14 s at four points in time each.	50
Figure 4:1 SEM image ($\times 30$) of the Pd/Rh catalyst.	53
Figure 4:2 CH_4 conversion of the a) Pd/Rh b) Pt/Rh catalyst during λ ramp-up (15 min) and ramp-down (15 min) at 520 °C (GHSV = 256000 h^{-1}).	54
Figure 4:3 Comparison of a) CO conversion b) NO_x conversion in the Pt/Rh and the Pd/Rh catalyst and c) H_2 concentration and d) NH_3 concentration downstream the catalysts during λ ramp-up at 520 °C.	55
Figure 4:4 CH_4 conversion during λ ramp-up and λ ramp-down in the Pd-only catalyst.	56
Figure 4:5 Comparison of NO_x conversion and NH_3 selectivity during λ ramp-up in the Pd-only and Pd/Rh catalyst.	56
Figure 4:6 CH_4 conversion during λ ramp-up and λ ramp-down in the Pd/Rh and Pt/Rh catalyst, at temperature a) 630 °C (GHSV = 546 000 h^{-1}), and b) 360 °C (GHSV = 83 000 h^{-1}).	57
Figure 4:7 CO concentration and CH_4 conversion during λ ramp-up and λ ramp-down in a) the Pd/Rh and b) the Pt/Rh catalyst at temperature 360 °C.	58
Figure 4:8 Comparison of temperature and concentration profiles upstream and downstream the Pd/Rh and Pt/Rh catalysts during cold start experiment.	59
Figure 4:9 Temperature and concentration profiles during temperature programmed reaction in model gas reactor.	60
Figure 4:10 THC, O_2 and NH_3 concentration profiles during slow λ oscillations at a) 360 °C, b) 520 °C, and c) 630 °C in Pt/Rh and Pd/Rh catalyst.	61
Figure 4:11 CH_4 conversion of the Pt/Pd/Rh catalyst during λ ramp-up and ramp-down at 520 °C.	62
Figure 4:12 THC, NO_x and NH_3 concentration profiles during oscillations with period length of 8 s, 20 s and 26 s.	63
Figure 4:13 THC, NH_3 , NO_x and O_2 concentration profiles for Pt/Pd/Rh catalyst during oscillations with $\lambda_c = 0.990, 0.995$ and 0.998 (corrected λ).	64

Figure 4:14 THC and NH ₃ emission under steady and oscillations in WHSC operating points for a) and c) Pt/Pd/Rh catalyst; b) and d) Pd/Rh catalyst.....	65
Figure 5:1 Simplified schemes of a) pressure-wave charger setup with one THC and one OC and b) turbocharger setup with two TWC stages. Measurement points (m.p.1-m.p.4) are also included in the schemes.	67
Figure 5:2 a) Temperature of m.p.1 for the conventional turbocharger (brackets) and the pressure-wave charger setup (without brackets), b) Temperature (top) and CO conversion rate (bottom) evolution during cold start for the pressure-wave charger setup (black) and turbocharger setup (grey).	68
Figure 5:3 a) Conversion rates of NO _x , CO, THC in the TWC, b) concentration of CO, THC, NO _x at m.p.1, c) concentration of CO, THC, NO _x at m.p.2 during steady and oscillating operation.	69
Figure 5:4 a) Conversion rates of H ₂ , CO, NH ₃ in oxidation catalyst, b) concentration of N ₂ O downstream of TWC during steady and dithering operations.	70
Figure 5:5 a) Conversion rates of NO _x , CO and THC in the first stage TWC under oscillating conditions, b) concentration of H ₂ , NH ₃ and CO at m.p.3 and m.p.4 in the turbocharger setup.....	70

List of Tables

Table 2:1 Feed composition of the different step experiments in the model gas reactor. The composition of the exhaust gas was switched from lean to rich with the compositions R1 to R5, followed again by the lean exhaust gas composition.	23
Table 3:1 List of reactions and reaction rate functions.....	46
Table 3:2 List of inhibition factor functions	47
Table 3:3 Concentrations and temperatures used as model input to simulate the lean and rich section of oscillations at $\lambda = 0.990 \pm 0.025$	48
Table 5:1 Engine operating points with corresponding temperature at inlet of TWC and OC.....	69

Chapter 1 Introduction

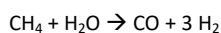
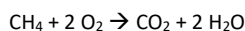
Diesel internal combustion engines dominate the heavy-duty transport sector today. To reach the goal of 55% CO₂ reduction by 2030, and net-zero CO₂ emission by 2050, a transition to alternative fuels and powertrains is urgently needed. Unlike light-duty vehicles, whose decarbonization path is clearly electrification, the road map for the heavy-duty sector is still vague. Competing technologies include fuel-cell vehicles, battery electric vehicles, natural gas internal combustion (ICE) vehicles, and ICE vehicles powered by bio-fuel/synthetic fuel. Several studies have predicted that natural gas engines (either compressed natural gas (CNG) or liquidified natural gas (LNG)) will remain the most competitive technology [1,2]. Natural gas has the potential of lowering well-to-wheel CO₂ emissions, in respect to diesel ICE vehicles [3]. The natural gas fueled vehicles can be further decarbonized by using renewable methane fuels (bio-methane/synthetic methane). The synthetic methane derived from power-to-methane pathways can help to solve the problem of seasonal variations in electricity production due to large-scale implementation of renewable energies. Synthetic methane is an ideal chemical energy carrier for seasonal storage, as it has the advantage of high storage density and low storage losses [4].

Despite its CO₂ advantage, methane itself is a strong green house gas. The complete conversion of methane (CH₄) remains a major concern, because the activation of symmetric tetrahedral CH₄ molecules are more difficult than other hydrocarbons [5]. A successful aftertreatment system for natural gas/CH₄ applications should be able to activate CH₄ conversion and balance emissions of other gaseous and particulate exhaust emissions.

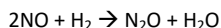
1.1 Engine emissions

1.1.1 Regulated and unregulated exhaust emissions

The harmful contents of an engine exhaust consist of mainly 3 groups: green house gases (CO₂, N₂O, CH₄), ozone hazard gases (NO_x, non-methane hydrocarbons (NMHC)) and health hazard gases (e.g. NH₃, CO, particulates, NO₂). The aftertreatment system has limited influences on CO₂ emission, which is mostly determined by the processes of in-cylinder combustion. CH₄ is the main component of natural gas. Unsurprisingly, unburnt CH₄ is the main hydrocarbon species in the natural gas engine exhaust. It has a global warming potential of 27 to 28 based on a 100-year period [6]. Ideally, CH₄ should be oxidized to CO₂ in the aftertreatment system, which is overall less harmful for the environment. CH₄ can be converted in the catalyst via two reaction pathways, direct oxidation by oxygen and methane steam reforming (SR):



N₂O is an extremely strong greenhouse gas and has a 100-year global warming potential of around 290 [7]. N₂O is formed in the exhaust aftertreatment system, via the following reactions:



Luckily studies have shown that N₂O emission occur almost strictly at low temperatures (below 350°C) [8,9], particularly during cold starts. As heavy-duty vehicles typically operate long distances and times during the day, cold start accounts for only a small fraction of the total emission. N₂O emission is until now not regulated in the EURO VI emission standard [10]. NO_x is one of the major and most frequently discussed pollutants in the engine exhaust. NO_x is formed at high temperatures during the combustion process [11], regardless of the fuel type (diesel, gasoline, natural gas, etc.). NO_x is a precursor for O₃ formation [12]. Apart from elevating O₃ concentrations, NO_x also causes other environmental concerns, including formation of acid rain and PM 2.5. The engine out NO_x emission can be lowered by various techniques that can reduce the combustion temperature, including EGR [13], in-cylinder water injection [14], and late intake valve closing [15]. Lean combustion (e.g. diesel) also leads to lower NO_x production due to lower combustion temperatures. With stringent emission regulations, almost all heavy-duty vehicles are equipped with NO_x abatement aftertreatment catalysts. NMHC is another precursor of O₃ from engine exhaust [16]. Literatures have reported that NMHC in the natural gas exhaust mainly consists of light NMHC in the range of C₂ – C₄ [17]. Another important pollutant is NH₃, which is rather formed in the catalysts and is particularly a problem for natural gas fueled stoichiometric engines [18]. NH₃ contributes significantly to the

formation of health hazardous PM_{2.5} [19] and is regulated under EURO VI emission standard [10]. The relevant reaction pathways are also an item of the present study and are discussed in later sections.

CO is a by-product caused by partial combustion of fuels. Being exposed to CO containing exhaust gases can result into high blood levels of CO, which can be even lethal and disrupt critical processes of brain development in children [20]. CO can be easily oxidized into CO₂ by oxygen. When oxygen is not available, CO goes through water gas shift. Particulate matters are associated with a series of cardiovascular and respiratory diseases. Until now, particles up to 23 nm size are regulated. Due to the smaller molecule size of CH₄, less particulate matters larger than 23 nm are formed during combustion in natural gas engine, in comparison to diesel [21]. Typically, no particulate filter is needed in natural gas engines. However, many studies have already investigated sub-23 nm particles. It is concluded that the particle size distribution peak for natural gas engines is below 5 nm [22].

1.1.2 Current Emission standards (Europe, US and China) for heavy duty on-road vehicles

Europe, US and China are the three largest road transport regions [23], each having their own emission regulations. The current European heavy-duty emission standard is commonly referred as EURO VI [10], which is adopted for motor vehicles with maximum weight exceeding 3500 kg. The EURO VI was implemented in heavy-duty type approvals starting from 2013, comprising emission limits for CO, NO_x, HC, NH₃, and particulate matter under specified testing procedures. Two sets of testing procedures are used for engine type approvals (engine dynamometers): world harmonized steady cycle (WHSC) and world harmonized transient cycle (WHTC). The emission standard is applicable for different engine types (including compression ignition and spark ignition types), but with slightly different emission limits. Compared to the previous EURO V, EURO VI reduces the NO_x emission limit more than 4 times. CO and HC emission limits are also significantly lower than the previous EURO V. EURO VI also introduces requirements of off-cycle emissions (OCE) testings, including laboratory tests following the not-to-exceed (NTE) limit approach and in-use portable emissions measurement systems (PEMS) testing.

China has fully adopted the emission standard China VI-a in 2021 [24], which is largely equivalent to EURO VI. However, a new emission standard China VI-b [24] is gradually phasing-in starting from 2021 and will be applied to all heavy duty vehicles from 2023. The China VI-b emission standard also includes on-road PEMS testing requirements.

The US adopts its own sets of regulations: federal emission standards (by US Environmental Protection Agency) and California standards (by California Air Resources Board (CARB)). The emission limits are based on chassis dynamometer testing: heavy-duty federal test procedure (FTP) transient cycle. Unlike EURO VI, the US emission standards are fuel-neutral, without distinguishing compression ignition and spark ignition engines. The current emission standard was phased-in starting from 2007 and fully adopted in 2010. Compared to EURO VI emission standard, the current US standard has already stricter NO_x limit (US: 0.268 g/kWh; EU: 0.4 g/kWh) [25]. However in 2020, the 'Heavy-Duty Low NO_x Omnibus Regulation' was approved by CARB, which stipulates that the NO_x limit will be further reduced to 0.0268 g/kWh (90% reduction) by 2027 [26]. Apart from NO_x, the US standards regulate CO, hydrocarbons (HC) and particulate mass (PM). NH₃ is not regulated in US standards.

1.2 Catalytic emission abatement

1.2.1 Layouts of aftertreatment system

Depending on the fuel type, the in-cylinder combustion processes are either performed under stoichiometric conditions or lean conditions. The combustion type of the engine determines the general layout of the aftertreatment systems. Lean combustion (diesel, lean combustion natural gas, dual fuel, and DME engines) results in excess oxygen in the aftertreatment system. The excess oxygen helps in oxidizing CO and HC in the oxidation catalyst (OC), but competes with NO_x for reduction agents. The reduction of NO_x is performed either in lean NO_x traps (LNT) or in selective catalytic reactor (SCR) systems. For SCR system, a dosing system of urea water solution is needed, which releases NH₃ as the reducing agent for NO_x. Due to the tendency of particulate matter formation in inhomogeneous combustion, a particulate filter (PF) is possibly needed for complying with particulate emission standards. The aftertreatment systems for lean burn engines are significantly more complex than the stoichiometric counterparts (discussed below). Not only a combination of different abatement technologies (PF, LNT, SCR, OC) has to be arranged, but also compatible urea dosing systems (for SCR) and/or engine transient control strategies (for LNT) are required.

During stoichiometric combustion, the amount of air exactly matches the fuel amount, resulting in very low oxygen levels in the exhaust. Typical fuels for stoichiometric combustion are gasoline and natural gas. For stoichiometric gasoline exhaust, three-way catalyst (TWC) can efficiently remove CO, NO_x and HC simultaneously. In case of gasoline direct injection (GDI), an additional gasoline particulate filter (GPF) might be needed. For natural gas applications, due to the high activation energy of CH₄, which is the main HC

in the exhaust, CH₄ conversion stays low. The goal of this study is to promote CH₄ abatement in stoichiometric natural gas fueled engines, without compromising the emissions of other species.

1.2.2 CH₄ oxidation under lean conditions

Under oxygen rich conditions, CH₄ is only oxidized by O₂ to CO₂ (complete oxidation) [27]. A lean activity ranking of Pd > Rh > Pt > Ru was identified in [28]. Rh was found to have advantages in CO oxidation and has high tolerances for SO₂ and H₂O poisoning [29]. The main drawback of Rh is its significantly higher price compared to Pt and Pd. Therefore, Rh is only added in small amounts in TWCs to promote the N₂ selectivity in NO_x reduction. In oxidation catalysts, no Rh is used. Most lean CH₄ oxidation catalysts are either single metal catalysts (Pd or Pt) or bimetallic Pt/Pd catalysts. Pt catalysts sinter relatively fast under oxidation environments due to volatile PtO₂ [30], which can lead to very large Pt particles [31]. PtO₂ is thermally unstable and starts to dissociate to metallic Pt at temperatures higher than 250°C [32]. As typical exhaust temperatures are well above 250°C, the majority of Pt exists in metallic form, which is the active form for CH₄ oxidation [33]. Alloying Pd and Pt can significantly inhibit sintering of Pt, by trapping the volatile PtO₂ [34]. As the thermal stability of Pd catalysts is less a concern than of Pt catalysts, more studies focus on Pd as catalysts for CH₄ oxidation.

PdO, compared to PtO₂, is more stable. Depending on the support, literatures have reported that the PdO dissociation temperature varies from 750°C to 850°C [35,36]. A temperature hysteresis of PdO dissociation and Pd reoxidation has been reported in many previous studies [37–40]. When slowly cooling down from high temperatures (Pd in metallic form), the metallic Pd does not start to be reoxidized in oxidation environment until 100–200 °C lower than the dissociation temperature. Through analyzing the CH₄ conversion during temperature ramp-up and down, the activity of Pd and PdO can be compared. Studies have concluded that metallic Pd has lower activity toward CH₄ oxidation compared to PdO at low to mid temperatures [38,40]. At high temperatures, when PdO is unstable, metallic Pd is able to efficiently convert CH₄. Several studies hold the opinion that a mixture of Pd/PdO results in the highest activity of CH₄ [41,42]. The argument was supported by experiments adding rich pulses to steady lean feed [43]. The idea is that PdO is quickly reduced during the rich pulse and therefore leads to a transient state Pd/PdO mixture after falling back to the lean feed. In some other works, the increase of conversion after the transition of metallic Pd to PdO is explained by the high activity of freshly formed PdO, compared to bulk PdO. It is explained that the higher activity comes from surface roughening [44,45].

Several works have engaged in studying changes of CH₄ oxidation reaction rates in relation to gas species in the feed. With excess oxygen, the CH₄ oxidation reaction is zero-order toward oxygen concentration and first order toward CH₄ concentration [46–48]. When injecting CO in the exhaust of a lean natural gas engine, oxidation of CO increases the local temperature in the catalyst and promotes CH₄ conversion [49]. NO_x was found to have an inhibition effect, which was attributed to the formation of nitrates on the surface [50]. In engine applications, water vapor in the exhaust is impossible to avoid. Water is known to deactivate Pd catalysts under lean conditions due to the formation of less active Pd(OH)_x [51]. The water inhibition effect occurs only at low temperature and is negligible at temperatures higher than 550°C [52].

1.2.3 CH₄ direct oxidation and steam reforming at near stoichiometric conditions

The air-to-fuel (AFR) equivalence ratio, lambda (λ), is commonly used to assess the oxidizability/reducibility of the exhaust mixtures. λ is defined as the ratio of actual AFR to stoichiometry AFR: $\lambda = \text{AFR}/\text{AFR}_{\text{stoich}}$. At $\lambda > 1.0$, the mixture is in oxygen-rich condition (lean); at $\lambda < 1.0$, the mixture is in oxygen-poor conditions (rich). At near stoichiometric conditions, a slight change in the feed compositions can lead to transitions from lean to rich conditions (or vice versa). These transitions quickly change the distribution of catalyst surface species, and further influence reaction rates and even conversion pathways. Two reactions are relevant for CH₄ abatement in natural gas exhaust at near stoichiometric conditions: CH₄ complete oxidation (by oxygen) and CH₄ steam reforming (SR). Despite CH₄ reaction with oxygen is mostly in focus for exhaust applications, the importance of SR has been noted by [50,53], especially after O₂ has been completely consumed by other reducing agents. In principle, CH₄ can also react with NO. The reaction between CH₄ and NO is strongly inhibited by both O₂ and CO [54]. In the exhaust environment, either O₂ is in excess (lean exhaust) or CO is in excess (rich exhaust). The reaction between CH₄ and NO is therefore unlikely to occur and is excluded in this investigation.

Oxygen presence influences CH₄ direct oxidation in various modes. On one hand, chemisorbed O₂ hinders the activation of CH₄ on active sites which consist mainly of metallic Pd [55]. A particularly high CH₄ oxidation rate was observed at only slightly rich conditions, where the metallic Pd surface was not fully covered by chemisorbed O₂. On the other hand, with increasing O₂ partial pressure, oxidation from Pd to PdO is observed. Crystallized PdO surfaces result in higher CH₄ oxidation rate than fully covered (by chemisorbed O₂) metallic Pd surfaces [55]. Besides O₂, adsorbed CO [56,57] also inhibits CH₄ activation on catalysts surfaces. This mainly affects SR under rich conditions. Under lean conditions, CO is quickly consumed with adsorbed O₂ and does not affect CH₄ activation.

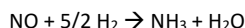
Methane SR is an important process for production of syngas and hydrogen, which are important feedstocks for many industrial chemical processes. SR in the exhaust gas is rarely discussed, because natural gas-powered vehicles remain until now a niche market. The mostly discussed methane SR catalysts are either Ni catalysts or Platinum-group catalysts. Ni SR catalysts have the problem of easy coke formation and low stability [58]. Under fuel rich conditions, the reported activity of Platinum-group metals towards SR are ranked as follow: Rh>Ru>Pd>Pt [59]. All TWCs nowadays contain either one, or a combination of Pd, Pt and Rh. In addition, ceria sites on the catalyst surface, mainly used for oxygen storage purposes, can promote methane SR [60]. In order for SR reaction to occur, two sub-processes have to take place: the activation of methane and the adsorption of H₂O. The activation of CH₄ occurs on the noble metal sites, forming CH_x fragments [56,61]. The adsorption of water occurs on the ceria compounds [62,63]. This reaction mechanism is very similar to the proposed water gas shift mechanism, where CO is adsorbed in the Platinum-group metal sites, and H₂O on the ceria sites [64,65]. Various studies have suggested that water gas shift catalysts can be deactivated by the formation of carbonaceous species on the ceria compounds [66–68].

Sulfur poisoning is a widely discussed topic during CH₄ steam reforming [69–71]. The noble metal catalysts are very sensitive to sulfur poisoning. Even a SO₂ concentration of 0.3 ppm can lead to sulfur accumulation and therefore lower reaction rates [70]. Sulfur poisoning takes place by blocking noble metal sites via formation of either sulfide or sulfate [71,72]. The sulfur compounds tend to spill-over to the support materials. Therefore, complete regeneration of sulfur poisoned catalysts is extremely difficult [72].

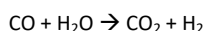
1.2.4 N₂O and Ammonia formation

Apart from methane abatement, the reduction of NO_x is another important process in TWCs. The reduction of NO_x can only occur at stoichiometric to rich conditions, because NO_x adsorption takes place only on 'clean surface' free of adsorbed oxygen [73]. Although the hope is that all NO can be selectively reduced to N₂, unwanted side products, e.g. NH₃ and N₂O are inevitably produced. N₂O emission is mainly reported during cold starts [8,9]. N₂O formation is an elementary step in the process of NO reduction to N₂ [74]. Part of the N₂O are desorbed into the gas phase, but can later undergo readsorption and further reduction.

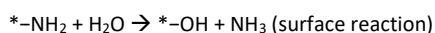
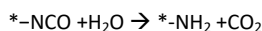
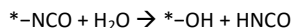
In contrary to N₂O, NH₃ formation occurs at higher temperatures [9,75,76]. The formation of NH₃ can follow different reaction pathways, depending on the feed components. The most straightforward formation pathway is NO_x reduction by H₂, when H₂/NO ≥ 2.5 [77]:



When H₂/NO < 2.5, the deficiency of H₂ can be relieved with the aid of water gas shift, which produces H₂, and assists NH₃ formation.



Several studies have referred to this reaction pathway as water gas shift assisted NH₃ formation [78,79]. Another proposed pathway involving CO and H₂O is hydrolysis of isocyanate groups at low temperatures [73] (via surface reactions):



Catalyst compositions can influence the selectivity toward NH₃ and N₂O. Rh has the highest selectivity toward N₂ during NO_x reduction [80,81], but has to be introduced segregated from Pd for obtaining a cooperative effect [80]. However, the high price of Rh suggest that this is a costly solution.

1.3 Modeling of catalytic processes

To model the catalyst behavior, many physical and chemical processes have to be taken into account, including mass transfer (both gas phase and gas to surface as well as in micropores), heat transfer, adsorption, chemical reactions and desorption. The importance of different mass transfer limitations has been stressed in many of the works [27,82,83]. In general, diffusion increases with increasing temperature. Different modeling approaches are characterized by varying detail levels of channel representations (1d to 3d) and diffusion models (no diffusion, 0d diffusion with effective diffusion coefficient and 1d diffusion). An analytic benchmark comparison of the existing approaches is delivered in [84]. It is concluded that 1d model with 1d diffusion is accurate enough for the prediction of the concentrations along the catalyst.

There are two ways to model a system of catalytic reactions. The first way is to describe the chemical reactions by elementary steps, including adsorption, dissociation, reactions between surface species and desorption. With this method, a clear picture of competition for active sites, surface coverages, and interaction of surface species can be derived. Many studies have successfully deployed this method in simulating catalytic behavior under feed of simple compositions [39,53,85,86]. The downside of such detailed description of surface reactions is that many reaction coefficients of elementary reactions are unknown. In addition, it is difficult if not impossible to determine these, given that some of the elementary processes cannot be isolated. A more general way of modeling reaction systems is to use global reactions. For these reactions a Langmuir-Hinshelwood scheme is used. In order to model the competition for active sites, inhibition factors are introduced in the reaction rate equations. Pioneering works have focused on configuring inhibition factors via experimental data [87,88]. The previously discussed competition between NO_x and O_2 for active sites is modeled with a 0.7 order inhibition factor [88]. The CO self-inhibition effect is covered by a second order inhibition factor [88]. Global reaction models have been successfully implemented in predictions of catalyst behaviors in gasoline [89] and natural gas exhausts [90].

1.4 Aim and scope of the thesis

The aim of this doctoral thesis is to advance knowledge in catalytic emission abatement and to reduce overall hazardous pollutant emission in natural gas exhausts. The research focuses on several different aspects: analyzing and understanding the CH_4 conversion pathways; designing operation strategies to maximize the activity of the catalysts; studying the formation and abatement of ammonia; investigating the metal-specific characteristics to guide improvements in catalyst formulation. To achieve these goals, the research goes through four progressive parts:

1. In the first part (Chapter 2), CH_4 oxidation reaction pathways in the Pd/Rh catalysts were studied under steady state and step transitions (from oxygen-excess to oxygen-poor and vice versa) on the engine test bench. In this way, the transition between two major methane conversion pathways (steam reforming and complete oxidation by oxygen) was investigated. Supplementary model gas reactor measurements and operando DRIFTS measurements were performed to study the influence of concentration changes and surface species coverages on CH_4 conversion. This chapter is based on the published results in the 'Chemical Engineering Journal'.
2. In the second part (Chapter 3), based on the results of Chapter 2, CH_4 conversion in the Pd/Rh catalysts during fast transitions between oxygen-excess and oxygen-poor conditions were investigated on the engine test bench. The fast oscillations resulted in alternating surface coverages, state of oxygen storage compounds (OSC), reaction rates and reaction pathways. These transitions were analyzed further with a global reaction model, embodying the proposed reaction mechanisms. The simulation model enabled spatial analysis of surface coverages along the catalyst axis. This chapter is based on the published results in a second article in the 'Chemical Engineering Journal'.
3. In the third part (Chapter 4), the characteristics of different Platinum-group metals in emission abatement were studied. Several commercial catalysts of different Platinum-group metal compositions were tested and compared under quasi-steady state and oscillating conditions. The formation and abatement of NH_3 is analyzed alongside CH_4 abatement. Based on the derived characteristics, a catalyst with improved composition is evaluated under regulated driving cycles. This chapter is based on the published article in the journal 'Catalysts'.
4. In the fourth part (Chapter 5), a particular aftertreatment system was investigated under a pressure-wave charger setup. The particular system had the significance of combining the advantage of a TWC operating near stoichiometry and an OC operating under lean conditions. Emissions were studied under cold start and various oscillating conditions. These attempts provide additional insights in balancing the emission of CH_4 with other hazardous species. This chapter is based on the results published in 'Energies'.

The last chapter (Chapter 5) presents an overview of important findings and suggests directions of future researches.

Chapter 2 Reaction pathways of methane abatement under steady and λ -step conditions

Parts of this chapter are published in: M. Wang, P. Dimopoulos Eggenschwiler, T. Franken, D. Ferri, O. Kröcher, Reaction pathways of methane abatement in Pd-Rh three-way catalyst in heavy duty applications: A combined approach based on exhaust analysis, model gas reactor and DRIFTS measurements, Chem. Eng. J. 422 (2021) 129932. <https://doi.org/10.1016/j.cej.2021.129932>.

In this chapter, we provide a comprehensive analysis of the conversion pathways of methane abatement. As discussed in the introduction chapter, two reactions dominate CH_4 conversion in exhaust environments – methane direct oxidation by oxygen and methane steam reforming. The reaction rates are strongly influenced by the catalyst states, e.g. oxidation state of active materials and surface coverages. Here, the catalytic performances were investigated in steady and transient operation conditions over a range of different temperatures, leading to insights on reaction pathways. Important findings from the engine experiments were further investigated in a model gas reactor with simulated exhaust gas for the flexibility of changing concentration of individual gas compositions. The surface species evolution of the catalyst was studied with infrared spectroscopy. The combination of industrial-size test bench experiments with spatially resolved gas phase analysis and model gas studies in the lab with surface spectroscopy provided clear evidences for the chemical reaction pathways of methane abatement over Pd-based oxidation catalysts in natural gas vehicles.

2.1 Experimentals

2.1.1 Engine test bench setup

The catalysts studied in this work were mounted in the exhaust line of an original equipment manufacturer (OEM) heavy-duty 4-cylinder natural gas engine operated under stoichiometric conditions. The engine had a bore diameter of 95.8 mm and a stroke of 104 mm. Engine torque was regulated by a Horiba DYNAS asynchronous electric machine. Natural gas from grid was used as the fuel and components were regularly controlled by gas chromatography. Natural gas was injected at each cylinder port. After in-cylinder combustion, exhaust gas passed the turbine of the turbocharger before reaching the aftertreatment system.

Two stages of aftertreatment catalysts were mounted downstream of the turbocharger, both commercial Pd/Rh three-way catalysts. The two-stage setup and catalysts were inherited from the serial production engine model. In both stages, the catalysts were cylindrical in shape and had a cell density of 400 cpsi. The first stage catalyst (diameter 105 mm; total volume 0.65 L) was based on a metallic substrate coated with Pd/Rh supported on alumina ceria-zirconia (250 g/ft³; Pd/Rh ratio = 24:1). The second stage catalyst (diameter 172 mm; total volume 2.3 L) consisted of a ceramic substrate with Pd/Rh supported on alumina ceria-zirconia (70 g/ft³; Pd/Rh ratio = 14:1). In commercial applications, these catalysts are mounted as whole pieces for each stage. On our engine test bench, the catalysts were cut in three slices of equal volume in each stage, in order to follow the concentration evolution along the catalyst axis at discrete locations. This is similar to the SpaciMS method in model gas reactors [51,91], which is used to measure spatial concentration profiles. The total catalyst volume of each stage is identical to the serial production catalyst of that stage. The distances between each slice are minimized in order to neglect heat losses caused by the new assembly. Sampling points and thermocouples have been mounted between each slice as well as upstream and downstream the entire catalyst system (in total eight measurement positions as indicated by numbers 1 to 8 in Figure 2:1).

At each measurement point, the temperature was measured with a K-type thermocouple. A Horiba MEXA-7400 two-line exhaust gas measurement system (combined system of nondispersive infrared sensor, chemiluminescence detector, paramagnetic oxygen analyzer and flame ionization detector) was attached to all measurement points. In addition, all measurement points were connected to an AVL infrared spectrometer (FTIR) and an H-Sense mass spectrometer (MS), which measures H_2 concentration. The MEXA measurement system provided fast response for a limited number of species (10 Hz), while the FTIR spectrometer delivered information

on more species but at slower response time (around 1 Hz). Each instrument measured only one sample point at a time, but simultaneous measurements with several instruments at each sample point is possible. The switch between measurement points is controlled electronically by hydraulic valves.

Two Bosch LSU4.9 lambda sensors were mounted before the first stage catalyst slices and downstream of the second stage catalyst slices. The exact λ estimation is fundamental for this investigation. Though used by the engine system control, the λ sensor signal shows non negligible dependencies on the mounting location and fuel type [92,93]. A wide range of investigations agree that the most exact λ definition is based on the equation proposed by Brettschneider et al. [94], which contains an empirical term for the estimation of water in the exhaust gas. In this study, this equation was modified as follows, as water concentration was obtained by FTIR and MS data (the last term of the denominator):

$$\lambda = \frac{[CO_2] + \left[\frac{CO}{2}\right] + [O_2] + \left[\frac{NO}{2}\right] + (H_{cv} \times ([CO_2] + [CO] + (n \times [HC]))) - 3 \times [NH_3] - 2 \times [H_2])/4}{\left(1 + \frac{H_{cv}}{4} - \frac{O_{cv}}{2}\right) \times ([CO_2] + [CO] + (n \times [HC]))}$$

H_{cv} , O_{cv} and n is the number of H, O and C atoms in the fuel. In this equation, the numerator is representing the number of O atoms, while the denominator C atoms.

The pre-measurement assessment showed that the temperature immediately upstream of the first stage catalyst was between 340°C and 725°C throughout the entire engine map. Four operating points were selected for the detailed measurements with inlet temperatures of approximately 430°C (engine speed: 1600 rpm, torque: 70 Nm), 520°C (600 rpm, 150 Nm), 590°C (2200 rpm, 150 Nm), and 660°C (2800 rpm, 220 Nm) respectively. These operating points will be later referred to only by their inlet temperature.

The compositions of THC in the exhaust was analyzed by FTIR spectroscopy. Approximately 90% of the THC in the exhaust were CH₄ (this was almost invariant at small λ variations). The next abundant hydrocarbons (HC) were C₂H₆, and C₂H₄. To better match transient results, THC concentrations measured with MEXA-7400 were used to assess the hydrocarbon conversions unless otherwise specified.

2.1.2 SEM/EDX catalyst characterization

SEM/EDX analysis was performed on the second stage ceramic catalyst with a Hitachi TM3030Plus to characterize the catalyst surface and show the ceria/zirconia OSC in the support.

2.1.3 Steady state λ -sweep measurements

The engine was first stabilized at $\lambda = 0.9$ at the designated engine speed and torque. After stabilization, sequential measurements at each available measurement point were performed. The target λ value was then increased to 0.95. Thereafter the target λ was increased by increments of 0.01 until $\lambda = 1.05$ is reached. At around $\lambda = 1$, the step resolution is further refined to 0.001 to capture more details near stoichiometry. The species concentrations were averaged over 1 min at each position. Engine speed and torque were kept constant throughout each λ -sweep.

2.1.4 Transient λ -step measurements

To obtain a defined initial state of oxygen storage, the ceria was either completely reduced and/or oxidized before each transient measurement. The engine operation procedure was defined as follows: the engine first run under rich conditions at $\lambda = 0.9$ for 2 min. This procedure ensured defined conditions of the ceria storage at the start of each transient. Then a transient λ -step measurement from fuel rich ($\lambda = 0.98$) to fuel lean ($\lambda = 1.03$) was recorded. After operating at $\lambda = 1.03$ for 120 s, the next λ -step measurement from lean to rich was prepared by running the engine at $\lambda = 1.1$ for 2 min. A lean ($\lambda = 1.03$) to rich ($\lambda = 0.98$) transient step was then recorded. As only one sampling line could be measured at one time, this procedure was repeated several times while sampling at a different measurement point. A scheme of the transient λ -step measurement procedure is presented in Figure 2:1.

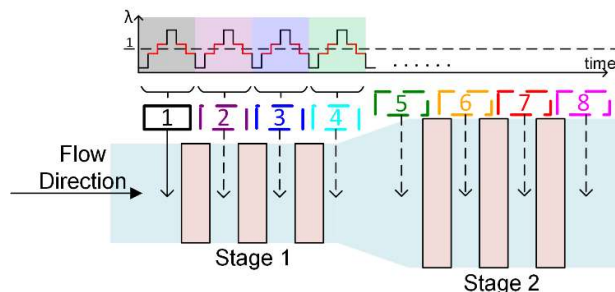


Figure 2:1 Scheme of transient λ -step measurements. Top: engine operation λ targets over time. Bottom: scheme of sliced catalyst system and measurement points 1 to 8.

2.1.5 Model gas reactor λ -step measurements

For the model gas reactor, cylindrical pieces (1.39 cm² entrance area, 4.83 cm length; 86 closed cells) of the second stage catalyst were cut from an identical ceramic monolith. The model gas reactor was equipped with a gas mixing unit, which allows separate control of the concentration of H₂ (diluted in N₂), CO, NO, O₂, CH₄ and N₂ in the model gas flow stream. A water evaporator was used, which can generate a maximum of 5 vol% water vapor in the gas feed. The difference in water content is compensated with N₂. The outlet of the reactor was analyzed using a FTIR spectrometer (iS50, Thermo) using a 2-m cell heated to 180 °C and a mass spectrometer (Pfeiffer, Omnistar). A series of λ -steps from lean to rich were performed. The feed gas compositions initially resembled the composition of the engine exhaust gas with elevated oxygen levels (similar to the exhaust gas from slightly lean combustion) and are listed in Table 1 (lean). The feed gas was kept for 10 min in order to condition the catalyst before performing the step change in λ value to a gas composition resembling the exhaust gas from a rich combustion mixture. The rich phase was maintained for 10 min before the feed gas was shifted again to lean exhaust mixture and continued with the next λ -step change. The corresponding gas compositions were derived from engine exhaust concentration profiles at $\lambda = 1.03$ and $\lambda = 0.98$ and an inlet temperature of 520°C. The water vapor concentration was kept at 5 vol% throughout all experiments due to technical limitations imposed by the model gas setup. In the λ -steps examined with the model gas reactor, the CO and H₂ concentrations in the feed gas were varied as follows: In the first rich stage (R1), the feed gas borne the same CO concentration as derived from the engine measurements at $\lambda = 0.98$. In the second rich stage (R2), the CO concentration was reduced by 50%; in the third rich stage (R3), CO was not present in the feed gas and H₂ was dosed at the same concentration throughout the steps R1-R3. In the fourth rich stage (R4), no CO was introduced in the feed and H₂ was added to the same concentration of CO in R1 in order to keep the same amount of reducing agent, thus the same λ . A fifth step (R5) served as repetition of R1. All experiments were performed at a volumetric gas hourly space velocity (GHSV) of 75,000 h⁻¹ and at an inlet temperature of 520 °C.

[ppm]	CH ₄	O ₂	CO	NO	H ₂
Lean	1144	6613	2342	2882	1414
R1	1376	3453	8654	1842	6062
R2	1376	3453	4327	1842	6062
R3	1376	3453	0	1842	6062
R4	1376	3453	0	1842	14716
R5	1376	3453	8654	1842	6062

Table 2:1 Feed composition of the different step experiments in the model gas reactor. The composition of the exhaust gas was switched from lean to rich with the compositions R1 to R5, followed again by the lean exhaust gas composition.

Diffuse reflectance infrared Fourier transform (DRIFT) spectra of the second stage catalyst were obtained using a Vertex 70 spectrometer (Bruker) equipped with a diffuse reflectance mirror unit (Praying Mantis, Harrick) and a MCT detector. The catalyst was crushed to obtain a powder and was filled in the sample cup of the commercial DRIFT cell (Harrick). The cell was closed with a flat

CaF₂ windows (2.5 cm) sealed by graphite. The gas feed manifold used for the model reactor study was used to deliver gases to the cell, but the cell was inserted in a side line of the main line to the reactor so that only 100 mL/min of feed could be used while maintaining the same gas composition. Prior to the DRIFTS analysis, the fresh catalyst was conditioned at 420 °C under lean conditions for at least 2 h and purged with N₂. Spectra were acquired at 4 cm⁻¹ resolution and 10 kHz scanning rate by accumulating 20 scans resulting in a time resolution of 27 s. Background spectra were collected in N₂ at the reaction temperature of 420 °C. 5 vol% H₂O was added first followed by sequential addition of the different gases to produce the lean feed (1507 ppm CH₄, 7923 ppm O₂, 2144 ppm CO, 2441 ppm NO, 1227 ppm H₂). After signal stabilization (ca. 10 min), a step change to rich was made and the rich feed (1830 ppm CH₄, 4496 ppm O₂, 8365 ppm CO, 1690 ppm NO, 5944 ppm H₂) was maintained for 10 min. The gas compositions were derived from engine exhaust concentration profiles at inlet temperature 430 °C.

2.2 Results and Discussion

2.2.1 SEM/EDX characterization

Figure 2:2a shows the SEM image of the second stage ceramic substrate catalyst. The EDX mapping of the marked red zone in Figure 2:2a is demonstrated in Figure 2:2b-d. The white feature in the size of 1-10 μ m (Figure 2:2a) is recognized as ceria/zirconia supported on alumina. Analysis by means of image processing technique has identified that ceria/zirconia agglomerates comprise around 14 area% of the catalyst surface.

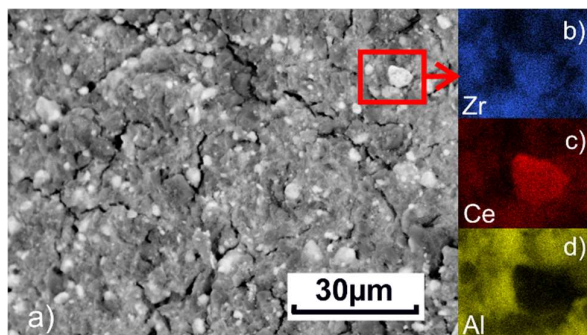


Figure 2:2 a) SEM image of stage 2 ceramic catalyst, b) EDX Zirconium mapping, c) cerium mapping, and d) aluminum mapping of the marked area in a).

2.2.2 Steady state λ -sweep

The concentration profiles of major species at different λ values (from rich stoichiometry $\lambda < 1$, to lean stoichiometry $\lambda > 1$) are plotted in Figure 2:3a-f. This experiment was conducted at a catalyst inlet temperature of 590 °C and at a GHSV of ca. 350,000 h⁻¹ for the first stage catalyst and ca. 99,000 h⁻¹ for the second stage catalyst. At such high GHSV, the conversion characteristics are heavily dominated by reaction rates and mass transfer limits than by thermal equilibrium. Therefore the following discussion focuses on the interpretations of reaction pathways and reaction rates. Figure 2:3a shows clearly that most of the oxygen was consumed in the first catalyst slice. The small amount of oxygen remaining for the downstream slices (particularly at $\lambda < 1$) was most likely due to mass transfer limitations in the first slice. At λ values below stoichiometry, CO was converted in every slice (Figure 2:3b) despite the negligible amount of oxygen remaining after the first slice. This indicates that CO conversion at $\lambda < 1$ was mainly due to the WGS reaction. The importance of WGS reaction was additionally evidenced by the increase of the hydrogen concentration at measurement point 2 and downstream (Figure 2:3c). As methane concentration stays constant from measurement point 1 to 8 at $\lambda < 0.975$ (Figure 2:3f), neither direct oxidation nor steam reforming of methane occurs. Hydrogen at $\lambda < 0.975$ could stem only from the WGS reaction. A high concentration of ammonia was formed at $\lambda < 0.99$ (Figure 2:3e). The exhaust gas contains high H₂O content (18 \pm 1 vol%), which varies with different λ values. Several ammonia reaction pathways could coexist with abundance of H₂ (Figure 2:3c), CO (Figure 2:3d) and H₂O in the exhaust gas mixture, including direct reaction between H₂ and NO [73], WGS assisted NH₃ formation [35] and hydrolysis of isocyanate [78,95]. The ammonia formation occurred predominantly in the first slice and its concentration increased only slightly in the following slices, because only low concentration of NO_x was detected in the downstream slices. The particular sensitivity of methane oxidation to λ deviations from stoichiometry ($\lambda = 1$) can be observed in Figure 2:3f. High THC conversion rate was limited to a very narrow region around stoichiometry and decreased in both the lean and rich regions. The loss of methane conversion at $\lambda > 1$ was generally attributed to the presence of chemisorbed oxygen on Pd that inhibited CH₄ activation [47,48,55].

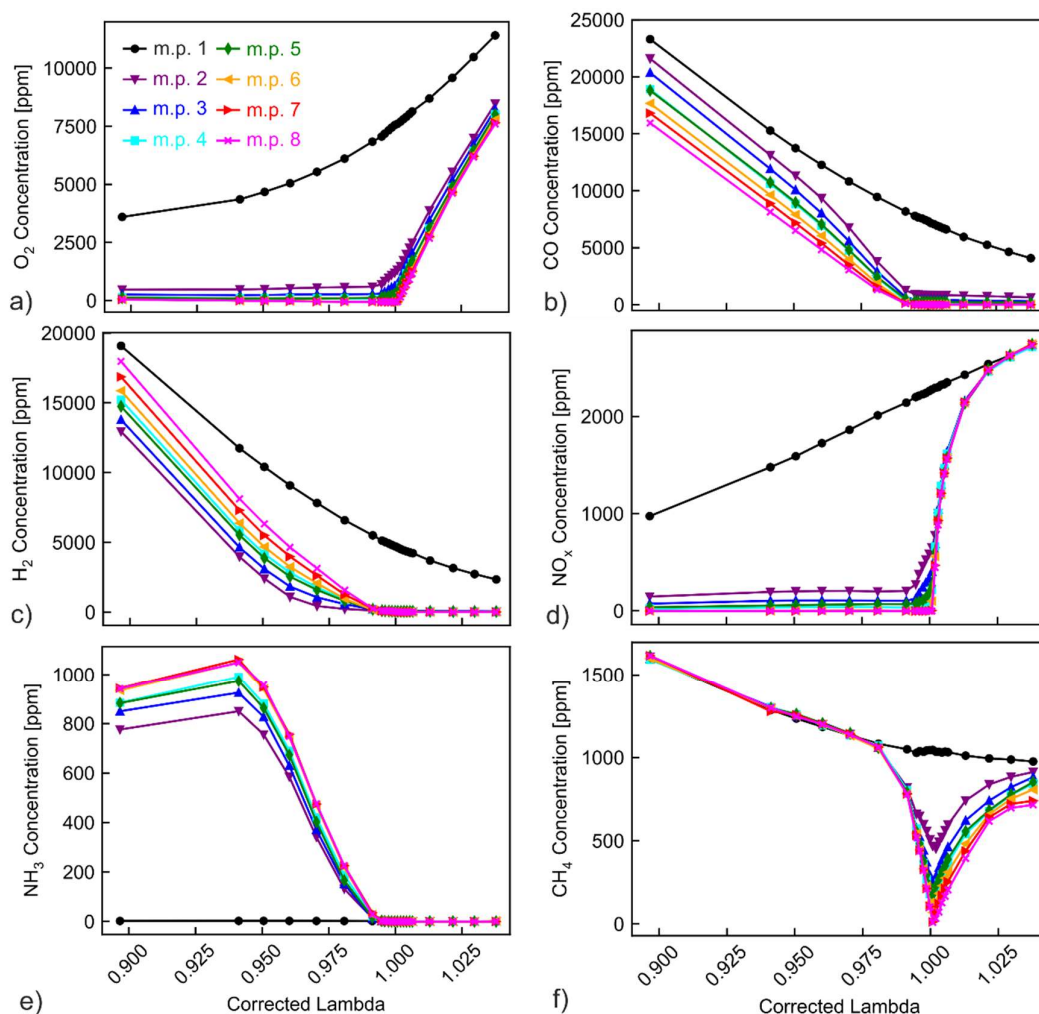


Figure 2:3 Concentration profiles of major species at different λ values recorded at measurement points numbered from 1 to 8 (Figure 2:1).

In order to investigate the conversion efficiency of each catalyst slice, the methane conversion rate of each slice was computed based on the methane concentration at the inlet and outlet of the slice. Methane conversion in the first slice (blue line in Figure 2:4a) started to be evident at $\lambda = 0.991$. At this λ value no methane conversion occurred in the second and in the third slice. At $\lambda = 0.995$, methane conversion increased in the first slice and some methane conversion was observed in the second slice, while no methane was converted in the third slice. The oxygen concentrations at the inlet of slice 2 and 3 are plotted together with the CH_4 conversion rates in Figure 2:4a. For better illustration of the increase of oxygen concentration at around $\lambda = 0.99$, the oxygen concentrations are shifted so that the concentrations at $\lambda = 0.973$ are aligned to zero. The methane conversion in slice 2 commenced exactly when excessive oxygen started to be available at the inlet of slice 2. Similarly, the methane conversion in slice 3 started only when excessive oxygen entered slice 3. This indicates that oxygen was necessary for methane conversion, which implies that methane was converted through direct oxidation with oxygen. In Figure 2:4b, the hydrogen concentrations are plotted together with methane conversions. The hydrogen concentrations are almost zero in the near stoichiometric regions where the methane conversion rate was the highest. This is an additional indication that SR did not contribute significantly to methane conversion under these conditions (steady state operation).

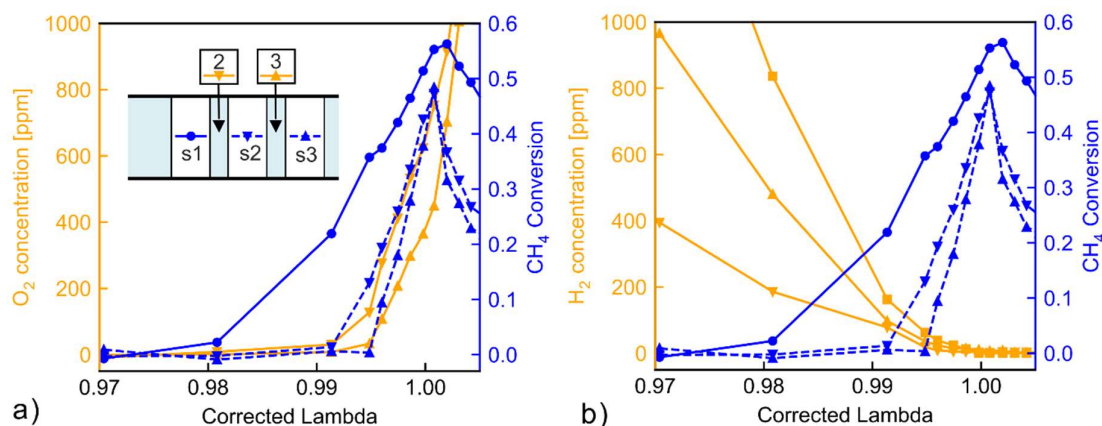


Figure 2:4 Relation between CH₄ conversion rate and a) oxygen concentration at the measurement points 2 and 3 and b) hydrogen concentration at measurement points 2, 3 and 4.

Similar effects were observed at several other catalyst inlet temperatures, i.e. 430, 520, 590 and 660°C as plotted in Figure 2:5. The different inlet temperatures were achieved by changing the engine operating conditions (torque and engine speed). At $\lambda < 1$, the conversion rates were similar in the examined temperature range. Oxygen deficiency rather than temperature was the limiting factor, because methane was only converted through direct oxidation. The conversion rates at $\lambda > 1$ were clearly temperature dependent, as expected. Despite higher GHSV at higher engine loads, THC conversion rates on the lean side increased with increasing temperature.

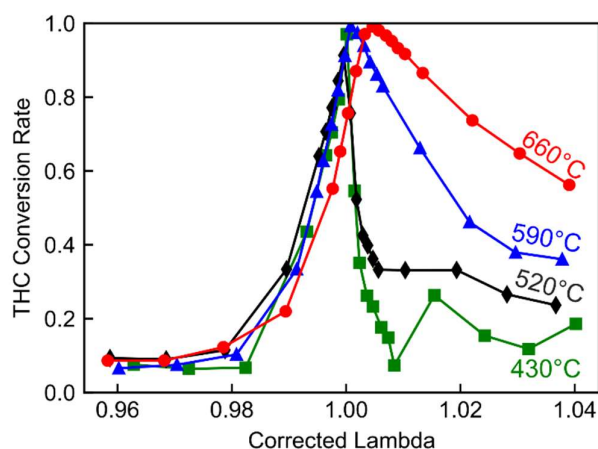


Figure 2:5 THC conversion rate of the complete aftertreatment system at different inlet temperatures (430°C, 520°C, 590°C and 660°C).

2.3 Conversion characteristics in lean to rich transitions

2.3.1 Engine test bench study

Transient λ shifts activate the transition of the oxidation state of both ceria and noble metals, and this has been reported beneficial for methane conversion [96,97]. The two different sized catalyst stages enabled the analysis of phenomena on different time scales. Short time scale phenomena associated with the ceria oxygen storage could only be resolved with the larger, second stage catalyst slices. Longer time scale phenomena (associated to steady state λ changes) could be distinguished clearly only over the slices of the smaller sized first stage catalysts, which provided more precise spatial concentration profiles.

Figure 2:6 presents λ sensor signals (Figure 2:6a) and concentration measurements during λ -step experiments from lean to rich (from $\lambda = 1.03$ to $\lambda = 0.98$) at the measurement points 1 to 8. The λ value at outlet of the second stage (point 8) only dropped to below $\lambda = 1$ ca. 20 s after the inlet λ (point 1) dropped. This is the time needed to deplete the available oxygen storage of ceria at this temperature. The sequential depletion of the oxygen storage capacity was also clearly demonstrated by the sequential increase of the CO concentration from measurement point 1 to 8 (Figure 2:6b). CO concentration increased slowly over time at points 2 to 4, indicating

a slow decay in CO conversion in the first stage catalyst slices. Similar to the steady state result, large amounts of CO were consumed after the first slice, even though upon lean to rich λ shift, O_2 (Figure 2:6d) and NO_x (Figure 2:6c) concentrations immediately decreased to zero at all measurement points downstream of the first slice. This means that the WGS reaction continued to play an important role in CO conversion in transient λ shifts. The THC concentration at point 8 (Figure 2:6e) remained below 100 ppm for 110 s after the λ shift to rich. This corresponds to a conversion of more than 90% of THC, compared to below 10% at the same λ value under steady state ($\lambda_{corr} = 0.971$ for λ sensor value 0.98) in Figure 2:5. It is also clear that a significant part of THC was consumed downstream of point 2, where neither NO_x nor O_2 were present. Under these conditions, SR was the only plausible way for methane conversion in the downstream slices. This means that the transient lean-to-rich step activated an additional pathway of methane conversion through SR. However, THC concentration increased over time, suggesting that the benefits of SR attenuated with time as the reactor remained under rich conditions. This is further confirmed by the decrease in H_2 concentration according to the attenuation of both WGS reaction and SR (Figure 2:6f). Similar to the case of steady state conditions at $\lambda < 1$, significant amounts of ammonia were formed, which tightly followed the behavior of H_2 concentration (Figure 2:6g). Apart from reaction pathways, valuable information on reproducibility can be derived from Figure 2:6. The concentration profiles at measurement point 4 and 5 had only little deviations, even though the measurements were made sequentially by repeating the λ -step (as described in section 2.1.4). Only around 70 ppm of THC concentration difference was observed between measurements at point 4 and 5 at 110s after the step transition, which proves good reproducibility of the engine test bench experiments.

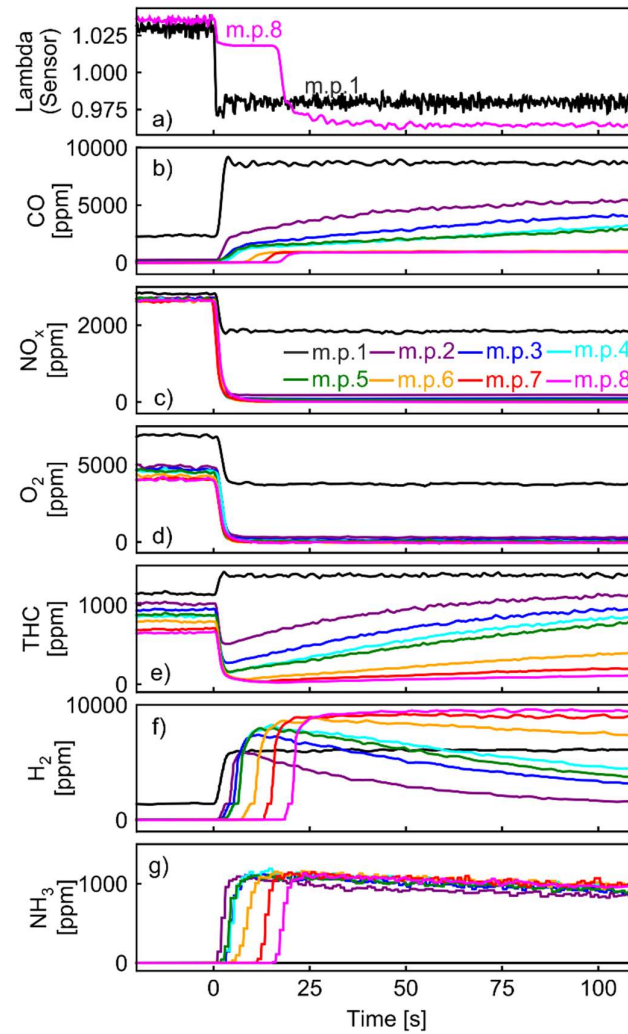


Figure 2:6 Concentration profiles at measurement points 1 to 8 during a λ -step from 1.03 to 0.98.

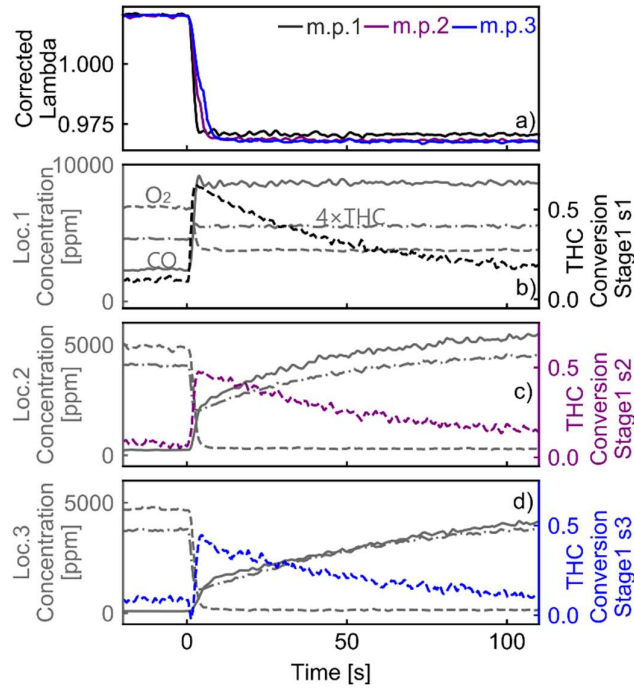


Figure 2:7 Transient λ -step from 1.03 to 0.98. a) Response of corrected λ , b)-d) transient concentration profiles and THC conversion rates for slices of the first stage catalyst.

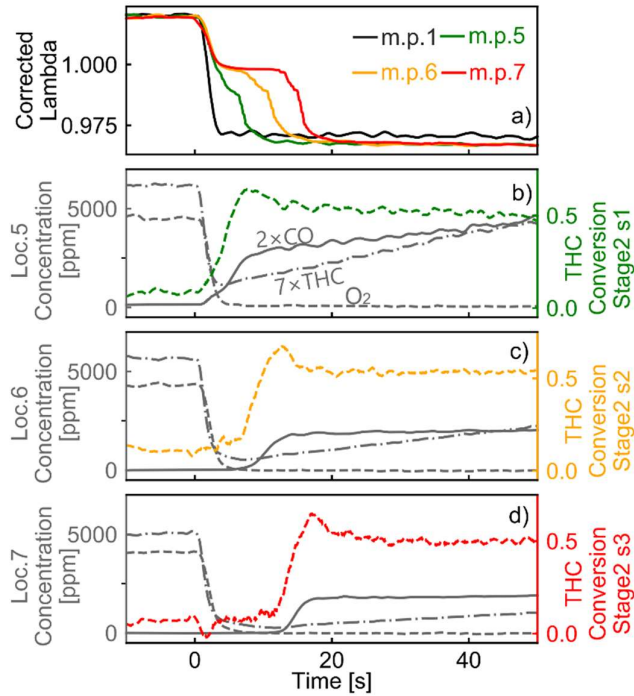


Figure 2:8 Transient λ -step from 1.03 to 0.98. a) Response of corrected λ , b)-d) transient concentration profiles and THC conversion rate for slices of second stage catalyst.

The transient high THC conversion rate at the lean-to-rich shift sheds light on possible strategies to enhance methane conversion in natural gas-fueled vehicles. Therefore, it is of importance to analyze the time scale and the mechanism behind the activation and

deactivation of this conversion enhancement. Local inlet λ values, inlet concentrations and THC conversion rates of the three slices of the first stage catalyst are shown in Figure 2:7. Because these slices had smaller dimensions and relatively lower amount of oxygen storage capacity, the decrease of λ values at the respective slice inlets were fast. THC conversion rates for all first stage slices showed similar behaviors, with a fast increase of conversion rates to about 50% per slice followed by relatively slow decays over time. After 110 s, the THC conversion rate was still at the level of 10% per slice, higher than the corresponding steady state values (10% for the entire system in Figure 2:5). For the slices of the second stage catalyst (Figure 2:8), the decay of THC conversion rates, i.e. of the methane SR reaction was much slower. In fact, the slow decay is only subtly visible in slice 1 of the second stage (Figure 2:8b) and not noticeable in slice 2 and 3 (Figure 2:8c and d). The start of the conversion increase appeared, however, at different times for each slice, even though both reactants, water and methane, were present in the exhaust gas immediately after the λ shift. The conversion in each slice started exactly at the time when the oxygen storage in the previous slice was depleted to the extent that $\lambda = 1$ could no longer be maintained at the selected slice inlet (Figure 2:8a). This is also the point in time when CO started to enter the inlet of the selected slice. Based on Figure 2:8, we can propose that the following process occurred considering that Rh and Pd are catalytically active for SR and ceria is a promoter. Methane adsorbs dissociatively on Rh and Pd during SR, while water is adsorbed and reduced on Ce^{3+} [60,63,65,98]. In a lean-to-rich λ -step, ceria cannot be used immediately to coordinate water after the sharp λ shift, because all sites on ceria are fully oxidized to Ce^{4+} in lean conditions and are not available for reducing water, thus inhibiting the methane SR pathway. Ce^{4+} are reduced with the arrival of oxygen-deprived exhaust gas originating from the rich combustion mixture. Both Rh and Pd are also reduced to Rh^0 and Pd^0 . Reduced ceria together with noble metal sites are able to trigger the onset of methane SR.

The decay of THC conversion rates, however, cannot be explained by the reaction mechanism of different adsorption sites of methane and water alone. The gradual decay continued for the complete measurement time of 110 s, while reduction of bulk ceria lasted for less than 20 s. It is worth noticing that the CO conversion also shows clear decay over time (Figure 2:6b), which resembles methane conversion decay. The WGS reaction is reported to have similar reaction kinetics as methane SR [65]: water dissociates on Ce^{3+} , while CO dissociates on noble metal sites. It is therefore reasonable to assume that the mechanisms of the attenuation of WGS reaction and methane SR are similar.

Methane SR catalysts for hydrogen production are normally working at temperatures above 500°C. However, deactivation is in general not a major concern. The two widely suggested explanations for the deactivation of SR catalysts are sulfur poisoning [99], carbon deposition [100] or their combination [70,100,101]. The two processes are both extremely slow, in particular on noble metal catalysts and deactivation is hardly visible over 10 h measurement time [101,102]. The WGS catalysts are reported to operate at lower temperature and deactivate much faster [68,103]. It is proposed that the deactivation of Ce-containing catalysts relies on the blockage of active sites due to the formation of surface carbonaceous compounds [66–68].

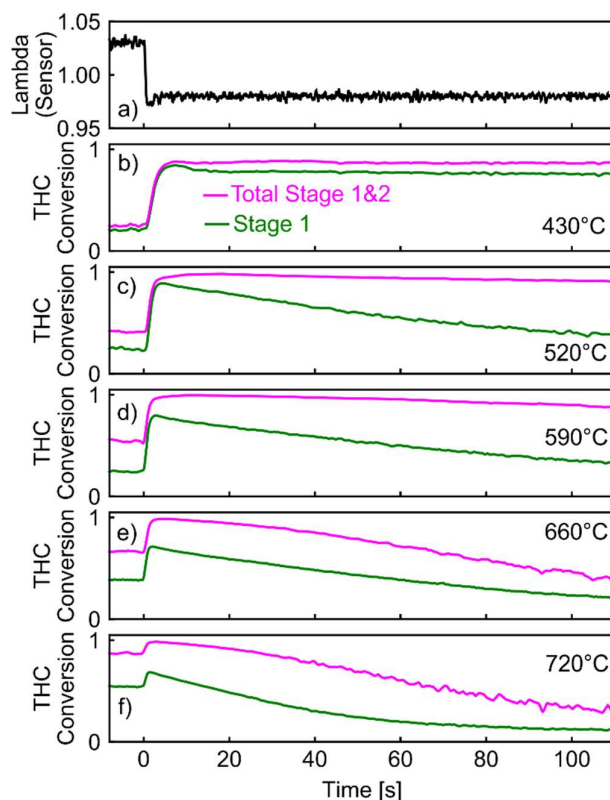


Figure 2:9 THC conversion rate of stage 1 catalyst and the complete system (stage 1 and 2 catalysts) for different engine operating points with different inlet temperatures. The inlet temperature and mass flow rate of each operating points are listed as follow b) 430 °C, 63.1 kg/h, c) 520 °C, 103.1 kg/h, d) 590 °C, 144.2 kg/h, e) 660 °C, 251.0 kg/h, and f) 720 °C, 287.5 kg/h.

To confirm the THC conversion trends and study the temperature effects, the same lean-to-rich λ -step procedure was repeated for different catalyst inlet temperatures as shown in Figure 2:9. At all temperatures, an increase of THC conversion upon shifting to rich conditions was observed. However, the decay of conversion rates after the transient increase took place at different rates. At 430 °C, the decay was so slow that the decrease in THC conversion was hardly visible in the initial 110 s in both the first stage catalyst and in the complete system. As temperature increases, the decay was more pronounced. The fast decay rate at higher temperatures is a result of both higher mass flow rates at the higher engine loads and the acceleration of SR decay due to the temperature effect. At 720 °C, the THC conversion rate of the first stage catalyst stabilized at 10% after 110 s, which is the typical THC conversion rate at this λ for steady state measurements. This confirms that the transient high conversion rate will finally recede to the low conversion rate recorded at steady state. It is widely agreed that PdO reduction completes within seconds above 400 °C [45]. However, in Figure 2:9, the enhanced methane conversion via SR lasts for minutes. This indicates that PdO/Pd transformation has limited impact on SR reaction in the transient λ -step studies and is unlikely the cause for the enhanced methane conversion.

2.3.2 Model gas study

Given the complex components of engine exhaust and the complexity in changing individual parameters during engine operation, various λ -steps from lean to rich were reproduced in a lab-scale reactor with synthetic gas. The aim was to conduct the experiments at similar conditions to the engine experiments introducing specific variations of λ . Figure 2:10 shows that methane conversion increased suddenly after each lean-to-rich step and then decreased with time in all experiments. The behavior is very similar to the behavior observed in Figures 2:6-9 in the case of engine experiments. The deactivation was clearly a reversible process and the catalyst regenerated in the lean period prior to the next shift to rich conditions. As sulfur was absent in the reactor feed and the catalyst had no history of operating under sulfur-containing environment, the sulfur-related deactivation hypothesis can be ruled out. The only reasonable deactivation effect is based on the accumulation of carbonaceous compounds on ceria that are oxidized by oxygen in the lean period. The almost identical methane conversion profiles for steps R1 and R5 indicate that the 10-min regeneration under lean conditions was sufficient to restore the catalyst to the original state. It is also an evidence of good reproducibility for model gas reactor measurements. However, the decay rate of methane conversion was different for steps R1 to R3 and in the order

R1>R2>R3 in agreement with the decreasing CO concentration in the feed gas. This supports the conclusion that CO concentration affected the deactivation rate most probably through the formation of carbonaceous adsorbates. CO is frequently associated to carbonaceous surface species [104–106], especially carbonates. The fact that methane conversion decayed more slowly in the absence of CO, regardless of H_2 compensation (steps R3 and R4) rules out the influence of λ values. Repetition of the same experiment at the inlet temperature of 430 °C (not shown) produced very similar results, except for the methane conversion decay that was slower, in line with the engine experiments of Figure 2:9.

Diffuse reflectance infrared Fourier transform (DRIFT) spectroscopy was used to monitor the evolution of surface species at a lean-to-rich λ -step corresponding to R1 in the model gas reactor experiments and to identify the relative slow deactivation process on the catalyst surface. After alignment of all spectra at 2600 cm^{-1} in order to remove the strong baseline shift due to the changes in the oxidation state of the catalyst (Figure 2:11a), we selected some signals to show their kinetic behavior upon the step change of reaction conditions. Assignment of signals in the spectra is difficult due to the complexity of the catalyst, the presence of cordierite and incomplete knowledge about the composition of the catalyst. While spectra in the lean period were relatively simple and were characterized by signals at 2050, 1639 and 1524 cm^{-1} , their complexity increased significantly after the step indicating the coordination of various species to the components of the catalyst. Assignment can be ambiguous, for example as in the case of the signal at 2169 cm^{-1} that can be attributed to isocyanates coordinated to noble metals [107–109] or alternately to the presence of CO coordinated to Ce^{3+} [110]. The signals at 2230 and 2053 cm^{-1} are unambiguously assigned to isocyanates adsorbed on the support [108,111] and to CO coordinated to noble metals [112], most likely reduced Pd. While all signals appeared very stable after the step, only the shoulder at 1595 cm^{-1} exhibited a slow intensity increase (inset of Figure 2:11a). The temporal behavior of this signal is compared to signals at 2053 and 2169 cm^{-1} in Figure 2:11b. In marked contrast to the signal at 1595 cm^{-1} , the intensity of these two signals stabilized immediately after the step. It is reasonable to associate the slow decay process observed both in the engine and the model gas reactor measurements with the slow intensity increase of this signal. This spectral region is typical of carbonyl compounds such as adsorbed formates and carbonate species [104,106,113]. Signals of carbonates were reported at 1581 cm^{-1} [104], 1598 cm^{-1} [113] and 1600 cm^{-1} [114]. Meunier et al. [115] showed that in a ceria-containing WGS catalyst, two types of formates accumulate on the surface at different rates, which evolve then to carbonates eventually causing catalyst deactivation. Similar correlation between deactivation and carbonates was reported for other WGS catalysts [64,66–68]. The transition from formates to carbonates is significantly faster at higher temperature [116], in agreement with the faster decay of methane conversion at higher temperature in our engine and model gas reactor experiments. Finally, carbonate species are stable at high temperature in reducing conditions, but $Ce_2(CO_3)_3$ can be quickly oxidized and decomposed into CeO_2 and CO_2 in lean environments [113,117], regenerating the catalyst in the lean periods. All these features of carbonates are in line with the deactivation behavior observed in the present work at different scales, from engine test bench to DRIFT measurements, confirming that the catalyst indeed deactivated due to an increasing surface coverage with carbonates.

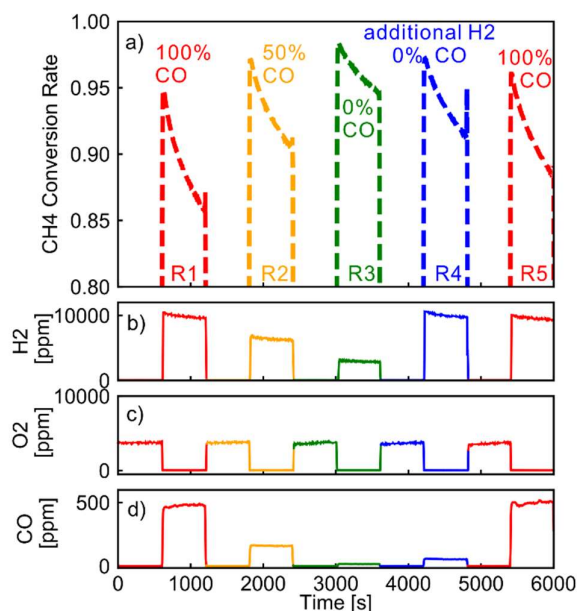


Figure 2:10 a) CH_4 conversion rates and concentrations of b) H_2 , c) O_2 and d) CO in the transient λ -steps in the model gas reactor.

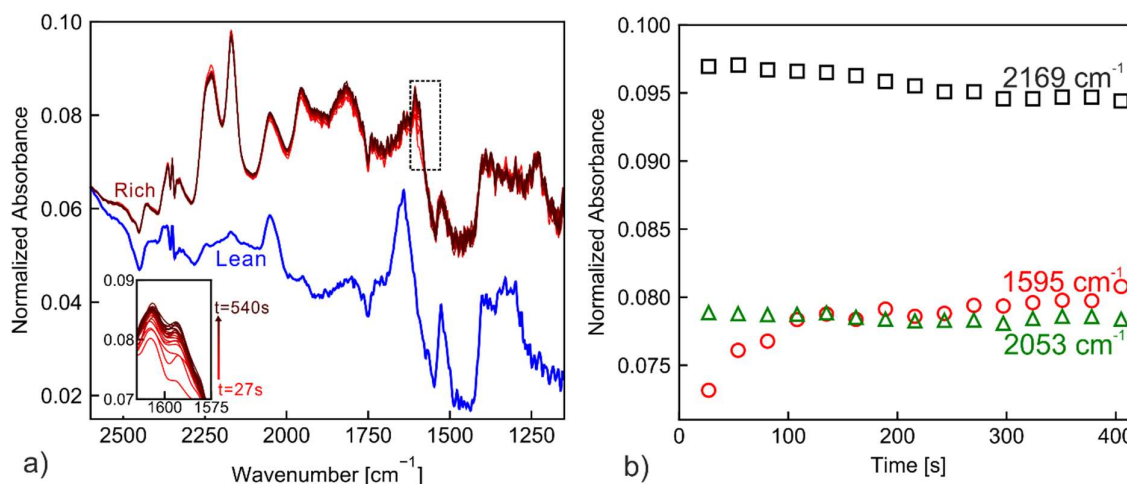
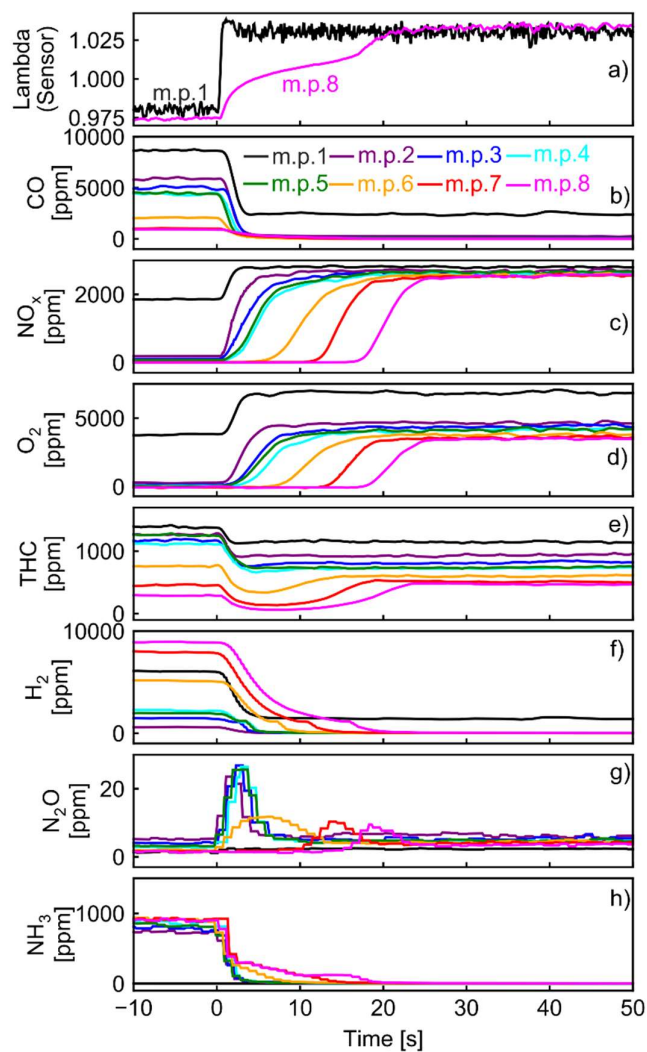


Figure 2:11 a) DRIFTS spectra obtained during transient λ -step from lean to rich feed at 430°C, b) temporal signal intensities at 1595 cm⁻¹, 2053 cm⁻¹ and 2169 cm⁻¹ (after λ -step change at $t = 0$).

2.4 Conversion characteristics in rich to lean transitions

Figure 2:12 shows the concentration profiles in the engine exhaust gas in a transient rich-to-lean λ -step from 0.98 to 1.03. The CO concentrations decreased immediately to nearly zero at all measurement points downstream of the first slice. The NO_x and O₂ concentrations increased sequentially from upstream to downstream, reflecting the gradual oxidation of Ce³⁺ obtained during the rich period. The THC concentration after the slices of the second stage catalyst (measurement points 6, 7, 8) showed a more complex behavior: the initial decrease directly after the λ -step was followed by an increase to a stable value. The same behavior was discernible at measurement point 4 of the first stage catalyst, although much less pronounced. A high THC conversion was observed lasting for around 15 to 20 s. H₂ only decreased slowly compared to CO, due to the remaining SR reaction, which will be discussed in the next paragraph. Traces of ammonia were detected when both NO_x and H₂ were available and N₂O appeared sequentially after each catalyst slice. These transient peaks were surprisingly intensive, as the N₂O concentration measured in steady state λ -sweeps and lean-to-rich jumps did not exceed 10 ppm. At each measurement point, the N₂O concentration reached a maximum when H₂ at the same point decreased to zero, indicating that NO experienced a two-step reduction, first to N₂O and then to either N₂ or NH₃.

Concentrations and THC conversion rates for all slices of the second stage catalyst are shown in Figure 2:13. The transient conversion increase in all slices started immediately after the rich-to-lean λ -step and passed through a maximum value. For slice 2 and 3, the increase in conversion rate occurred earlier than the arrival of oxygen. Therefore, the transient conversion increase was unlikely to occur due to reoxidation of palladium as oxygen was not yet present. The lack of oxygen indicates that it was caused by methane SR rate rather than direct methane oxidation by oxygen. One possible explanation for the increase of methane conversion rate is that the sudden drop of CO concentration allowed more sites on the catalyst to contribute to methane SR, because WGS and methane SR have similar reaction mechanisms and compete for active sites. The occurrence of SR was evidenced by the slight increase in CO concentration (up to 20 s) and positive hydrogen production rate (from measurement point 5 to 8). CO was simultaneously consumed through the WGS reaction under the oxygen-deficient environment. In the absence of the reoxidation of ceria after the λ -step, the observation of CO production on an engine is extremely difficult. Methane SR is always associated with rich conditions and with high CO concentration. Under these conditions, the WGS reaction consumes CO and obscures CO production. The oxidation of ceria during the first 20 s after the λ shift provided a unique environment where the CO production via methane SR could be observed. After the initial THC conversion enhancement, the THC conversion rate returned and stayed at a constant low level (after 20 s). Methane SR was no longer possible with oxidized ceria and excess oxygen. The reaction pathway was limited to methane direct oxidation, where the dissociation of methane was hindered by the excess oxygen adsorbed on the noble methane surfaces [47,48,55].

Figure 2:12 Concentration profiles at measurement points 1 to 8 during a λ -step from 0.98 to 1.03.

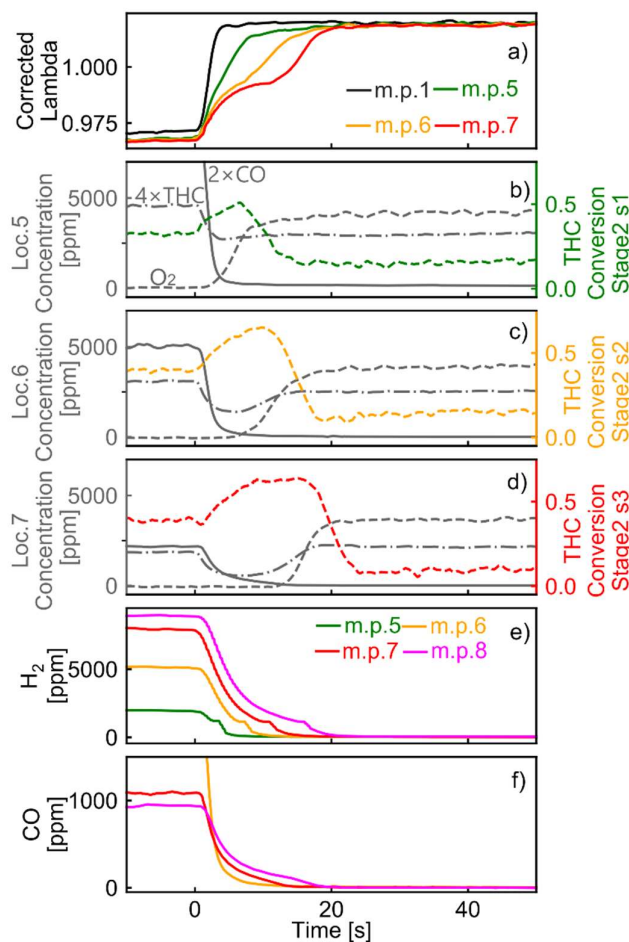


Figure 2:13 Transient λ -step from 0.98 to 1.03. a) Response of corrected λ , b)-d) transient concentration profiles and THC conversion rate for the slices of the second stage catalyst, e) H_2 concentration, and f) CO concentration.

2.5 Conclusions

In this section, a detailed analysis of the behavior of a three-way catalyst in methane combustion exhaust under steady and transient operation with different λ values is presented. Different reaction pathways of methane were identified under steady and transient operation. The special designed sliced catalyst system allowed distinguishing reactions in individual slices, which were subject to different feed compositions. In parallel, targeted experiments in a model gas reactor and in operando DRIFTS allowed further analysis and interpretation of the reaction pathways involved.

In steady state, the low methane conversion was identified as the result of only direct oxidation by oxygen in both rich and lean conditions. A large part of CO was consumed under rich conditions through the WGS reaction evidenced by the generation of hydrogen.

In transient measurements, extremely high methane conversion rates were identified under rich conditions after shifting from lean conditions for a limited time. The large increase of methane conversion rate compared to steady state measurements could be attributed to methane SR. The onset of SR occurred at different instants following depletion of oxygen storage, which is related to the ceria oxidation state. The reaction rates of methane SR decayed over time at temperature-dependent rates. Faster deactivation of SR was observed at higher temperatures. After a moderate time (minutes), methane conversion rates converged to low numbers corresponding to the steady state measurements. Model gas reactor experiments and operando DRIFTS confirmed the methane conversion increase and the deactivation and link the deactivation with surface carbonaceous functional groups (most likely carbonates) related with CO.

In transient λ -steps from fuel rich to fuel lean conditions, a short conversion increase was detected immediately after the switch, caused by a sudden increase of the methane SR rate. These findings have notable implications on natural gas engine catalyst development and the further optimization of engine control strategies. Particularly, transient engine control strategies, e.g. λ periodic oscillations, have the potential to promote the methane conversion by promoting methane SR. The attention of catalyst development should as well be focused on SR characteristics. However, this may require an additional oxidation catalyst to oxidize excess hydrogen and ammonia.

Chapter 3 Sustainable high methane conversion under periodic lean/rich oscillations

Parts of this chapter are published in: M. Wang, P. Dimopoulos Eggenschwiler, D. Ferri, O. Kröcher, *Experimental and modeling-based analysis of reaction pathways on catalysts for natural gas engines under periodic lean/rich oscillations*, *Chem. Eng. J.* 430 (2022) 132848. <https://doi.org/10.1016/j.cej.2021.132848>. And M. Wang, P. Dimopoulos Eggenschwiler, *Modeling of Three Way Catalyst Behavior Under Steady and Transient Operations in a Stoichiometric Natural Gas Fueled Engine*, in: *SAE Tech. Pap. Ser.*, 2021: pp. 1–10. <https://doi.org/10.4271/2021-24-0074>.

In the previous chapter, the important role of SR in promoting methane conversion has been demonstrated. The high conversion of SR, however, attenuates fast under steady state conditions. This chapter analyses the a novel approach to achieve sustainable high methane conversion based on periodic lean/rich oscillations, which result in sustainable high methane conversion. We had applied a targeted procedure to gain insights in catalytic behaviors under different lean/rich oscillations conditions. The important findings of the experiments under oscillating conditions were successfully reproduced and further analyzed with simulations, which were based on the development of a global reaction scheme model. The insights gained in this chapter provide novel and unique explanations on the mechanism of high methane conversion during periodic lean/rich operations, as well as guidance to lean/rich oscillation optimizations even for catalysts with different formulations.

3.1 Experimental

To simplify the system, only the three slices of the second stage catalyst described in Chapter 2 was used for λ oscillation investigations. Four measurement points were available for concentration measurements: at the catalyst inlet, between catalyst slices and at the catalyst outlet. The measurement points were numbered from 1 to 4. An engine operation procedure was designed for measuring the transient periodic lean/rich oscillations. The engine was operated at 1600 rpm and 210 Nm (same as in steady state measurements). Before each measurement, the catalyst was first pre-conditioned by either running the engine under rich ($\lambda_{\text{sensor}} = 0.9$) or lean conditions ($\lambda_{\text{sensor}} = 1.1$) for 5 min. After pre-conditioning, the engine λ value jumped to the designated center λ value (λ_c) and started to oscillate around λ_c with specified frequency at an amplitude of ± 0.025 . All oscillations performed in this study were symmetric (same lean and rich duration), which means that the center λ value (λ_c) was equal to the average λ (λ_{avg}). The concentration profiles of measured species were recorded at 10 Hz frequency at the individual measurement points. The measured concentration profiles were shifted according to the determined analyzer delay time, so that concentration measurements were aligned with λ sensor signals.

3.2 Results of engine test bench measurements

3.2.1 General characteristics

Periodic lean/rich oscillations were studied at $\lambda_{\text{avg}} = 0.990$, oscillation period = 10 s (lean/rich duration each 5 s), and amplitude of 0.025. The selection of a slightly rich λ_{avg} value represents a realistic TWC operating condition to achieve complete reduction of NO_x . Oscillation period of 10 s is well suited for the CLD, FID, NDIR analyzers and H-sense mass spectrometer to capture the general concentration profiles during each oscillation, as the response time of analyzers is below 1.5 s and the refresh frequency is 10Hz.

Figure 3:1 shows the evolution of different exhaust gas species during lean pre-conditioning ($t < 0$) and 15 min after the start of lean/rich oscillations. The total hydrocarbon (THC) concentration is plotted instead of CH_4 , due to faster response of the THC signal from the FID analyzer (10 Hz) compared to the FTIR spectrometer (1 Hz). The FTIR measurements have shown that more than 90% of the THCs were comprised of CH_4 . Therefore, when analyzing THC conversions, only CH_4 reactions are discussed in the following sections.

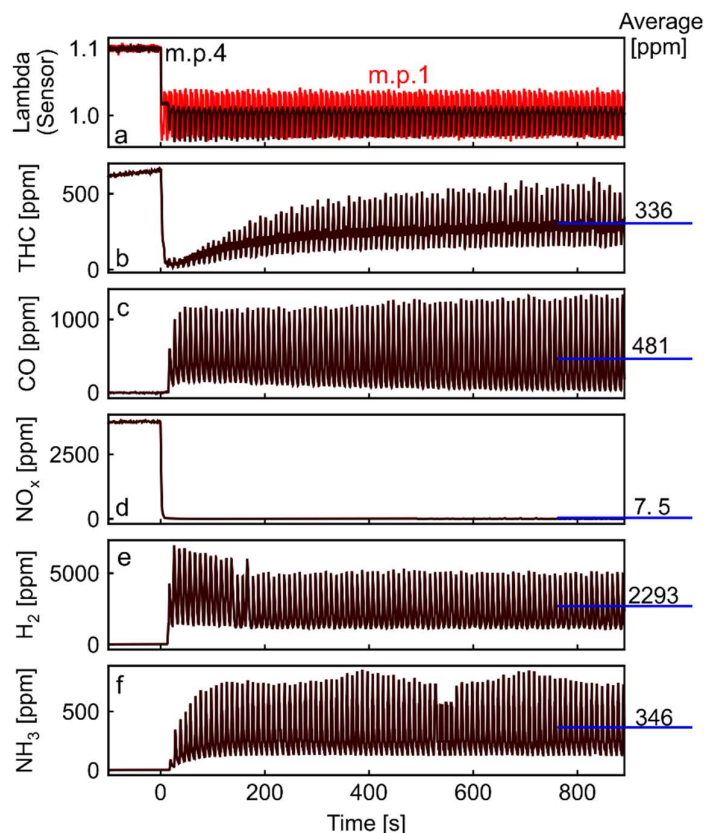


Figure 3:1 a) λ sensor signal at measurement points 1 and 4, b-f) concentration of various species at measurement point 4 during periodic oscillation at $\lambda = 0.990 \pm 0.025$, with period = 10 s (lean/rich duration 5 s). The average concentration of species after 750 s are tabulated on the right side of each plot.

After pre-conditioning, the outlet THC concentration drops significantly upon start of the lean/rich oscillations (Figure 3:1b). During the initial several oscillations, the maximum THC concentration is lower than 100 ppm. However, the THC concentration gradually rose over time and stabilized after around 700 s. More detailed discussion on the THC concentration evolution over time is provided in the following sections. Initially, in section 3.2.2, the reaction schemes during one single oscillation period was analyzed in detail. Following, in section 3.2.3 the discussion focused on the analysis of the multi-period evolution of the THC conversion. The average outlet THC concentration after stabilization was 336 ppm, corresponding to a conversion of 69%. Under steady state conditions, at identical λ (0.990), the outlet THC concentration was 961 ppm, corresponding to a conversion of 11%. This means that the introduction of oscillations led to six times higher THC conversion. The enhancement of THC conversion during λ oscillation is attributed to the activation of the additional reaction pathway of SR. Our previous investigation demonstrated that under rich steady state conditions, ceria sites are deactivated by adsorbed carbonates [98,118], which hinder the occurrence of the SR reaction. The important role of ceria in SR and WGS reactions was demonstrated in numerous studies focusing on different applications [60,63,65,98,119]. During SR and WGS reaction, water is dissociatively adsorbed and reduced on active ceria sites. The deactivation by accumulation of carbonates is overcome through facile oxidation of the carbonates during the lean period with available oxygen [117]. During lean/rich oscillations, at least part of the deactivated ceria sites were regenerated during lean phases, thus activating the methane SR reaction.

The CO emissions during the lean/rich oscillations decreased to on average 481 ppm after stabilization (Figure 3:1c), compared to a steady state concentration of 754 ppm. This is due to the enhanced water gas shift reaction caused by the additional ceria sites that were repetitively freed during periodic operation. The enhanced WGS and SR reactions, however, caused significant increase of the hydrogen emissions to on average 2293 ppm (steady state 320 ppm). The substantial increase of hydrogen concentrations also led to increased ammonia emissions (Figure 3:1f), which was formed by reduction of NO_x by hydrogen. This means that an additional catalyst might be needed in the exhaust gas system for oxidizing residual hydrogen and ammonia to water and nitrogen, respectively.

The average NO_x emissions stayed below 10 ppm without significant NO_x breakthrough (Figure 3:1d), indicating that the oxygen storage capacity (OSC) was not completely oxidized within the 5 s lean period (as expected, since λ_{avg} is below unity).

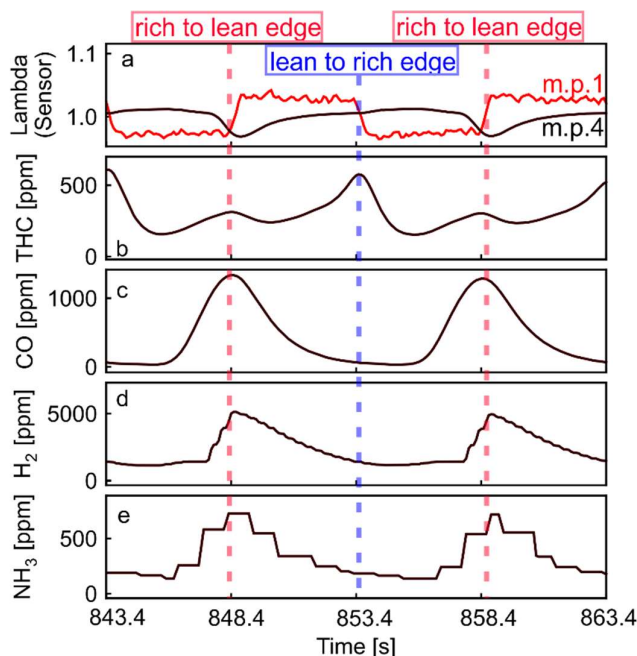


Figure 3:2 a) λ sensor signals and b) THC, c) CO, d) H_2 , and e) NH_3 concentration evolution in cycles after stabilization during periodic oscillation at $\lambda = 0.990 \pm 0.025$, with period = 10 s.

Figure 3:2 zooms into two cycles at $843.4 < t < 863.4$ s (corresponding to the x-axis of Figure 3:1), i.e. after stabilization of the oscillations. In Figure 3:2a, the lean/rich transition edges are marked with two different colors, the rich to lean edges in red and the lean to rich edge in blue. The rich to lean edge represents the λ -step transition to lean after the 5 s rich phase. As expected the maximum concentration of CO, hydrogen and ammonia were measured at this edge. At the end of a rich phase there was insufficient oxygen and the OSC of ceria was depleted, resulting in the conversion of CO through the WGS, which is less efficient than the oxidation by oxygen. Therefore, the CO concentration increased towards the end of the rich phases. Contrarily, CO was efficiently removed by direct oxidation during the lean phases. Hydrogen (Figure 3:2d), similar to CO, was also oxidized by the excess oxygen during the lean phases. Ammonia (Figure 3:2e) exhibited similar concentration profiles as CO and hydrogen, because NH_3 was formed under the net reducing environments either through direct reaction of NO with H_2 ($\text{NO} + \frac{5}{2} \text{H}_2 \rightarrow \text{NH}_3 + \text{H}_2\text{O}$) or indirect pathways involving CO and H_2O [77,78].

The THC concentration pattern in Figure 3:2b is more complex than that of the other species. The transition from lean to rich was accompanied by a strong decrease of the CH_4 concentration. This decrease was followed by an increase of the CH_4 concentration during the second half of rich phase. The transition to the lean phase was characterized by a weak but clear decrease of the CH_4 concentration, which was followed by strong increase leading to the peak at the end of the lean phase. The maximum THC concentration appeared at the lean to rich edge (half a period out of phase with CO and H_2). The phase difference of these concentration peaks suggest different conversion pathways for CH_4 compared to hydrogen and CO. CH_4 direct oxidation in the lean phases exhibits a slow reaction rate due to hindering of CH_4 dissociation by oxygen adsorbed on the catalyst surfaces [47,55,118]. In rich phases, CH_4 is converted through SR at higher reaction rates with the assistance of active ceria sites. This is in contrast to the conversion pathway of CO that mainly relies on fast direct oxidation by oxygen.

3.2.2 Reaction schemes during a single oscillation period

As already described for Figure 3:2b, the THC concentration profile during one oscillation exhibits a 'W' shape with two local minima, one each during the rich and lean phase, and two local maxima at lean to rich and rich to lean edges. Four reaction regimes can be assigned to the characteristic shape, which are schematically presented in Figure 3:3. The oscillation period was normalized to 1, so

that the first half of the period length corresponds to the rich phase and the second half between $t_{\text{norm}} = 0.5$ and 1.0 to the lean phase. In the first reaction regime, the CH_4 concentration decreased with time and reached the first minimum concentration. This regime is linked with the reduction of Ce^{4+} to Ce^{3+} , which gradually activated steam reforming, as water was adsorbed and activated only on active Ce^{3+} sites [60,63,98]. The second reaction regime was characterized by the attenuation of SR. This attenuation can be attributed to the accumulation of carbonates on ceria sites and the increasing CO concentration. The accumulation of carbonates blocked the active Ce^{3+} sites [64,67,68,118] and reduced the reaction rate of SR. At the same time, the CO concentration increased during the second regime (Figure 3:2c), since the remaining OSC is not sufficient to completely oxidize all CO. WGS and SR have similar reaction mechanisms with both CO and CH_4 adsorbed on noble metal sites. Studies have reported competitive adsorption of CO and CH_4 during stoichiometric and rich conditions on noble metal sites [120,121]. It is therefore reasonable to assume competition between WGS and SR. After the transition to lean, i.e. the half period length at 0.5 in Figure 3:3, the THC concentration decreased due to the shift of equilibrium between SR and WGS. CO was immediately oxidized by the abundance of oxygen at $t_{\text{norm}} > 0.5$. The CO concentration decreased, shifting the ratio of WGS and SR towards SR, resulting in a decrease in THC concentration. In the final regime at $t_{\text{norm}} > 0.8$, SR was attenuated again by the excess oxygen in the lean feed. Oxygen vacancies were filled by the supply while metallic state noble metals were oxidized, which play a key role in SR reaction mechanism [63,122]. SR gradually gave way to the less efficient direct oxidation, which resulted in the sharp increase of THC concentrations. Although it was not clearly seen in the concentrations, excess oxygen also reacted with reduced ceria and regenerated ceria carbonates.

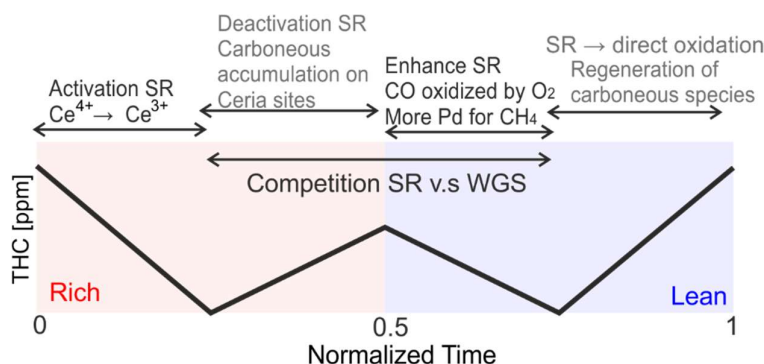


Figure 3:3 Scheme of typical THC concentration profile (W shape) with explanation. The rich to lean transition occurs at $t_{\text{norm}} = 0.5$.

The spatial evolution of THC concentrations during one oscillation period is shown in Figure 3:4. The THC concentration profiles at all three measurement locations have the described 'W' shape. The gas hour space velocity (GHSV) in the first slice is three times as high as for all three slices, while the GHSV for the first two slices combined is 1.5 times as high. The concentration measurements at the three measurement points (m.p.2 to m.p.4) demonstrate the conversion characteristics with different GHSV values. The observation that the 'W' shape is independent of the GHSV confirms the generality of the different reaction regimes.

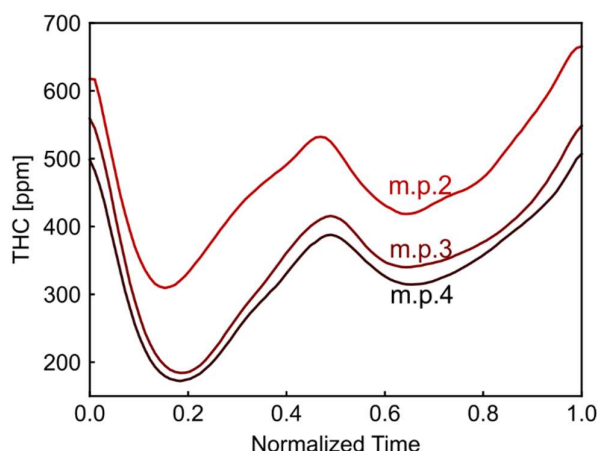


Figure 3:4 THC concentration profiles during one cycle (after stabilization at $t > 700$ s in Figure 3:1 at different measurement points during periodic oscillation at $\lambda = 0.990 \pm 0.025$, with period = 10 s (lean/rich duration 5 s).

3.2.3 Reaction schemes over multiple oscillation periods

In order to analyze closely the upshift of the THC concentration profiles over time in Figure 3:1b, THC concentration profiles from different time instances have been collected and plotted together in Figure 3:5. The curve labels indicate the approximate time at the start of each oscillation (correspond to the time at the x-axis of Figure 3:1). The normalized time was plotted in the x-axis (rich phase $0 < t_{\text{norm}} < 0.5$; lean phase $0.5 < t_{\text{norm}} < 1$). The average THC concentrations raised during cycled operation, in accordance with the observation of Figure 3:1b. The higher average THC concentrations levels with time was caused by the gradual accumulation of carbonates on ceria sites during the periodic oscillations. During rich phases, carbonates slowly formed and deactivated ceria sites. During lean phases, the formed carbonates were partially regenerated by the excess oxygen. Due to the short duration of the lean phases, not all deactivated ceria sites were regenerated. A part of the formed carbonates accumulated over the cycles. Directly after the pre-conditioning, the ceria sites were fully regenerated, exhibiting maximum activity toward SR, thus THC conversion was the strongest (lowest THC concentration). After the oscillation had started, the accumulated carbonates caused the slow deactivation of ceria sites during the cycles, and therefore the slow increase of the average THC concentration with time. Despite these ascending THC concentrations over time, the concentration profiles kept their characteristic 'W' shape throughout the entire measurement time from 0 to 900 s. Finally, the THC concentration stabilized when the deactivation/regeneration balance was reached (Fig 4b, $t > 700$ s).

The same oscillation measurement was repeated with 5 minutes rich pre-conditioning at $\lambda_{\text{sensor}} = 0.9$ (not shown). Despite the different initial conditions and the resulting concentration evolutions, after the time scale of several hundred seconds, the concentration profiles for each species remained the same regardless of the pre-conditioning. In the following sections of this study, only stabilized concentration profiles will be used for further analysis when comparing different cases.

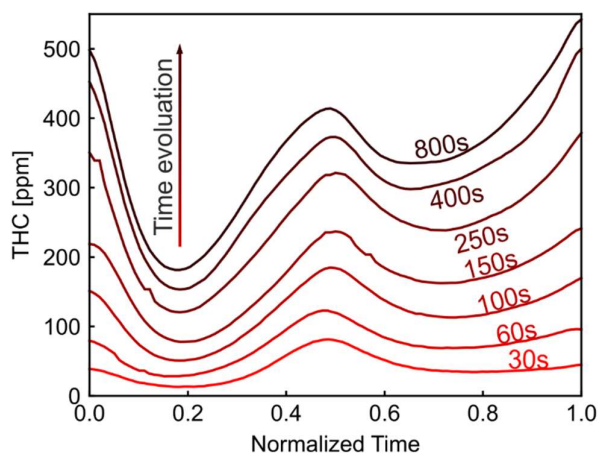


Figure 3:5 THC concentration profiles at different times after the start of oscillations at $\lambda = 0.990 \pm 0.025$, with period = 10 s (lean/rich duration 5 s).

3.2.4 Oscillations entirely on the rich side

So far, the λ_{avg} value was set to 0.990 with maximum λ values larger than one and minimum values below one during oscillations. The long-term enhancement of the THC conversion is mainly ascribed to the regeneration of ceria sites during the lean phases of oscillations. Results of oscillations entirely on the rich side provide supporting evidence for the reaction scheme proposed in Figure 3:3. It can be expected that the 'W' shape as well as the enhanced conversion disappears if λ oscillates on the rich side all the time (maximum $\lambda < 1.00$). We have conducted an experiment with $\lambda = 0.970 \pm 0.025$, in which the oscillation amplitude of the λ value remained always below stoichiometry. Figure 3:6b shows the THC concentrations at the inlet and the outlet of the catalyst during these oscillations. The results of the experiments with $\lambda = 0.980 \pm 0.025$ (maximum $\lambda > 1.00$) are plotted as reference in Figure 3:6a. When comparing Figure 3:6a and b, a significant difference in conversion can be observed, even though both cases oscillated around a center $\lambda < 1.00$ and the inlet THC concentration were very similar (m.p.1). With $\lambda_{\text{avg}} = 0.98$, the oscillation resulted in more than 60% THC conversion, while the conversion was below 10% for average $\lambda_{\text{avg}} = 0.97$. Remarkably, this conversion at $\lambda = 0.97$ was very similar to the steady state THC conversion at the same λ_{avg} . The THC concentration at m.p.4 in Figure 3:6b oscillated at the same frequency as the inlet concentration (m.p.1), while in Figure 3:6a the m.p.4 THC concentration oscillated at a higher frequency. This drop in m.p.4 THC oscillation frequency with $\lambda = 0.970 \pm 0.025$ is the result of change in THC concentration profile during one oscillation period, which

was analyzed in detail in Figure 3:7. Unlike the phase difference between maximum CO and THC concentration shown in Figure 3:2, the THC concentration profile in Figure 3:7b is in phase with the CO concentration. There is no 'W' shape in the THC concentration in Figure 3:7a. This suggests that the conversion mechanism of THC, similar to CO, is now mainly direct oxidation by oxygen. Without regeneration during lean phases, SR is blocked by the deactivated ceria sites covered by carbonaceous species. The change of THC concentration profile and the sharp drop of THC conversion when lowering the λ_{avg} by 1% from 0.98 to 0.97 at otherwise comparable conditions is an important evidence for the explanation provided in Figure 3:3. The finding also implies that in order to benefit from oscillations, the choice of oscillation amplitude should be sufficiently large to ensure oscillations across the threshold of $\lambda = 1$.

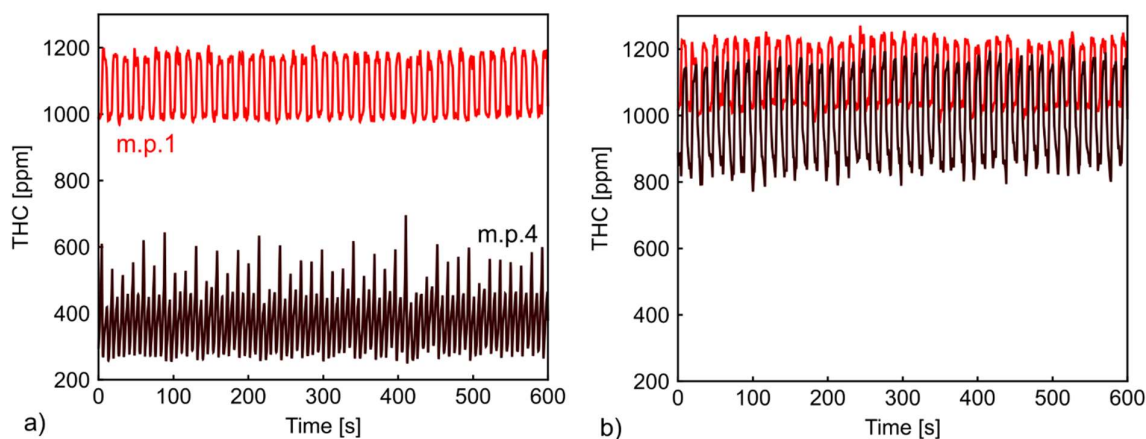


Figure 3:6 Inlet (m.p.1) and outlet (m.p.4) THC concentrations of oscillations with different average λ : a) $\lambda_{\text{avg}} = 0.980$ and b) $\lambda_{\text{avg}} = 0.970$. The other oscillation parameters are the same for a) and b) with an amplitude of 0.025.

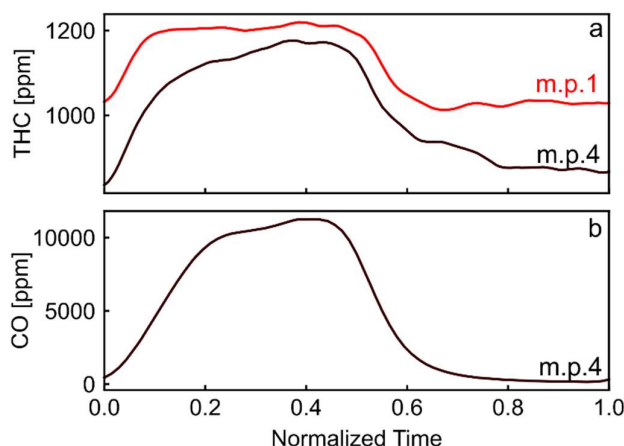


Figure 3:7 a) THC and b) CO concentrations during one oscillation with $\lambda = 0.970 \pm 0.025$ shown in Figure 3:6b.

3.2.5 Influence of different oscillation periods

The oscillation period has significant influence on the chemical state of the catalyst by affecting the duration of different transient processes, e.g. ceria oxidation/reduction, deactivation and regeneration. Figure 3:8a and b demonstrate the change of concentration profiles with different period lengths from 4 s to 14 s (lean/rich duration from 2 s to 7 s) at $\lambda = 0.990 \pm 0.025$ and $\lambda = 1.000 \pm 0.025$ respectively. The advantage of using a 10 Hz resolution analyzer became evident. The typical 1 Hz resolution analyzers would only show a part, if any, of the methane conversion evolution. We used the dimensionless time for the x-axis, which allows direct comparison of the different experiments. In Figure 3:8a, all THC concentration profiles of 4 s, 10 s and 14 s period length show the previously described 'W' shape, however at different conversion levels. The 'W' shaped concentration profile is less pronounced at

the 4 s oscillations, due to relatively short lean/rich durations which are close to the analyzer response time. Compared to the experiment with 14 s period length, the shorter period length resulted in higher concentrations (lower conversion). The increase of concentrations (and consequently the decrease of conversion) was due to the shorter time available for regeneration of the ceria sites. During oscillation with shorter periods, a larger fraction of the catalyst was not regenerated and thus remained inactive. In Figure 3:8b, THC concentration profiles are shown for oscillations around $\lambda = 1.000 \pm 0.025$ at the same oscillation periods as in Figure 3:8a. The THC concentration increased with decreasing oscillation period as well, similar to the observation in Figure 3:8a. The overall THC concentration profile of oscillations at $\lambda_{avg} = 1.000$ (Figure 3:8b) was lower than corresponding oscillations with the same oscillation period but at $\lambda_{avg} = 0.990$ (Figure 3:8a). The higher λ_{avg} means that, during lean conditions, oxygen in the feed was more abundant and the carbonates were regenerated at higher reaction rates. At the same time, the feed gas contained less CO at higher λ_{avg} , which means the carbonates accumulated at slower rate [104,118]. Both effects resulted in more active ceria sites for SR, which explains the relatively high THC conversion when oscillating around $\lambda = 1.000$ compared to $\lambda = 0.990$. The typical 'W' shape THC concentration profile in Figure 3:8b is less pronounced, however still visible for the 10 s and 14 s oscillations. The weakening of concentration changes during reaction regimes 2 and 3 was caused by the combined effect of slower formation of carbonates (thus slower SR deactivation) and less competitive adsorption of CO and CH₄ (less CO in the feed due to higher λ_{avg}). Despite the improved THC conversions in Figure 3:8b compared to Figure 3:8a due to a higher λ_{avg} , this result cannot be generalized. It can be expected for λ_{avg} values far above 1.00 that SR will be suppressed by excess oxygen during the lean phase resulting in a lower THC conversion. The optimization of the λ_{avg} was not further studied and is subject to further research.

The THC concentration at m.p.4 does not always increase monotonically with increasing oscillation period. Figure 3:9 plots the THC concentration profile with further increase of oscillation period to 40 s (20 s lean/rich duration) and compares with 14 s period oscillation (7 s lean/rich duration), both oscillating around $\lambda = 1.000 \pm 0.025$. In contrast to observation in Figure 3:8 (period length range from 4 s to 14 s), the 40 s period oscillation results in on average higher THC concentration than 14 s period oscillations. For oscillation with 40 s period length, the final part of the lean phase ($t_{norm} > 0.8$) is characterized by a constant THC concentration. The THC conversion at $t_{norm} > 0.8$ is higher than the steady state conversion at the same λ ($\lambda = 1.025$). One possible explanation is that the palladium is more active in the form of Pd/PdO mixture shortly after changing into lean conditions from rich periods [43]. Under steady state measurements palladium exists in fully oxidized form at $\lambda = 1.025$. However, a clear understanding of the influence of Pd/PdO transition requires further investigations.

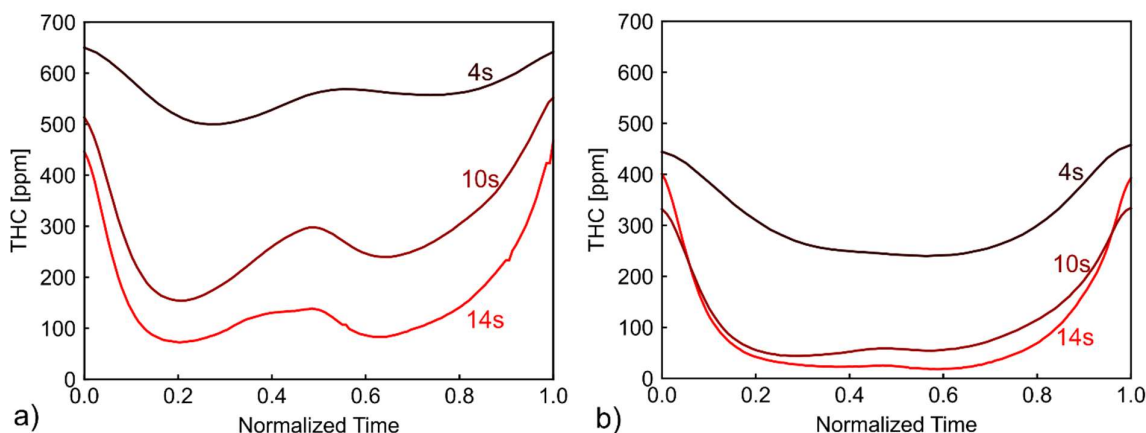


Figure 3:8 THC concentration profiles at m.p.4 during oscillations at a) $\lambda = 0.990 \pm 0.025$ and b) $\lambda = 1.000 \pm 0.025$ with period lengths from 4 s to 14 s.

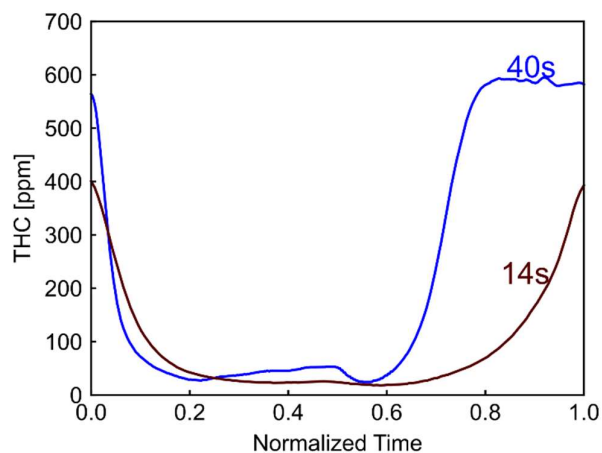


Figure 3:9 THC concentration profiles at m.p.4 during oscillations at $\lambda = 1.000 \pm 0.025$ with period lengths from 14 s to 40 s.

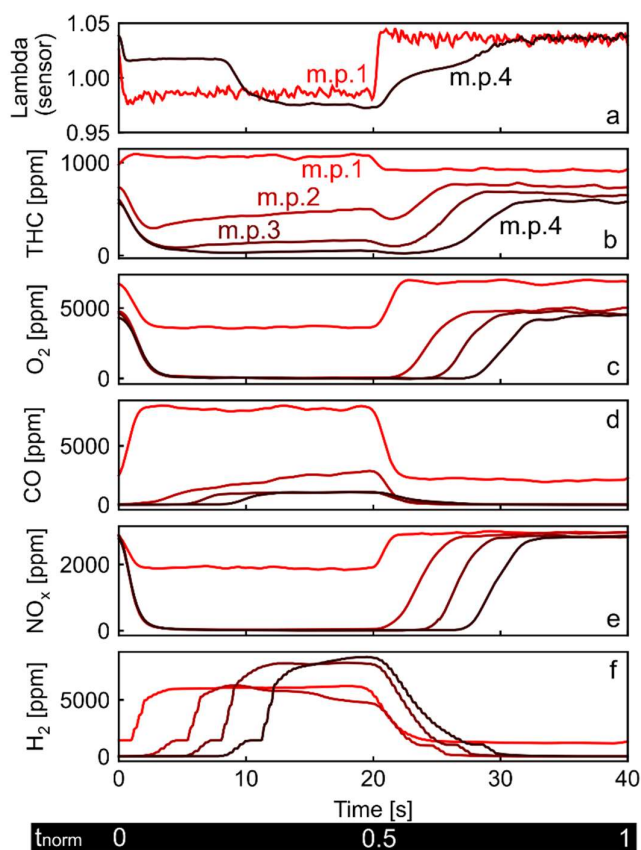


Figure 3:10 a) λ sensor signals and b-f) concentrations of various species at measurement points (m.p.1-4) during one oscillation with period length 40 s.

For detailed analysis of oscillations with period length 40 s, Figure 3:10 plots different species concentrations at different measurement points during one cycle of the oscillation. In Figure 3:10a, the λ signal delay at the outlet (m.p.4) suggests that the approximate time to oxidize and deplete ceria sites is around 11 s and 8 s, respectively (derived from λ sensor signal at m.p.4 in Figure 3:10a), both below the 20 s length of a lean/rich phase. As expected, after the OSC had been completely depleted, CO and H_2 breakthrough appeared. The THC concentration started to become constant (Figure 3:10b: $t > 31$ s) in the lean phase at the point in time when the OSC was completely replenished (Figure 3:10a). In addition, Figure 3:10 provides additional evidences on the reaction pathways. The

THC outlet concentration (m.p.4) stayed below 100 ppm during a large part of the rich phase and the first several seconds of the lean phase (Figure 3:10b). This corresponds to a conversion of more than 90%. During the rich phase, the calculated λ value was around 0.975. Under steady state conditions of the exact same feed, the THC conversion was below 10%. During the rich phase of the λ oscillation, THC was consumed not only in the first slice (m.p.2), but also in the second (m.p.3) and third slices (m.p.4) in Figure 3:10b, where no traces of oxygen were detected (Figure 3:10c). This clearly demonstrates the activation of SR as CH_4 conversion pathway. The efficient conversion of THC via SR attenuated continuously over time in the rich phase, regardless of the OSC oxidation state, which was more obvious in the first two slices. CO (Figure 3:10d), similar to THC under rich conditions, was converted even in slices without oxygen traces, by the water gas shift reaction. The increasing H_2 concentration along the catalyst axis (second half of the rich period in Figure 3:10f) confirmed again the ongoing water gas shift and SR reactions.

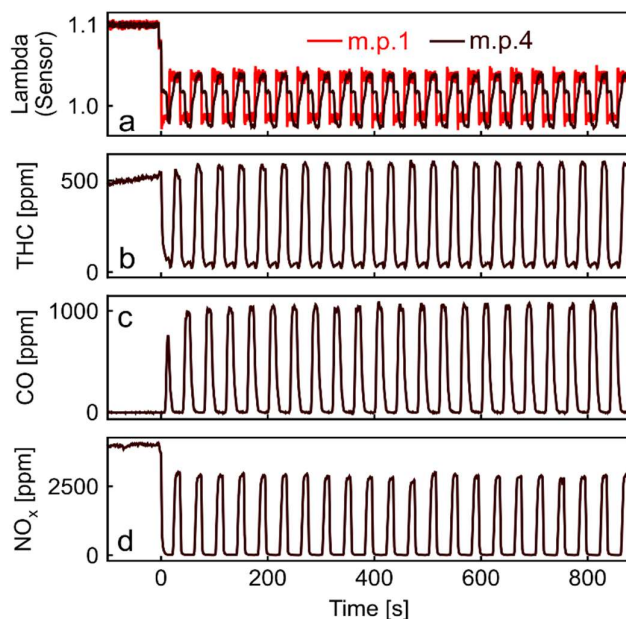


Figure 3:11 a) λ sensor signal at measurement points 1 and 4, b-d) concentrations of various species at measurement point 4 during lean/rich oscillations with period length 40 s.

Figure 3:11 zooms out from single cycle analysis and plots the evolution of species concentrations from the preconditioning phase to 15 min after the start of the lean/rich oscillations with period length of 40 s. The THC concentrations in Figure 3:11 b shows stable peaks from the first oscillation and onward, in contrast to the slow THC concentration evolution observed in the oscillations with period length 10 s (Figure 3:1b). As discussed previously, the period length of 40 s allowed complete depletion and replenishment of the OSC. The 20 s duration of the lean phase was long enough to oxidize all deactivated Ce^{3+} sites covered with carbonates. For each cycle, the initial state of ceria sites was identical (all sites were oxidized to Ce^{4+}). With a period length of 10 s, as discussed in section 3.2 (Figure 3:1), the 5 s duration of the lean/ rich phase was below the time scale for complete ceria oxidation and reduction, respectively. Consequently, the carbonates on the ceria sites could not be fully regenerated during the short 5 s lean phase. The accumulated carbonates caused the slow stabilization of the THC concentration profile in Figure 3:1b (0 - 600 s). Figures 3:11c and d plot the CO and NO_x concentrations during oscillations with 40 s period length. Due to the long duration of each lean/rich period, both CO and NO_x exhibits strong concentration peaks, which is undesirable in real TWC operations. This observation, together with the THC concentration behavior give implications that when optimizing oscillations, lean/rich phase durations should be kept below the time needed for complete depletion or replenishment of the OSC, in order to achieve best catalyst performance.

3.3 Analysis of the chemical processes during the oscillations by means of simulations

3.3.1 Model setup

A one dimensional model is constructed to simulate the closed coupled three-way catalyst in commercial software Exothermia Suite. The catalyst dimension was derived from the experimental parts. Heat transfer by forced convection between the gas phase and solid phase was resolved. The thermodynamic parameters of the substrate were taken from the relevant materials. The reaction heat release or consumption was modeled as a heat source. Apart from the channel scale heat transfer, the convective heat transfer from the catalyst boundary to the atmosphere was as well modeled.

Previous studies have discussed the effect of different mass transfer models and conclude that the implementation of a 1-d diffusion model is the optimal choice for catalyst modeling, balancing the computational effort and the result accuracy [84]. In this study, the washcoat was discretized into 10 cells in the direction vertical to the catalyst channel (1D intralayer mesh). The mass transfer inside the porous washcoat was modeled by the parallel pore model. In this model, the total diffusivity was estimated by porosity, mean pore size and tortuosity of the material. The porosity and mean pore size were taken from the work of Hayes et al. [123], who has studied similar washcoat materials. The tortuosity was set at 0.5, lying in the range suggested by [123].

In total 13 active species were included in the chemical reaction model. C_2H_6 was included in the reaction species to represent the non-methane hydrocarbons in natural gas engine exhaust. C_2H_6 was identified as the most abundant NMHC in the exhaust gas of the engine by the FTIR measurements.

The inlet concentrations of each species were set strictly according to measurements from our engine test bench and were subject to change under different operating conditions. Inlet temperature and mass flow rate follows measurement values as well. Global chemical reactions were modeled with a Langmuir-Hinshelwood scheme. 17 reactions are included in the reaction scheme (Reaction 1-17), as listed in Table 3:1.

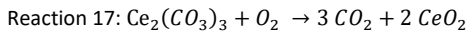
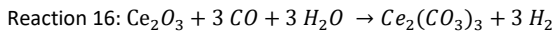
Reaction	Reaction rate function	A_i [mol*K/s/m ³]	E_i [J/mol]
Reaction 1: $H_2 + \frac{1}{2} O_2 \rightarrow H_2O$	$A_1 e^{-\frac{E_1}{RT}} \frac{p_{H_2} p_{O_2}}{G_1}$	1e21	1.05e5
Reaction 2: $CO + \frac{1}{2} O_2 \rightarrow CO_2$	$A_2 e^{-\frac{E_2}{RT}} \frac{p_{CO} p_{O_2}}{G_2}$	5e18	9.5e4
Reaction 3: $CH_4 + 2 O_2 \rightarrow CO_2 + 2 H_2O$	$A_3 e^{-\frac{E_3}{RT}} \frac{p_{CH_4} p_{O_2}}{G_3}$	4e20	1.51e5
Reaction 4: $C_2H_6 + \frac{7}{2} O_2 \rightarrow 2 CO_2 + 3 H_2O$	$A_4 e^{-\frac{E_4}{RT}} \frac{p_{C_2H_6} p_{O_2}}{G_4}$	1e19	1.1e5
Reaction 5: $CO + NO \rightarrow CO_2 + \frac{1}{2} N_2$	$A_5 e^{-\frac{E_5}{RT}} \frac{p_{CO} p_{NO}}{G_5}$	8e17	8e4
Reaction 6: $NO + \frac{5}{2} H_2 \rightarrow NH_3 + H_2O$	$A_6 e^{-\frac{E_6}{RT}} \frac{p_{NO} p_{H_2}}{G_6}$	1.5e20	1e5
Reaction 7: $NH_3 + \frac{3}{2} NO \rightarrow \frac{5}{4} N_2 + \frac{3}{2} H_2O$	$A_7 e^{-\frac{E_7}{RT}} \frac{p_{NH_3} p_{NO}}{G_7}$	5e18	1.2e5
Reaction 8: $NH_3 + \frac{3}{4} O_2 \rightarrow \frac{1}{2} N_2 + \frac{3}{2} H_2O$	$A_8 e^{-\frac{E_8}{RT}} \frac{p_{NH_3} p_{O_2}}{G_8}$	2e18	1.2e5

Reaction 9:	$\text{CO} + \text{H}_2\text{O} \rightarrow \text{CO}_2 + \text{H}_2$	$A_9 e^{-\frac{E_9}{RT}} \frac{p_{\text{CO}} p_{\text{H}_2\text{O}} E q \Phi_{\text{Ce}} f_1(\phi_{\text{Ce}_2\text{O}_3})}{G_9}$	4e13	9e4
Reaction 10:	$2 \text{CeO}_2 + \text{H}_2 \rightarrow \text{Ce}_2\text{O}_3 + \text{H}_2\text{O}$	$A_{10} e^{-\frac{E_{10}}{RT}} \Phi_{\text{Ce}} \phi_{\text{CeO}_2} p_{\text{H}_2}$	2e7	6e4
Reaction 11:	$2 \text{CeO}_2 + \text{CO} \rightarrow \text{Ce}_2\text{O}_3 + \text{CO}_2$	$A_{11} e^{-\frac{E_{11}}{RT}} \Phi_{\text{Ce}} \phi_{\text{CeO}_2} p_{\text{CO}}$	8e5	6e4
Reaction 12:	$\text{Ce}_2\text{O}_3 + \text{NO} \rightarrow 2 \text{CeO}_2 + \frac{1}{2} \text{N}_2$	$A_{12} e^{-\frac{E_{12}}{RT}} \Phi_{\text{Ce}} \phi_{\text{Ce}_2\text{O}_3} p_{\text{NO}}$	1e6	6e4
Reaction 13:	$\text{Ce}_2\text{O}_3 + \frac{1}{2} \text{O}_2 \rightarrow 2 \text{CeO}_2$	$A_{13} e^{-\frac{E_{13}}{RT}} \Phi_{\text{Ce}} \phi_{\text{Ce}_2\text{O}_3} p_{\text{O}_2}$	4e7	5e4
Reaction 14:	$\text{CH}_4 + \text{H}_2\text{O} \rightarrow \text{CO} + 3 \text{H}_2$	$A_{14} e^{-\frac{E_{14}}{RT}} \frac{p_{\text{CH}_4} p_{\text{H}_2\text{O}} \Phi_{\text{Ce}} f_2(\phi_{\text{Ce}_2\text{O}_3})}{G_{14}}$	6.5e13	1.1e5
Reaction 15:	$\text{C}_2\text{H}_6 + 2 \text{H}_2\text{O} \rightarrow 2 \text{CO} + 4 \text{H}_2$	$A_{15} e^{-\frac{E_{15}}{RT}} \frac{p_{\text{C}_2\text{H}_6} p_{\text{H}_2\text{O}} \Phi_{\text{Ce}} f_2(\phi_{\text{Ce}_2\text{O}_3})}{G_{15}}$	1e15	1.1e5
Reaction 16:	$\text{Ce}_2\text{O}_3 + 3 \text{CO} + 3 \text{H}_2\text{O} \rightarrow \text{Ce}_2(\text{CO}_3)_3 + 3 \text{H}_2$	$A_{16} e^{-\frac{E_{16}}{RT}} \Phi_{\text{Ce}} \phi_{\text{Ce}_2\text{O}_3} p_{\text{CO}} p_{\text{H}_2\text{O}}$	6e10	1.3e5
Reaction 17:	$\text{Ce}_2(\text{CO}_3)_3 + \text{O}_2 \rightarrow 3 \text{CO}_2 + 2 \text{CeO}_2$	$A_{17} e^{-\frac{E_{17}}{RT}} \Phi_{\text{Ce}} \phi_{\text{Ce}_2(\text{CO}_3)_3} p_{\text{O}_2}$	4e6	5e4

Table 3:1 List of reactions and reaction rate functions

The reaction rates were modeled as $A e^{-E/RT} \Pi_k p_k / G$. $\Pi_k p_k$ is the product of partial pressure of all reactants. G is the inhibition factor. The introduction of an inhibition factor has been proved as an efficient way to include competition for active sites for global reaction models by many previous works [89,90,124]. For NO_x reduction reactions, the inhibition factors were set following the pioneering work from Voltz et al. [88]. For reaction 2 (CO oxidation reaction), two species inhibition coefficients were included in the reaction rate formulation, CO self-inhibition and NO inhibition. CO self-inhibition effect is a known phenomenon [125] and is usually modeled by a second order inhibition factor. NO competes for active Pd/Rh sites with O_2 and the competition has been modeled with a 0.7 order inhibition factor [89]. The same NO/ O_2 competition also affects oxidation of C_2H_6 and CH_4 , therefore these reactions have identical formulations of the NO inhibition factor. In addition, for hydrocarbons, there is a competition for adsorption sites with CO, which has been mostly modeled by a second order inhibition [88,89,124].

The following two reactions on ceria sites were introduced in the model, representing the previously discussed deactivation and regeneration reactions of active ceria sites:



Reaction 16 describes the slow deactivation process related to the formation of carbonates, widely reported for water gas shift environments [64,67,68]. During the lean phase, the carbonate covered ceria sites are regenerated according to reaction 17. Under these conditions $\text{Ce}_2(\text{CO}_3)_3$ is oxidized to CeO_2 , which can be reduced back to active Ce_2O_3 sites in rich exhaust gas. The influence of activated Ce^{3+} sites on methane SR reaction rate was implemented in the model by insertion of a linear term dependent on the surface coverage of active Ce_2O_3 . The MSR reaction rate function can be written as:

$$R_{\text{MSR}} = A_{14} e^{-\frac{E_{14}}{RT}} p_{\text{CH}_4} p_{\text{H}_2\text{O}} \Phi_{\text{Ce}} f_2(\phi_{\text{Ce}_2\text{O}_3}) / G_{14}$$

In which Φ_{Ce} is the total amount of ceria sites, $\phi_{\text{Ce}_2\text{O}_3}$ is the surface coverage of Ce_2O_3 , G_{14} is the inhibition factor and f_2 is a linear function of $\phi_{\text{Ce}_2\text{O}_3}$, here $f_2(\phi_{\text{Ce}_2\text{O}_3}) = \phi_{\text{Ce}_2\text{O}_3} \cdot G_{14}$ contains a high order oxygen inhibition term, representing the oxygen inhibition

effect caused by oxidizing metallic state noble metals and removing oxygen vacancies. A table of all the inhibition factor functions are presented in Table 3:2.

Inhibition factor functions
$G_1 = G_T G_{1_NO} = T(1 + k_{1_NO} p_{NO}^{0.7})$
$G_2 = G_T G_{1_CO} G_{1_NO} = T(1 + k_{1_CO} p_{CO})^2 (1 + k_{1_NO} p_{NO}^{0.7})$
$G_3 = G_T G_{2_CO} G_{2_NO} G_{2_O_2} = T(1 + k_{2_CO} p_{CO})^2 (1 + k_{2_NO} p_{NO}^{0.7}) (1 + k_{2_O_2} p_{O_2})^2$
$G_4 = G_T G_{2_CO} G_{2_NO} = T(1 + k_{2_CO} p_{CO})^2 (1 + k_{2_NO} p_{NO}^{0.7})$
$G_5 = G_T G_{3_CO} G_{3_NO} = T(1 + k_{3_CO} p_{CO})^2 (1 + k_{3_NO} p_{NO}^{0.7})$
$G_6 = G_T G_{3_CO} G_{3_NO} = T(1 + k_{3_CO} p_{CO})^2 (1 + k_{3_NO} p_{NO}^{0.7})$
$G_7 = G_T = T$
$G_8 = G_T = T$
$G_{14} = G_T G_{2_CO} G_{2_NO} G_{14_O_2} = T(1 + k_{2_CO} p_{CO})^2 (1 + k_{2_NO} p_{NO}^{0.7}) (1 + k_{14_O_2} p_{O_2})^6$
$G_{15} = G_T G_{2_CO} G_{2_NO} G_{14_O_2} = T(1 + k_{2_CO} p_{CO})^2 (1 + k_{2_NO} p_{NO}^{0.7}) (1 + k_{14_O_2} p_{O_2})^6$

Table 3:2 List of inhibition factor functions

3.3.2 Modeling result of steady state λ -sweep

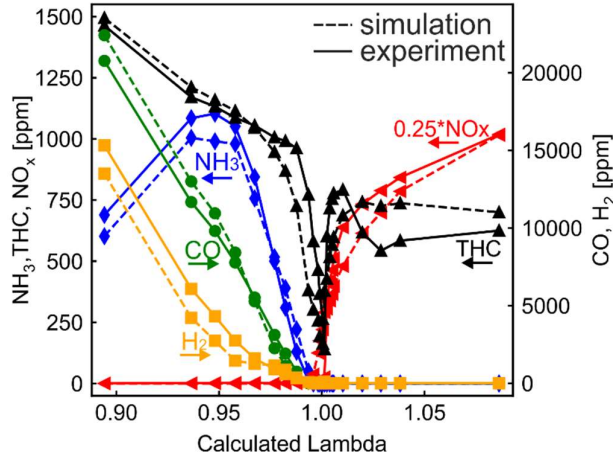
Figure 3:12 Predicted and measured concentrations of various species at m.p.4 during steady state λ -sweep.

Figure 3:12 compares the predicted and measured concentration of five species at the outlet of the catalyst under steady state λ -sweep. The model successfully predicted the characteristic behavior of THC that the outlet concentration drops sharply around the stoichiometry and quickly returns to high level after only a slight deviation from the stoichiometry. Analysis of the CH_4 reaction pathway revealed that the introduction of methane SR reaction contributes only a negligible amount of CH_4 (not shown), due to the high surface coverage with $Ce_2(CO_3)_3$ in the rich steady state. Ammonia emission first increased with increasing λ , with more NO_x

available in the raw exhaust gas of the engine, and then decreased to zero at around stoichiometric conditions due to insufficient reducing agent. The crossover of NO_x and CO/H_2 at around stoichiometry is also captured accurately.

3.3.2 Modeling result of λ oscillations

After the predictive model was validated against steady state λ -sweep, the model was fed with data to simulate oscillations under the same reaction parameters. The inlet concentrations of the rich and lean phase were derived from the concentrations of oscillations at $\lambda = 0.990 \pm 0.025$, tabulated in Table 3:2. The simulation started from a rich preconditioning phase, in which 100% of all ceria sites were covered by $\text{Ce}_2(\text{CO}_3)_3$. The shown results are taken from already stabilized oscillations. Figure 3:13 provides a comparison of predicted and measured concentrations of different species during one oscillation ($\lambda = 0.990 \pm 0.025$, period length = 14 s). The model produced a 'W' shaped THC concentration profile, similar to the observed curve in our measurements. The first local minimum of THC concentration occurred at the same time when the predicted CO and H_2 concentration starts to rise. After the λ -step change from rich to lean at $t_{\text{norm}} = 0.5$, the modelled THC concentration dropped, due to a sudden drop of CH_4 in the lean feed gas as well as the implemented CO inhibition factor in the SR reaction. The model predicted lower CO concentrations than measurements showed under lean conditions ($t_{\text{norm}} > 0.5$). One possible explanation is the mixing of the gases in the measurement device, which had a certain volume and did not allow ideal plug-flow reactor behavior. Figure 3:14 compares the modeled CH_4 conversion rate via CH_4 oxidation by oxygen with SR during one oscillation cycle. During the rich phase ($t_{\text{norm}} < 0.5$), CH_4 direct oxidation was hindered by the lack of oxygen and SR was absolutely dominant. After the switch to a lean feed at $t_{\text{norm}} > 0.5$, SR gradually decreased to zero because of the excess oxygen. The reaction rate of CH_4 direct oxidation gradually surpassed the SR. At the same time, the surface carbonates dissociated as cerium were oxidized by oxygen.

	O_2	NO	H_2	CO	CH_4	C_2H_6	CO_2	Temperature
	[ppm]	[ppm]	[ppm]	[ppm]	[ppm]	[ppm]	[ppm]	[°C]
Rich	2953	1585	7182	9910	941	200	87190	521
Lean	5585	2636	1540	2716	399	160	91360	521

Table 3:3 Concentrations and temperatures used as model input to simulate the lean and rich section of oscillations at $\lambda = 0.990 \pm 0.025$.

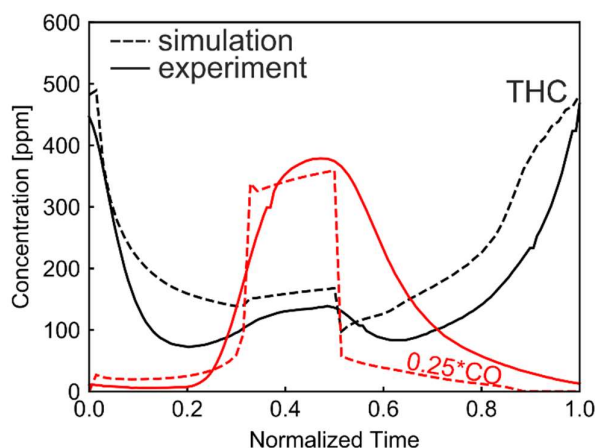


Figure 3:13 Predicted and measured concentrations of CO and THC during one oscillation at $\lambda = 0.990 \pm 0.025$, period = 14 s.

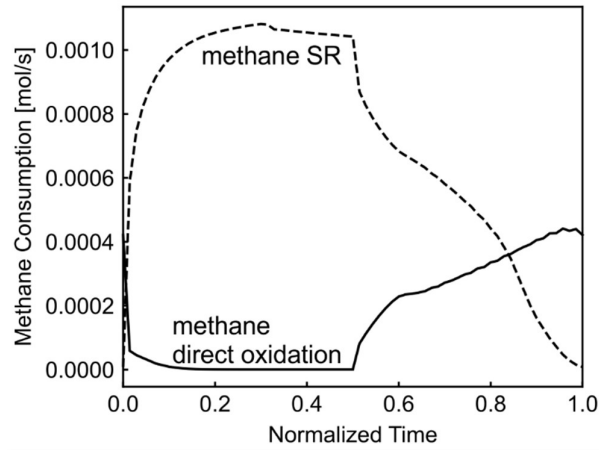


Figure 3:14 Reaction pathways of CH₄ via direct oxidation and SR during one oscillation at $\lambda = 0.990 \pm 0.025$, period = 14 s.

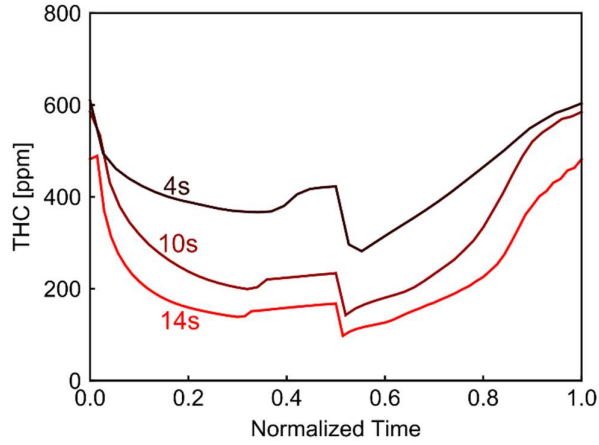


Figure 3:15 Model-predicted THC concentration profiles during oscillations with a period length from 4 s to 14 s ($\lambda = 0.990 \pm 0.025$).

Figure 3:15 plots the modeled THC concentrations during oscillations with different period lengths. Similar to the observation in Figure 3:8a, the model predicted an increase of the concentration profiles with decreasing period length of the oscillations. Based on the simulation model encompassing ceria oxidation/reduction reactions (Table 3:1), surface coverage fraction of ceria compounds (Ce_2O_3 , CeO_2 , $\text{Ce}_2(\text{CO}_3)_3$) could be derived. The surface coverage of the three compounds were determined by equations $\phi_{\text{Ce}_2\text{O}_3} = 2 \frac{[\text{Ce}_2\text{O}_3]}{\Phi_{\text{Ce}}}$, $\phi_{\text{CeO}_2} = \frac{[\text{CeO}_2]}{\Phi_{\text{Ce}}}$ and $\phi_{\text{Ce}_2(\text{CO}_3)_3} = 2 \frac{[\text{Ce}_2(\text{CO}_3)_3]}{\Phi_{\text{Ce}}}$, where $\Phi_{\text{Ce}} = 2 \times [\text{Ce}_2\text{O}_3] + 2 \times [\text{Ce}_2(\text{CO}_3)_3] + [\text{CeO}_2]$ stands for the total amount of ceria concentrations. As already discussed in previous sections, only Ce_2O_3 was active for the H_2O dissociative adsorption and reduction step of SR, while both CeO_2 and $\text{Ce}_2(\text{CO}_3)_3$ were not active sites. The modeled state of surface ceria over the catalyst length during oscillations with different periods is shown in Figure 3:16. Four characteristic time instants have been chosen. At $t_{\text{norm}} = 0$, λ underwent the transition from lean to rich, while at $t_{\text{norm}} = 0.5$, λ underwent the reverse transition from rich to lean.

Figure 3:16a shows the results for oscillations with a period length of 4 s. At $t_{\text{norm}} = 0$, after 2 s of lean feed, ceria was fully oxidized (CeO_2 , brown areas) in the first millimeters of the catalyst inlet. In the downstream only a small part comprised of Ce_2O_3 , while the largest part of the catalyst towards the outlet was covered with $\text{Ce}_2(\text{CO}_3)_3$ (blue areas). When rich feed entered the catalyst at $t_{\text{norm}} > 0$, the CeO_2 reduction started. At $t_{\text{norm}} = 0.25$, a large part of the CeO_2 was reduced to Ce_2O_3 (red areas). The reduction of CeO_2 to Ce_2O_3 corresponded to the SR activation stage, the first branch of the characteristic 'W' shape in Figure 3:3. The rich feed continued up to $t_{\text{norm}} = 0.5$, during which CeO_2 reduction to Ce_2O_3 continued until CeO_2 was fully reduced. The CO in the rich feed was not only increasing the amount of Ce_2O_3 , it started also to form small amounts of $\text{Ce}_2(\text{CO}_3)_3$ (more distinctive in the Figs. 19b and 19c at t_{norm}

= 0.5 in the inlet). The formation of $\text{Ce}_2(\text{CO}_3)_3$ corresponded to the attenuation of SR and to the second branch of the characteristic 'W' shape in Figure 3:3. At $t_{\text{norm}} > 0.5$, lean feed with excess oxygen entered the catalyst, which oxidized Ce_2O_3 as well as the small fraction of the $\text{Ce}_2(\text{CO}_3)_3$ near the inlet ($t_{\text{norm}} = 0.75$). The decrease of the Ce_2O_3 fraction corresponded to further attenuation of SR and to the fourth part of the 'W' shape. The third branch of the 'W' shape, the SR increase after $t_{\text{norm}} > 0.5$, was not due to ceria site changes and thus not to be seen in Figure 3:16, but has been discussed in the previous section with Figure 3:3. However, by the end of the lean period ($t_{\text{norm}} = 1$, due to periodicity represented by the plot $t_{\text{norm}} = 0$), the majority of the catalyst surface still comprised of $\text{Ce}_2(\text{CO}_3)_3$ (blue area). The reduction/oxidation cycle ensured that at least part of the catalyst was active for SR (covered by Ce_2O_3 during the rich period), preventing full SR deactivation.

The discussed reduction/oxidation process of the ceria compounds was similar for oscillations with longer period lengths (10 s and 14 s in Figure 3:16b and Figure 3:16c respectively). Longer oscillation period length means that oxygen penetrated longer into the catalyst length and brought more ceria into oxidation/reduction cycle. Compared to Figure 3:16a, the completely deactivated catalyst section, fully covered with $\text{Ce}_2(\text{CO}_3)_3$ was significantly shorter in Figures 3:16b and c (10 s and 14 s period length, respectively). The fraction of the Ce_2O_3 covered surfaces (red area) in Figs. 19b and 19c is higher than with the shorter period oscillations in Figure 3:16a. More Ce_2O_3 corresponded to more conversion via SR and thus additional methane abatement, consistent with Figure 3:8a and Figure 3:15.

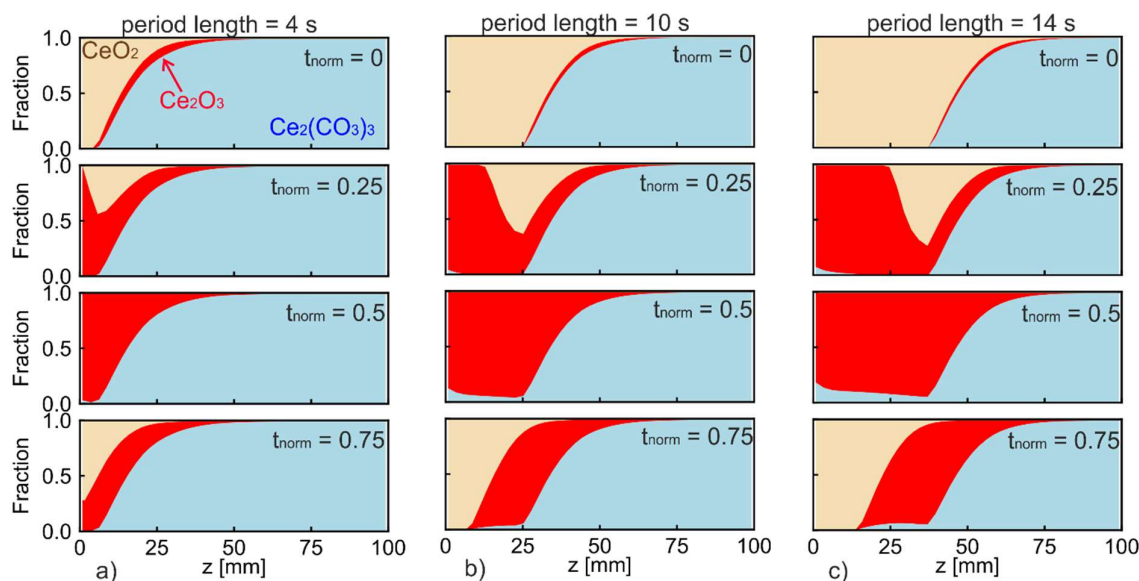


Figure 3:16 Model-predicted surface coverage of different ceria species along the catalyst length with oscillations at $\lambda = 0.990 \pm 0.025$ and a period length of a) 4 s, b) 10 s and c) 14 s at four points in time each.

In Figure 3:16a, the ceria sites at the surface of the catalyst more than 50 mm downstream of inlet ($z > 50\text{ mm}$) were permanently covered by $\text{Ce}_2(\text{CO}_3)_3$ regardless of the time instances. As can be seen in Figure 3:16b, during the 10 s oscillations, the final 1/3 of the catalyst ($z > 67\text{ mm}$) was mostly deactivated, corresponding to the subtle change of concentration between m.p.3 and m.p.4 in Figure 3:4. The spatial illustration enabled by the simulation implies that oscillations of too high frequency was not beneficial for CH_4 conversion, due to largely deactivated ceria sites. The key for optimization of oscillation frequency lied in maximizing the active length of the catalyst. However, very low frequencies resulted in longer lean gas periods with increasing NO_x emissions.

3.4 Conclusions

In this section, pathways of catalytic CH_4 removal for natural gas engines were investigated under different periodic lean/rich oscillations. CH_4 conversion increased significantly with oscillations, reaching even six times higher values in respect to steady state under the same λ_{avg} . During each oscillation, a characteristic CH_4 concentration profile was identified with local maxima at both the lean to rich and rich to lean transitions, followed by local minima during each lean and rich phase. The CH_4 concentration time histories were characterized by a typical 'W' shape during each lean/rich oscillation. This 'W' shape profile was observed for various oscillations and operating conditions. Notably, the CO conversion was also enhanced during the oscillations. The maximum concentrations of CH_4

and CO were half a period out of phase, evidencing different reaction pathways. While direct oxidation by oxygen was the dominant conversion pathway for CO, CH₄ was mostly reduced by steam reforming (SR).

Four reaction regimes were identified in the 'W' shaped CH₄ concentration profile.

Following the lean to rich transition,

- SR was activated, associated with the reduction of Ce⁴⁺ to Ce³⁺, followed by
- SR deactivation due to competition with CO oxidation and carbonate formation on the catalyst surface.

Following the rich to lean transition,

- CO is immediately oxidized by oxygen resulting in SR enhancement, followed by a
- lean oxidation/regeneration phase dominated by CH₄ direct oxidation.

Each of these reaction regimes was linked to different chemical processes that affected the active sites and reaction rates, which in turn shaped the CH₄ concentration profile in this characteristic 'W' shape. SR, however, resulted in enhanced H₂ generation and consequently also increased NH₃ emissions. On the other hand, NO_x emissions remained low as long as the λ_{avg} stays below 1.0.

The oscillations were varied in terms of λ_{avg} and period length. For achieving enhanced CH₄ conversion compared to steady state, the λ_{avg} must be sufficiently high to allow regeneration of the active sites during the lean phases. The THC outlet concentration profile was shifted to higher values with increasing oscillation frequency until a maximum value determined by the time needed to completely deplete and replenish the OSC. However, a too long lean/rich duration leads to on average low THC conversion due to the low reaction rate of CH₄ direct oxidation by oxygen during lean phases.

A simulation model was developed to support the interpretation of the oscillation related phenomena, which was validated against the experiments under steady state and transient periodic oscillating conditions. The characteristic THC concentration profiles and important results of the experiments under oscillating conditions were successfully reproduced. The simulation allowed interpretations of the chemical processes on the catalyst surface along the catalyst axis. Results have shown that high CH₄ conversion was achieved by minimizing the length of completely deactivated section fully covered with Ce₂(CO₃)₃, which were associated with deactivated SR.

Chapter 4 Roles of different noble metals

Parts of this chapter are published in: M. Wang, P. Dimopoulos Eggenschwiler, T. Franken, M. Agote-Arán, D. Ferri, O. Kröcher, Investigation on the Role of Pd, Pt, Rh in Methane Abatement for Heavy Duty Applications, Catalysts. 12 (2022) 373. <https://doi.org/10.3390/catal12040373>.

In previous chapters, methane abatement pathways have been investigated in Pd/Rh catalysts under steady and transient conditions. This chapter takes a closer look at methane oxidation and ammonia formation characteristics under the catalytic influence of different Platinum-group metals (Pt, Pd and Rh). To our knowledge so far, this has not been a subject of systematic studies up to now. Catalysts of different compositions were analyzed under various temperatures using targeted quasi-steady and transient procedures. Based on the identified characteristics of different Platinum-group metals, an improved catalyst composition was proposed, manufactured and tested under optimized λ oscillation strategies during a world harmonized steady cycle (WHSC) test, in order to highlight the findings of the present work in the emissions of the entire engine parameter map. The knowledge gained in this study provides important guidance for development of catalyst compositions in future methane aftertreatment systems.

4.1 Experimental

4.1.1 Catalysts

Catalysts used in this study were commercial honeycomb catalysts containing different combinations of Platinum-group metals supported on alumina and ceria zirconia: Pd-only (62 g/ft³), Pt/Rh (44/4.5 g/ft³), Pd/Rh (64.4/4.6 g/ft³), and Pt/Pd/Rh (22/32.2/4.5 g/ft³). All catalysts were washcoated on ceramic monolith substrates (400 cpsi). The diameter of the substrate was 105 mm. The monolith lengths were either 50 mm or 100 mm, depending on the setup. The cross sections of the catalysts were studied with SEM (Hitachi TM3030Plus).

4.1.2 Measurements on the engine test bench

The catalysts were mounted downstream of the turbocharger without first stage catalysts, similar to the setup in Chapter 3. Measurement equipments and test bench setups were the same as described in Chapter 2. Three measurement procedures were designed for the investigations: λ ramp, cold start and λ oscillations.

The measurement procedure for λ ramps started with a pre-conditioning period of 10 min, in which the engine ran at steady state at $\lambda = 0.9$ for 10 min. This guarantees that the λ ramp starts with known catalyst state and fully depleted oxygen storage capacity (OSC). After preconditioning, the λ value of the exhaust gas increased linearly from 0.9 until 1.1 in 15 min, while keeping the engine speed and torque steady. Upon reaching $\lambda = 1.1$, the λ value started decreasing linearly toward 0.9 and reached 0.9 in 15 min. The transient concentration profiles were recorded during the λ -sweeps.

Cold starts were performed after the test bench was cooled overnight. During cold starts, the engine operation point was kept at 1600 rpm, 50 Nm and the λ sensor signal stayed at 1.00. The transient concentration profiles were recorded until 30 minutes after the start of fuel injection.

During λ oscillations, λ sensor signal made step changes between $\lambda_c \pm 0.025$ (λ_c is the pre-determined λ center). The duration of lean/rich periods were kept the same. The lean/rich duration varied from less than 3 s to 60 s, according to measurement needs. Before performing each λ oscillations measurement, the catalyst was pre-conditioned at $\lambda = 0.90$ for 10 min. After the start of λ oscillations, the concentration profiles were monitored until reaching stabilization. All analyses were based on stabilized concentration profiles.

4.1.3 Measurements on the model gas reactor

A cylinder piece (1.39 cm² entrance area, 4.83 cm length) was extracted from the Pd/Rh monolith mentioned in engine test bench tests. The model gas reactor described in Chapter 2 was used for testing the piece. The catalyst was analyzed under a slightly rich gas mixture (1500 ppm CH₄; 9000 ppm CO; 2750 ppm NO; 5000 ppm H₂; 7600 ppm O₂; 50000 ppm H₂O, bal. N₂) in temperature sweep experiments (100 °C → 400 °C; 5 °C/min). The calculated λ value was 0.995. The flow rates of gases were adjusted to obtain a gas hour space velocity (GHSV) of 75 000 h⁻¹.

4.2 Results and Discussions

4.2.1 SEM washcoat characterization

Figure 4:1 shows the SEM image of the Pd/Rh catalyst, in which the substrate and washcoat can be clearly distinguished. The SEM analysis revealed that the washcoat thickness in the channel corners was significantly higher than in the central parts. In the corner of the cells the washcoat accumulated up to a thickness of 250 μm ; in contrast, the layer thickness in the center of the substrate walls was below 80 μm . All investigated cells showed comparable washcoat distribution and morphology.

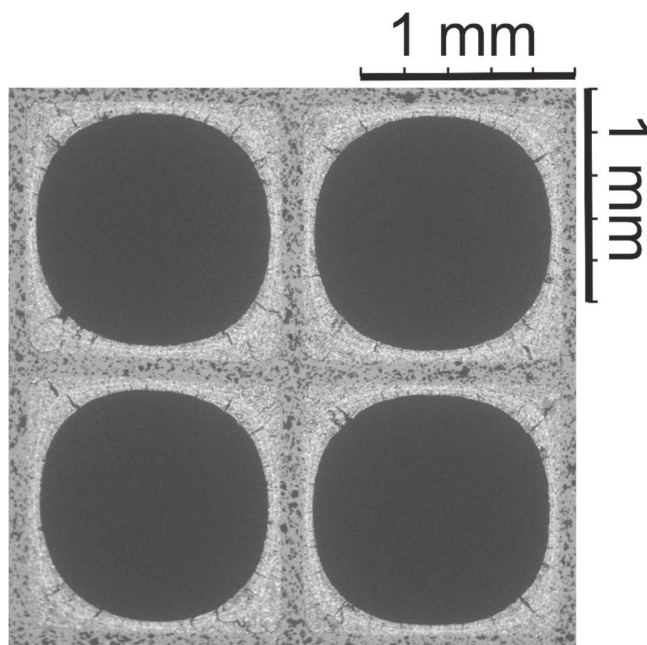


Figure 4:1 SEM image ($\times 30$) of the Pd/Rh catalyst.

4.2.2 λ ramp in the mid temperature range

Figure 4:2 shows CH_4 conversions obtained during λ ramp-up and ramp-down for Pd/Rh (Figure 4:2a) and Pt/Rh (Figure 4:2b) catalyst (50 mm length). The engine operates at a speed of 1600 rpm and 210 Nm torque. The catalyst inlet temperature was approximately 520 $^{\circ}\text{C}$, which varied by ± 10 $^{\circ}\text{C}$ according to the λ values. The gas hourly space velocity (GHSV) is of ca. 256000 h^{-1} . During λ ramp-up in Pd/Rh catalyst (blue line in Figure 4:2a), CH_4 conversion stayed 0 until λ was slightly larger than 1.0. This demonstrates that both conversion pathways of CH_4 (direct oxidation by oxygen and SR) were inactive. Direct oxidation was restricted by the lack of oxygen under rich conditions, while SR was likely inhibited by surface carbonaceous species [118]. At λ slightly larger than 1.0, a sharp increase of CH_4 conversion was observed. Similar observations have been made in Chapter 2 during a quasi-steady state λ -sweep on the same Pd/Rh catalyst. The sharp rise in conversion was proved to be linked to the oxygen excess remaining after oxidizing other active reducing agents, e.g. CO and H_2 . Until this point in time, palladium was probably in the metallic phase and its surface was not yet fully covered by oxygen molecules. The sharp rise in CH_4 conversion lasted briefly and was followed by a sharp decrease in CH_4 conversion. This could be explained by oxygen inhibition, i.e. oxygen molecules cover the active sites and hinder CH_4 adsorption [47,55]. With increasing λ value, Pd was slowly oxidized to PdO due to the excess oxygen in lean feed. Between 500 $^{\circ}\text{C}$ and 600 $^{\circ}\text{C}$, Pd oxidation is possible however slow [40,126]. It is generally agreed that the combination of metallic Pd(0) and PdO is the most active palladium state for lean CH_4 oxidation [41–43]. Therefore in our λ ramp-up, on the lean side, the CH_4 conversion first increased to a maximum of around 0.27, probably corresponding to the existence of a mixed Pd/PdO phase, and then decreased slowly to around 0.13 at $\lambda = 1.1$ when Pd is likely completely oxidized to PdO.

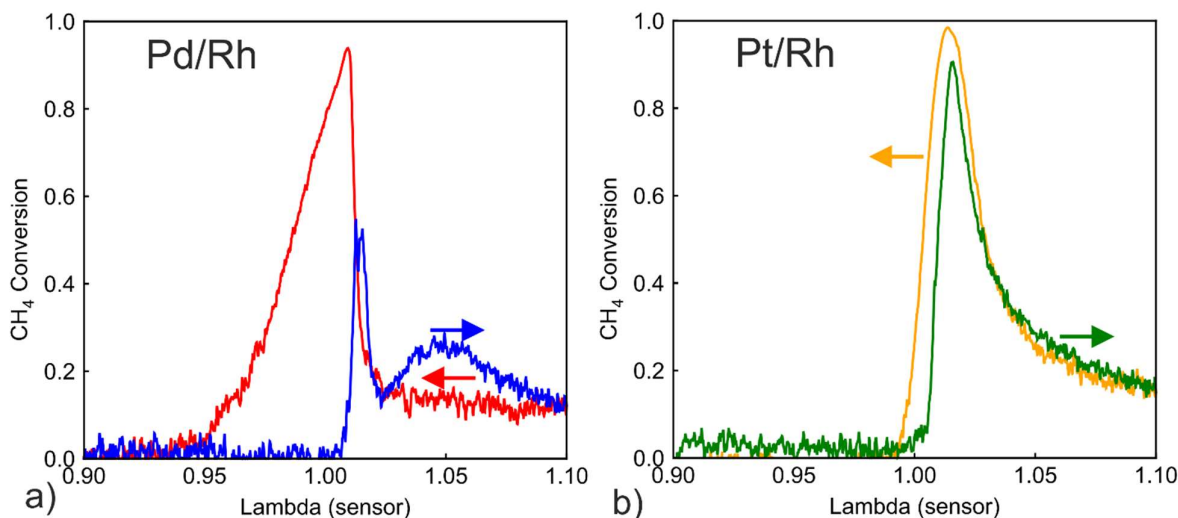


Figure 4:2 CH₄ conversion of the a) Pd/Rh b) Pt/Rh catalyst during λ ramp-up (15 min) and ramp-down (15 min) at 520 °C (GHSV = 256000 h⁻¹).

During λ ramp-down, CH₄ conversion showed clear hysteresis in the lean phase compared to ramp-up, and stayed steady at around 0.13 conversion. The hysteresis demonstrated different palladium oxidation states between ramp-up and ramp-down. While ramping down, palladium stays fully oxidized in PdO state. Several previous studies have shown that the oxidation of CH₄ is a zero order reaction toward oxygen concentration [46,47], which is in line with the steady lean CH₄ conversion during ramp-down. At λ sensor slightly higher than 1.00, CH₄ conversion rose sharply to more than 0.9. The CH₄ conversion during ramp-down was significantly higher, compared to zero CH₄ conversion between $0.95 < \lambda < 1.00$ during ramp-up. The high CH₄ conversion at around $\lambda = 1.00$ only decreased slowly in the rich phase, and reached zero conversion at $\lambda < 0.95$. The same, strong enhancement of CH₄ conversion was studied in detail in Chapter 2. Activation of SR reaction pathway was proved to be the cause. SR reaction, however, only lasts a short period of time, until all active ceria sites were blocked by surface carbonaceous species (mostly carbonates). The carbonate blocked ceria sites could be regenerated during lean conditions, which explained the activation of SR only after shifting from lean to rich conditions. The H₂O content varied only slightly, from 17.3 vol% (minimum at $\lambda = 1.1$) to 19.0 vol% (maximum at $\lambda = 1.0$), when λ value changed from 0.9 to 1.1. It was safe to neglect the influence of H₂O variation.

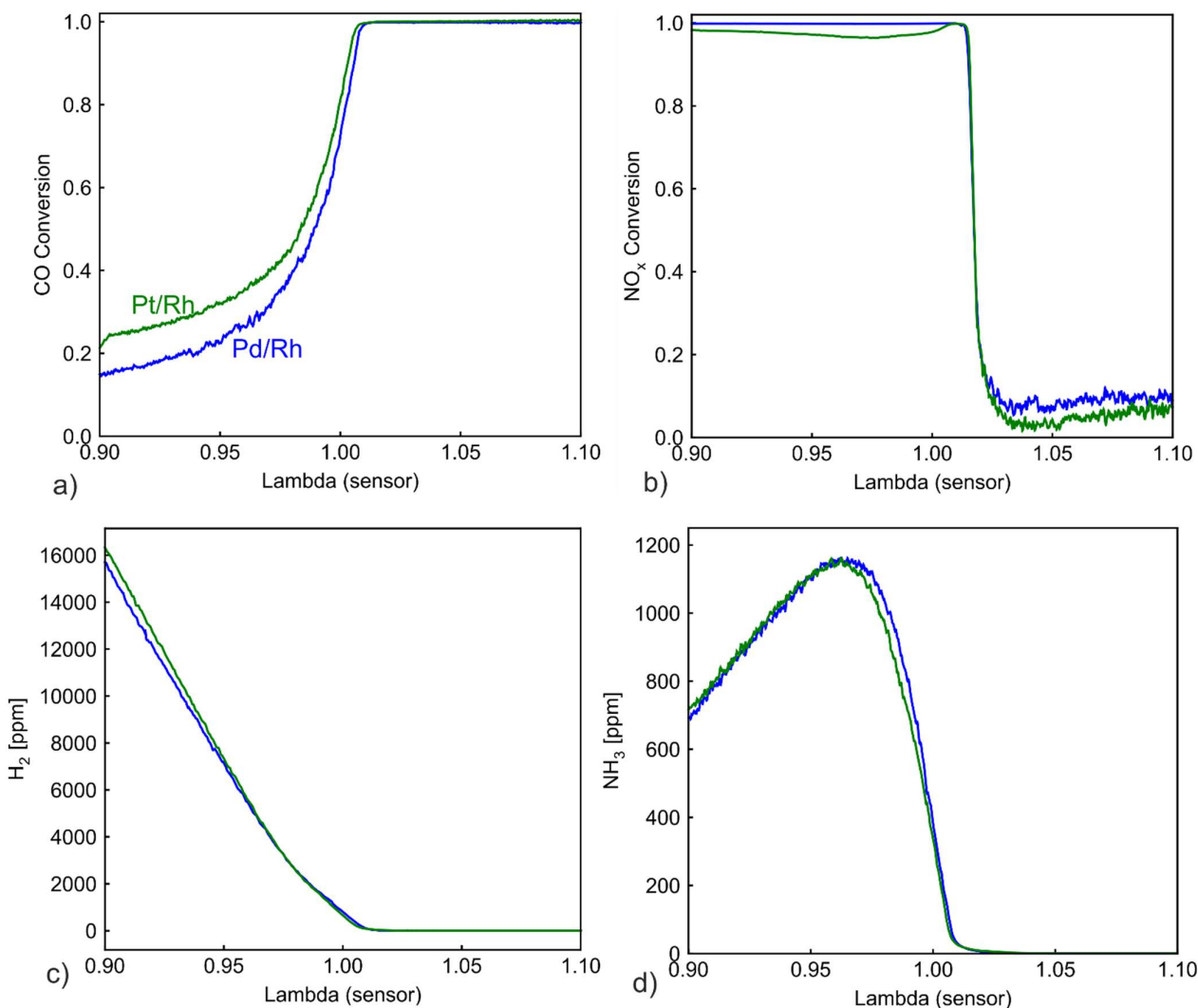


Figure 4:3 Comparison of a) CO conversion b) NO_x conversion in the Pt/Rh and the Pd/Rh catalyst and c) H₂ concentration and d) NH₃ concentration downstream the catalysts during λ ramp-up at 520 °C.

During λ ramp-up with the Pt/Rh catalyst (Figure 4:2b green line), similar to Pd/Rh, no CH₄ conversion occurred until the sharp onset of conversion due to sufficient O₂ at λ slightly higher than 1.00. The lean CH₄ conversion profiles of the Pt/Rh catalyst were less complicated than the profiles of Pd/Rh. CH₄ conversion decreased steadily until $\lambda = 1.1$. The CH₄ conversion in the vicinity of $\lambda = 1.00$ was much higher than that of Pd/Rh. The active state of platinum for CH₄ oxidation is metallic Pt [33]. Due to instability of PtO_x above 300 °C, platinum is expected to stay in metallic state during the experiment [127]. Even though oxygen inhibition affected also the Pt/Rh catalyst, Pt was in its active form after the rich/lean transition and converted CH₄ more efficiently than Pd/Rh at near stoichiometric lean regions. During ramp-down, no hysteresis was observed on the lean side, most probably due to the fact that Pt stayed in the same metallic form. On the rich side ($\lambda < 1.0$), the CH₄ conversion was near zero in the Pt/Rh catalyst for both ramp-up and ramp-down, signaling either low activity toward SR or very fast deactivation of SR.

Conversion of CO and NO_x, as well as outlet concentration profiles of H₂ and NH₃ during ramp-up are plotted in Figure 4:3. Unsurprisingly, in both catalysts, CO (Figure 4:3a) was 100% converted under lean conditions, while the conversion was low at $\lambda < 1.0$. In Chapter 2, CO was proved to undergo mainly the water gas shift (WGS) reaction under very rich conditions. Pt/Rh exhibited higher activity in WGS, despite having less precious metal loading (48.5 g/ft³) compared to the Pd/Rh catalyst (70 g/ft³). The NO_x conversion profile for both catalysts were very similar, with almost 100% conversion on the rich side and low conversion in the lean side. H₂ in the exhaust gas were first oxidized by O₂/NO_x when either was available. In the downstream part of the as, H₂ was formed through

WGS reaction [118]. Due to slightly better WGS behavior of Pt/Rh, the outlet H_2 concentration was also slightly higher. NH_3 was not detected in the engine-out exhaust and was produced in the catalysts via NO_x reduction [77,79]. The NH_3 production profile (Figure 4:3d) was almost the same for Pt/Rh and Pd/Rh catalysts.

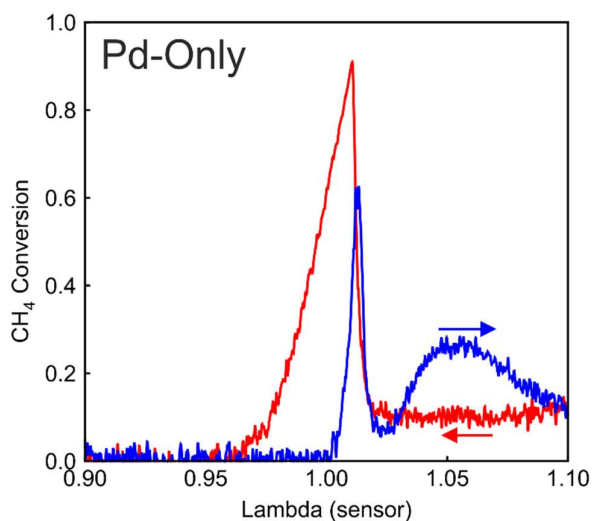


Figure 4:4 CH_4 conversion during λ ramp-up and λ ramp-down in the Pd-only catalyst.

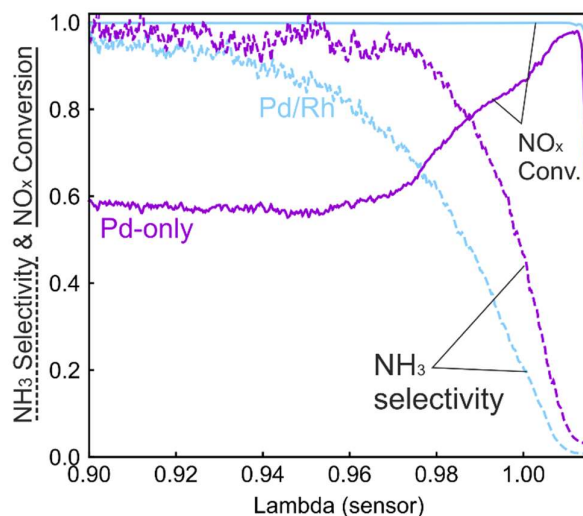


Figure 4:5 Comparison of NO_x conversion and NH_3 selectivity during λ ramp-up in the Pd-only and Pd/Rh catalyst.

To better understand the role of Rh in Pd/Rh, the same λ ramp was performed on a Pd-only catalyst. In Figure 4:4, CH_4 conversion profiles demonstrate almost identical characteristics as for Pd/Rh catalyst (Figure 4:2a). During ramp-up, as iws an initial conversion peak at around 1.00, followed by the lowest conversion shortly after the peak. With increasing oxygen in the feed, the CH_4 conversion rised slowly, reaching a maximum value briefly, and subsequently decreased to a steady value. This is additional evidence that the characteristic behavior of CH_4 conversion on the lean side is attributed to palladium oxidation states, while presence of Rh has no significant effect.

Figure 4:5 shows a comparison of NO_x conversion and NH_3 selectivity between the Pd/Rh and Pd-only catalyst. The Pd-only catalyst exhibited NO_x conversion lower than 60% at $\lambda < 0.96$, whereas the NO_x was nearly completely converted with the Pd/Rh catalyst. At very rich conditions ($\lambda < 0.93$), NH_3 selectivity was nearly 100% for both catalysts. As λ increased toward 1.00, NH_3 selectivity of Pd/Rh

catalyst decreased much faster than in the Pd-only catalyst. NH_3 selectivity of the Pd/Rh catalyst was significantly lower in regions within 3% of stoichiometry, which is the relevant range for real-life operating conditions. The results are in line with the notion that Rh is the most active platinum-group metal for selective NO_x reduction to N_2 [80,81,128]. In view of strictly regulated NO_x and NH_3 emissions in engine exhausts, Rh is an important component along side Pd and/or Pt.

4.2.3 λ ramp at low and high temperature

The λ ramp procedure was repeated at different engine loads, for analyzing the temperature effect. In Figure 4:6a, the engine operated at high load (2800 rpm; 220 Nm), with a catalyst inlet temperature of ca. 630°C and a GHSV of approximately 546 000 h^{-1} . In Figure 4:6a (high temperature), during λ ramp-up of the Pd/Rh catalyst (blue curve), the CH_4 conversion decreases monotonously after the initial conversion peak at λ slightly higher than 1.00, in contrast to the fluctuating lean conversion in Figure 4:2a. There is also no lean conversion hysteresis. This phenomenon could be attributed to the instability of PdO at high temperatures. The oxidation from Pd to PdO only occurred below 600°C [38]. The catalyst temperature in Figure 4:6a lied at 630°C or higher, therefore palladium stayed in the form of metallic Pd(0), even under lean conditions. The CH_4 conversion of the Pd/Rh catalyst at $\lambda = 1.1$ in Figure 4:6a was almost the same as that in Figure 4:2a, even though the temperature was much higher. This is another evidence of Pd staying in metallic state, as Pd(0) is demonstrated to be less active in CH_4 oxidation than PdO [126]. In comparison, at high temperatures (Figure 4:6a), Pt/Rh catalyst exhibited higher CH_4 conversion than in Figure 4:2a. This is rather unsurprising, as metallic Pt was the active site for both temperatures. The SR hysteresis under rich conditions was again observed with the Pd/Rh catalyst, but only in a narrower λ range. SR deactivated faster at higher engine loads due to higher GHSV and temperature, which corresponded to results from Chapter 2.

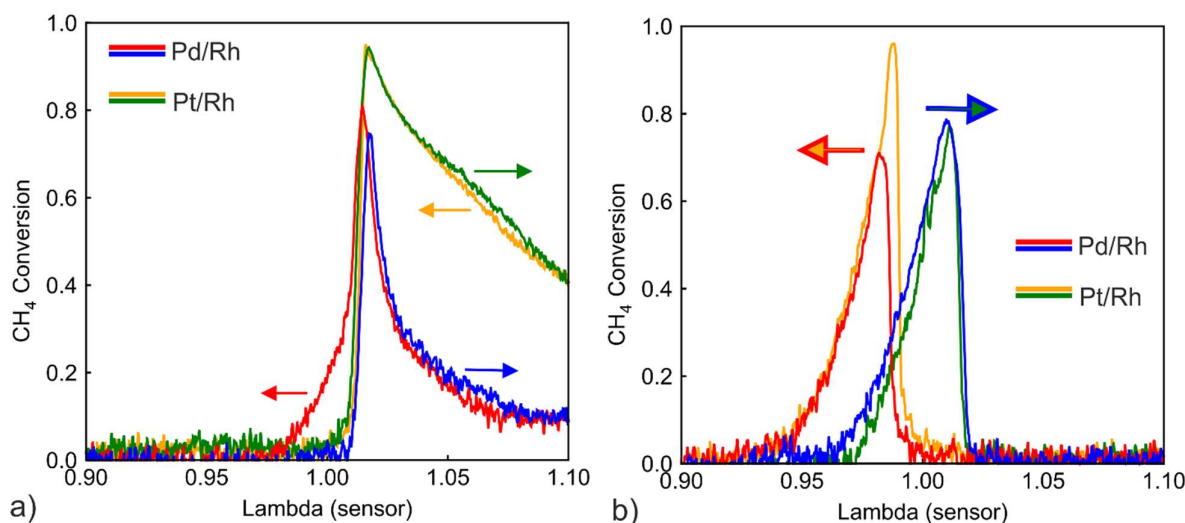


Figure 4:6 CH_4 conversion during λ ramp-up and λ ramp-down in the Pd/Rh and Pt/Rh catalyst, at temperature a) 630 °C (GHSV = 546 000 h^{-1}), and b) 360 °C (GHSV = 83 000 h^{-1}).

Figure 4:6b shows the CH_4 conversion during λ ramp under low load conditions (1600 rpm 50 Nm) at an inlet temperature of ca. 360 °C and a GHSV of ca. 83 000 h^{-1} . Under lean conditions, CH_4 was not converted at all for Pd/Rh and Pt/Rh catalysts, which signals that the temperature was too low for direct oxidation with oxygen. At near stoichiometry and under rich conditions, a strong conversion peak (over 65%) was observed for both ramp directions and catalysts. The Pt/Rh catalyst displayed higher conversion during ramp-down. As the temperature was too low for direct oxidation, these conversion peaks were based on the SR reaction. In contrast to higher temperatures, SR was activated during λ ramp-up. This implies that the proposed deactivation mechanism through carbonaceous formation cannot completely block SR at low temperatures. The exact mechanism requires further studies. In Figure 4:6b, there is a hysteresis of conversion profiles in the form of displacement between ramp-up and ramp-down. The displacement at the right edge of the conversion can be easily attributed to OSC. However, the conversion discrepancy lasted even after OSC was fully depleted ($\lambda < 0.97$). Figure 4:7 plots CO concentration together with methane conversion for both the Pd/Rh (Figure 4:7a) and the Pt/Rh (Figure 4:7b) catalyst. CO concentration (dotted lines) exhibits a long-lasting hysteresis throughout the entire rich side. The hysteresis can be explained with the difference in WGS reaction rate, caused by the accumulated amount of slow forming surface carbonate species [64,66,67]. The hysteresis of CH_4 conversion is linked to the outlet CO concentration. This is demonstrated in Figure

4:7, where two characteristic CH₄ conversions (0.1 and 0.2) are selected, and the corresponding CO concentrations are indicated. With the Pd/Rh catalyst (Figure 4:7a), at 0.1 CH₄ conversion, the corresponding CO concentration was about 500 ppm for both ramp-up and ramp-down. The same applies to 0.2 CH₄ conversion: CO concentration was about 350 ppm for both ramp-up and ramp-down. Also in Figure 4:7b (Pt/Rh catalyst), the characteristic CH₄ conversion (0.1 or 0.2) corresponds to the same CO concentration for ramp-up and ramp-down (within the same catalyst). This suggests that the low temperature CH₄ conversion was linked to the CO concentration, which had a strong inhibition effect on SR [57,129]. At mid to high temperatures (Figures 4:2 and 4:6a), due to full deactivation of SR during ramp-up, the effect of CO inhibition was not observed.

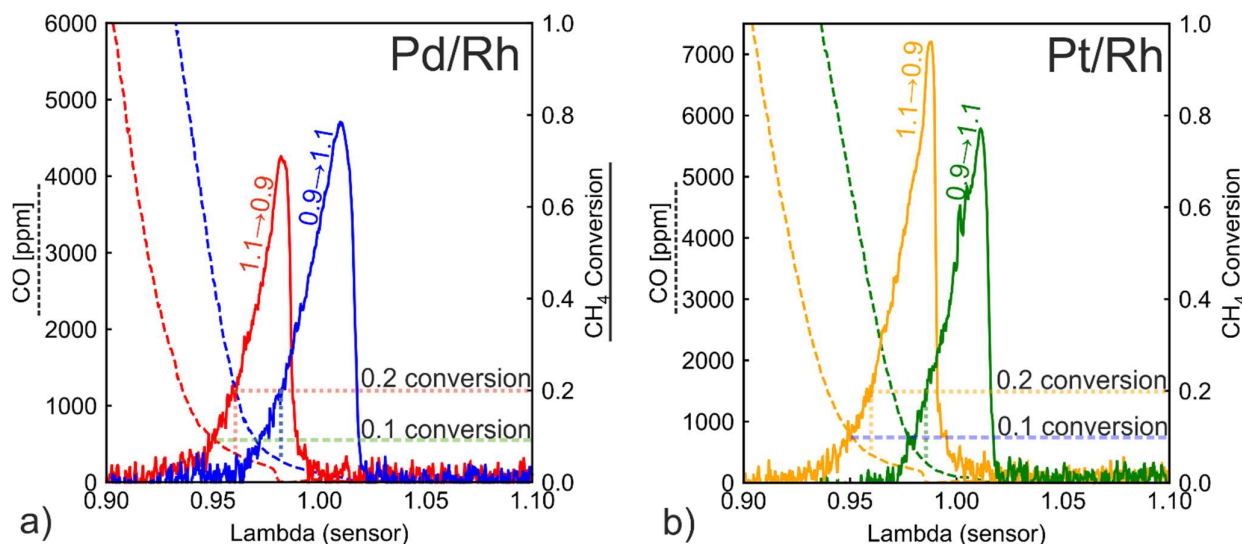


Figure 4:7 CO concentration and CH₄ conversion during λ ramp-up and λ ramp-down in a) the Pd/Rh and b) the Pt/Rh catalyst at temperature 360 °C.

4.2.4 Analysis of low temperature behavior based on cold start and temperature ramps

In model gas reactors, temperature programmed techniques are frequently used to analyze reaction mechanisms. Engine test benches are less flexible in changing only one operating parameter, because temperature, GHSV and engine out emissions are all interconnected. Cold start tests provide a unique opportunity where temperature increases continuously with stable engine out emissions. In Figure 4:8, evolution of outlet temperature and species concentrations are plotted against inlet temperature during cold start. In the top plot of Figure 4:8, the outlet temperatures of the Pd/Rh and the Pt/Rh catalysts (blue and green line respectively) are depicted together with the inlet temperature (black linear line). At the beginning of the cold start process (inlet temperature < 130°C), no chemical reactions could take place. Heat was transferred from the hot exhaust gas to the cold catalyst and the catalyst canning. The inlet temperature was higher than the outlet temperature. As the inlet temperature rises, exothermic reactions e.g. H₂ and CO oxidation started to occur, which resulted in higher outlet temperatures than the inlet (>175°C). Detailed investigations and analysis of heat transfer phenomena during cold starts can be found in [130]. For the Pd/Rh catalyst (blue line), NO_x conversion started at around 130°C. At the same time, H₂ consumption and N₂O production were observed. As CO was not unconverted at this temperature, the observed NO_x was solely reduced by H₂ leading to N₂O formation. N₂O is often observed as intermediate product of NO_x reduction, and can be re-adsorbed and further reduced to either N₂ or NH₃ [74,131]. At ca. 150°C, NH₃ started to appear and its concentration reached a maximum value at ca. 165°C before decreasing to zero at ca. 200°C. The decrease in NH₃ could be attributed to two effects: the complete consumption of H₂ by O₂ (H₂ concentration plot), and the oxidation of NH₃ by O₂. Results in a later chapter (Chapter 5) on the same Pd/Rh catalyst suggest that the oxidation of NH₃ started above 150 °C and below 200 °C [132]. CO started to be consumed at approximately 160°C, much later than the start of the consumption of NO_x, O₂, and H₂.

In the Pt/Rh catalyst, the start of conversion for NO_x, CO and H₂ occurred at approximately 50°C higher temperature, in comparison to the Pd/Rh catalyst. The different platinum-group metal loadings of the two catalysts made it difficult to compare their oxidation activity. With the Pt/Rh catalyst, NO_x consumption occurred at a similar temperature as CO, and much later than the start of O₂ consumption. N₂O also appeared at a much higher temperature (80°C) than in the Pt/Rh catalyst. First principle calculation has shown that N₂O binds more strongly to Pt than Pd and desorption is more difficult with Pt [74]. THC conversion started at around 290 °C in the Pt/Rh catalyst, around 30°C lower than the Pd/Rh catalyst. The start of conversion of total hydrocarbons (THC, more than 90%

methane) accompanied immediate formation of NH_3 and H_2 , suggesting that THC were consumed by SR, rather than by oxidation with oxygen. The results agree with the above conclusions indicating that the only reaction pathway for CH_4 is SR during λ ramps at 360°C . In view of the fact that Pt/Rh catalyst had lower metal loading but lower SR initiation temperature, it is safe to conclude that Pt has better SR activity at low temperatures than Pd.

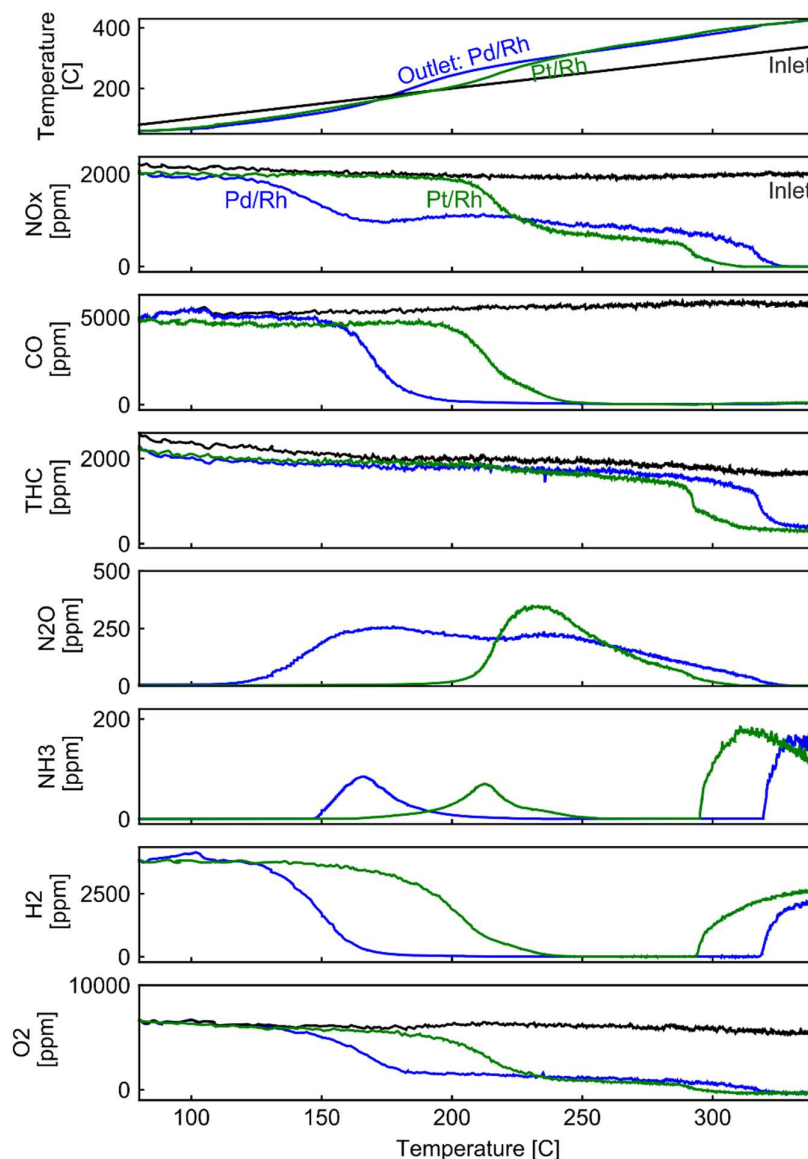


Figure 4:8 Comparison of temperature and concentration profiles upstream and downstream the Pd/Rh and Pt/Rh catalysts during cold start experiment.

The Pd/Rh catalyst was further studied in the model gas reactor with a controlled temperature ramp ($5^\circ\text{C}/\text{min}$). In Figure 4:9, the results of concentrations and conversion of major pollutants are shown. Similar to the Pd/Rh catalyst during cold start, N_2O was the first product observed at low temperature, before N_2 and NH_3 was formed. This confirms that N_2O was an intermediate product of NO_x reduction. At low temperature ($< 200^\circ\text{C}$), NH_3 concentration peaked at around 168°C and decreased quickly to zero with rising temperature, in agreement with the results obtained on the engine test bench. At 168°C , the sudden decrease in NH_3 concentration was accompanied by a simultaneous increase in N_2O , hinting that NH_3 was oxidized into N_2O . Starting from 325°C (similar temperature range as in engine test bench), NH_3 concentration increased again, accompanied by a simultaneously decrease of H_2 conversion, which was linked to the H_2 production from the increasing SR reaction rate. The 50% conversion of CO and H_2 occurred at 156°C and

170°C, respectively (150 °C and 170 °C for Pd/Rh in engine test bench). The consistency of observations in lab-scale reactors and engine test bench demonstrated the reliability and significance of cold start tests in engine, which can provide valuable implications on reaction pathways.

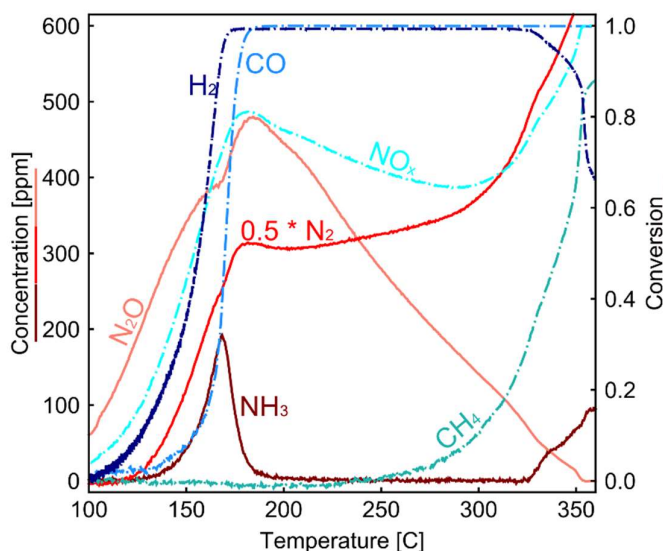


Figure 4:9 Temperature and concentration profiles during temperature programmed reaction in model gas reactor.

4.2.5 Slow λ oscillation

The above λ ramp experiments revealed the conversion characteristics in a wide range of λ , but it was limited in the analysis of transient operations, due to the slow and continuous λ change. Transient conversion characteristics were better captured during slow λ oscillations, in which both the lean and rich phase last 60 s. Species concentration during one λ oscillation at different temperatures are shown in Figure 4:10. The operating points of the engine corresponded exactly to the low, mid and high load points in the previous λ ramp experiments. The almost identical O_2 concentration profiles in the λ transitions (O_2 concentration plots in Figure 4:10) indicate that both catalysts possessed similar OSC. At low temperature (Figure 4:10a), after transition to rich conditions, the THC concentration in both catalysts passed through a low value before stabilizing at ca. 1000 ppm, corresponding to a conversion of 0.4. The THC conversion change of Figure 4:10a can be imagined to correspond to a fast transition along the ramp-down curve in Figure 4:6b. The conversion remained high as long as OSC was not depleted. The temporary conversion enhancement was stronger in the Pt/Rh catalyst, corresponding to the higher conversion peak in Figure 4:6b (yellow line). Due to stronger conversion, the OSC depleted faster in the Pt/Rh catalyst, as more reducing agent was needed to oxidize CO and H_2 formed from SR. The fast depletion of OSC affected also the NH_3 formation. NH_3 was observed earlier in the Pt/Rh catalyst. After the transition to lean phase at $t = 60$ s, another temporary low THC concentration is observed. Similar to the previous analyses of the rich transition, this signaled an SR enhancement related to the favorable λ condition during oxidation of the OSC component. In addition, CO was oxidized by the excess O_2 immediately after changing into the lean feed. This alleviated the competitive adsorption of CO and CH_4 and further enhanced SR in the time range of $60 < t < 75$ s, when SR was occurring. After OSC was fully oxidized, SR is deactivated, as oxygen vacancies were necessary for SR [63,122]. Without SR, THC conversion was very low. The converted part was mainly non-methane hydrocarbons.

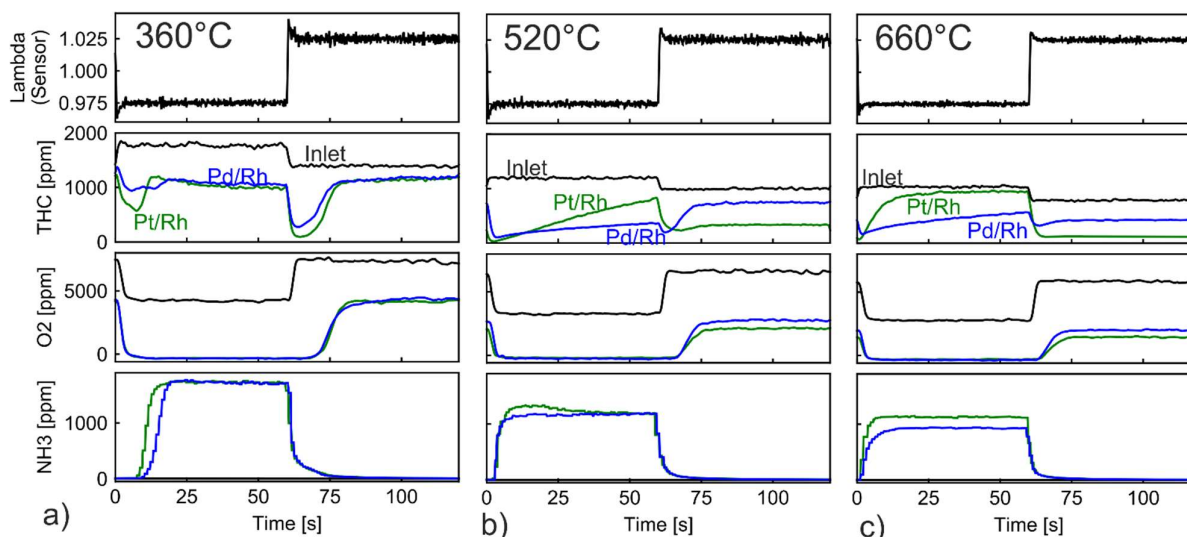


Figure 4:10 THC, O₂ and NH₃ concentration profiles during slow λ oscillations at a) 360 °C, b) 520 °C, and c) 630 °C in Pt/Rh and Pd/Rh catalyst.

At 520 °C (Figure 4:10b), the THC concentration in both catalysts reached minimum after the step change from lean to rich. This increase in conversion was attributed to SR activation in Chapter 2. The SR conversion was stronger in the Pt/Rh catalyst immediately after the step change. The high THC conversion, however, attenuates with time. As discussed above, this is linked to the decrease of SR reaction rate caused by the formation and accumulation of ceria carbonates. The deactivation via carbonates affected only SR reaction, because active ceria sites were involved in the H₂O dissociation step during SR [60,63,98]. The attenuation was much faster in the Pt/Rh catalyst, the conversion drops from 0.98 to less than 0.3 in 60 s. The fast deactivation of SR explains the lack of SR hysteresis in Figure 4:2b for the Pt/Rh catalyst. In line with results from Figure 4:2, the Pt/Rh catalyst oxidized CH₄ at significantly higher conversion than the Pd/Rh catalyst under lean conditions.

The SR activation and deactivation characteristics at 660 °C were very similar to those observed at 520 °C (Figure 4:10c). The Pt/Rh catalyst triggered initially higher SR rate but deactivated much faster than the Pd/Rh catalyst. The Pt/Rh catalyst also produced more NH₃ at 660 °C.

4.2.6 Conversion characteristics of Pt/Pd/Rh catalyst

Of the three metals, the role of Rh was unique and unreplaceable. Rh enhanced NO_x conversion and reduced selectivity toward unwanted NH₃ emissions. Pt and Pd both acted as oxidation catalysts and each has different characteristics at different gas composition and temperature. Pt had clear advantages with rich feed at low temperature. However, SR deactivation was too fast at higher temperatures. Pd sustained SR for a longer time under rich conditions, but in general had lower activity toward methane direct oxidation. The results suggest that the combination of these three metals can possibly integrate advantages and balance weaknesses.

A catalyst consisting of Pt/Pd/Rh (22/32.2/4.5 g/ft³) was prepared and installed in the engine test bench. The catalyst has a length of 100 mm. λ ramp experiment was performed on the Pt/Pd/Rh catalyst at 1600 rpm 210 Nm (520 °C), and the result is shown in Figure 4:11. During ramp-up (blue line), the CH₄ conversion decreased monotonously with λ under lean conditions, similar to Pt/Rh catalyst in Figure 4:2b. During ramp-down, at $\lambda > 1.0$, the CH₄ conversion increased with decreasing λ , which again corresponded to the behavior of Pt. The hysteresis in the range of $1.0 < \lambda < 1.1$ could be traced back to Pd, which existed in different oxidation states during ramp-up and ramp-down. A clear SR hysteresis under rich conditions ($0.95 < \lambda < 1.00$) suggested that the Pt/Pd/Rh catalyst was able to sustain SR for a relative long period of time, similar to the Pd/Rh catalyst in Figure 4:2a. The Pt/Pd/Rh catalyst combined the advantage of the Pt/Rh catalyst at lean conditions and the benefit of the Pd/Rh catalyst under rich conditions.

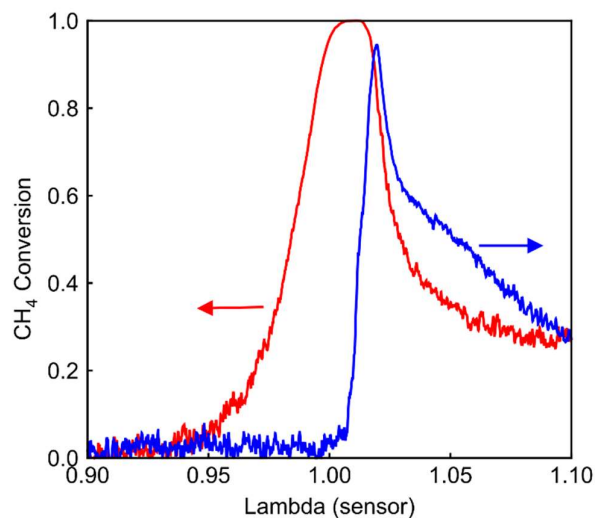


Figure 4:11 CH₄ conversion of the Pt/Pd/Rh catalyst during λ ramp-up and ramp-down at 520 °C.

4.2.7 Optimization of λ oscillation in Pt/Pd/Rh catalyst

λ oscillations have been recognized to promote a significant enhancement of CH₄ conversion [42,50,97]. This was attributed to high SR reaction rate (discussed in Chapter 3), which was enabled by the periodic catalyst regeneration from carbonaceous species. The potential of the Pt/Pd/Rh catalyst, which as demonstrated integrates the strength of both Pt and Pd, can be best demonstrated using λ oscillations. Figure 4:12 plots THC, NO_x and NH₃ concentration profiles during oscillations of different period lengths (8, 20 and 26.6 s). The oscillation center (λ_c) was set at λ sensor signal 1.0, which was a pragmatic reference for real life applications. The actual λ (λ_{corr}) at sensor signal 1.0 was identified as 0.990 in a preliminary study. For better comparison, the oscillation period was normalized to 1.0. The concentration profiles are shown in one oscillation starting with the rich phase ($0 < t_{norm} < 0.5$), followed by the lean phase ($0.5 < t_{norm} < 1.0$). For all three period lengths, the concentration profiles were similar. The highest concentration appeared at $t_{norm} = 1.0$, while a local maximum could be observed at $t_{norm} = 0.5$. The 8 s oscillation had the highest THC average concentration (247 ppm, 77.3% conversion), while the 26.6 s oscillation had the lowest THC concentration (26 ppm, 97.6% conversion). At 26.6 s period length, the NO_x concentration rose slightly at $t_{norm} = 1.0$, signaling that the OSC was almost completely filled. Further prolongation of period length led to higher NO_x peaks, which was highly undesirable in sight of strict NO_x emissions regulations. The 26.6 s period length, which almost fully oxidized OSC, was therefore the optimal setting for THC conversion. These results were consistent with results in Chapter 3. The THC concentration profiles were shaped by 4 reaction stages including: activation of SR, subsequent gradual deactivation of SR in rich phase, enhancement of SR and subsequent take-over of oxidation in lean phase. With a longer oscillation period, oxygen penetrated deeper into the catalyst and a larger part of the catalyst underwent regeneration, which resulted in a higher SR rate. The average NH₃ concentration was respectively 377, 363, 357 ppm for the three period lengths. The change of oscillation period length did not significantly change the amount of NH₃ formation.

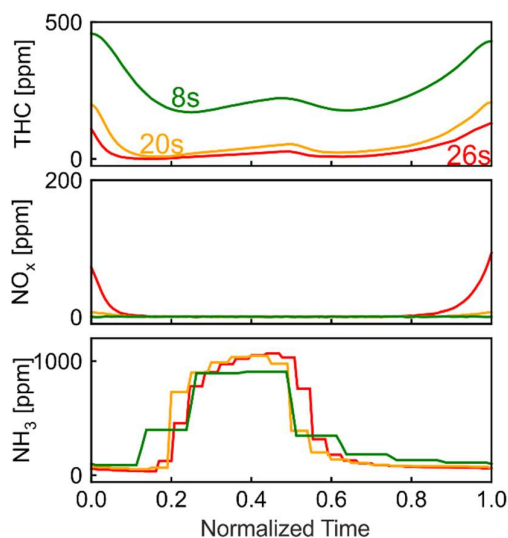


Figure 4:12 THC, NO_x and NH₃ concentration profiles during oscillations with period length of 8 s, 20 s and 26 s.

As discussed before, the inaccuracy of the λ sensor led to 1% deviation to the rich side from stoichiometry. To study the potential of Pt/Pd/Rh catalyst, oscillations with λ_c at 0.5% and 0.2% deviation from stoichiometry were tested, representing an increased accuracy of the λ sensor. Figure 4:13 showed species concentration during oscillations of different center λ_c . The corrected λ (λ_{corr}) equaled 0.990 0.995 and 0.998, for the 1%, 0.5%, 0.2% assumption of λ sensor deviations respectively. The oscillation with $\lambda_c = 0.990$ ($\lambda_{sensor} = 1.0$), 13.3 period length was already shown in Figure 4:13, and is plotted here again for better comparison. The oscillation period lengths were adjusted for the oscillations with $\lambda_c = 0.995$ (10 s period length) and $\lambda_c = 0.998$ (8.7 s period length), in order to keep the OSC from full oxidation. The NO_x concentration in Figure 4:13c slightly increased to around 404 ppm at $t_{norm} = 1.0$ with $\lambda_c = 0.995$. However, the average NO_x concentration stayed low (46 ppm). At $\lambda_c = 0.995$ and 0.998, the O₂ concentration hardly rised from zero (Figure 4:13d), implying that the OSC was nearly but not completely filled. Based on previous discussions, these period lengths were optimal for THC conversion. The average THC concentrations for $\lambda_c = 0.995$ and 0.998 were 28 ppm and 29 ppm, respectively, thus similar to the case of $\lambda_c = 0.990$. The low NH₃ emissions were the main advantage of having λ_c closer to 1.00. The average NH₃ concentrations for $\lambda_c = 0.990$, 0.995, 0.998 were 357, 203, 129 ppm, respectively. At $\lambda_c = 0.998$, NH₃ was observed later under rich conditions and its maximal concentration was lower. Two processes affected the outlet NH₃ concentration profile: NH₃ formation and NH₃ oxidation. NH₃ was formed either through direct reduction of NO_x by H₂ or through combined NO_x reduction of CO and H₂ [77,79]. The NH₃ formation was therefore only possible with the presence of NO_x under rich phase. Under the same catalyst dimension, similar GHSV and temperature, in Chapter 2 it was demonstrated that NO_x was fully reduced in the first half of the catalyst under rich conditions. Thus, NH₃ formation occurred only in the upstream part of the catalyst (under rich conditions), where NO_x was still available. Directly after shifting to rich conditions, the OSC component was almost completely in oxidized state. While NH₃ was formed in the first half of the catalyst, the remaining OSC in the second half of the catalyst oxidized the formed NH₃. Therefore, there was a delay for the rise of NH₃ concentration at the outlet after shifting to rich conditions. The gradual increase of NH₃ concentration signaled the slow depletion of OSC. With $\lambda_c = 0.998$, the OSC was depleted more slowly due to the higher λ value, resulting to late NH₃ observation and therefore less NH₃ emissions.

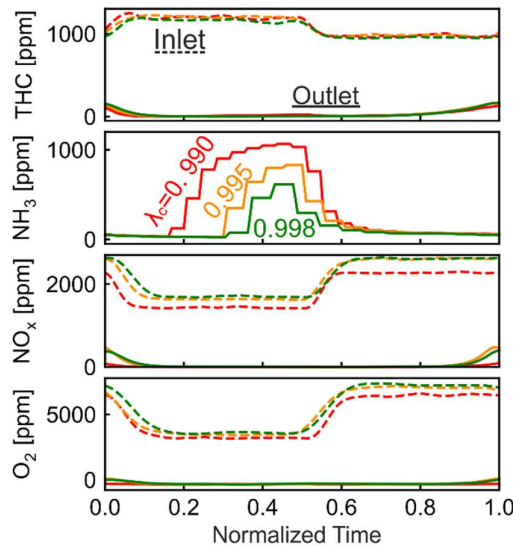


Figure 4:13 THC, NH_3 , NO_x and O_2 concentration profiles for Pt/Pd/Rh catalyst during oscillations with $\lambda_c = 0.990, 0.995$ and 0.998 (corrected λ).

4.2.8 Optimized λ oscillation for the WHSC cycle

To showcase the applicability of the above findings in various real life driving conditions, the Pt/Pd/Rh catalyst was tested under the World Harmonized Steady Cycle (WHSC). For comparison, a Pd/Rh ($65.4/4.6 \text{ g/ft}^3$) catalyst of the same dimension was also tested. Representative engine operating points (except for idling point) were determined based on WHSC regulations [10] and the full engine map. Due to limitations of our engine test bench, the idling point was represented by extreme low load operating point (850 rpm, 50 Nm). For each load point, emissions were measured at steady and oscillating conditions. The steady state measurements were conducted at $\lambda_{\text{sensor}} = 1.00$, and represent the steady state emissions without oscillation strategies. The oscillations were conducted at $\lambda_c = 0.998$ (λ_{corr}), which was calibrated for each operating point. The period length (T) was calculated according to the following equation,

$$T = T_0 \times \frac{\dot{m}_0}{\dot{m}}$$

where T_0 is the period length at reference point, \dot{m} is the mass flow rate, and \dot{m}_0 is the mass flow rate at reference point. The $\lambda_c = 0.998$ oscillation in Figure 4:12 was selected as reference point, which had the best performance in both THC conversion and NH_3 emission. Figure 4:14 summarizes THC and NH_3 emission under steady and oscillating conditions at different load points. In Figure 4:14a, except for the near idling point (850 rpm, 50 Nm), the average THC emissions with oscillations were all below 35 ppm, corresponding to more than 0.97 conversion, while THC emission varied from 60 ppm to 1000 ppm under steady state. The high THC emission occurred especially at high load points (high temperature). This is in line with previously discussed λ ramp results in Figure 4:2 and Figure 4:6a, where CH_4 conversion was close to zero after staying in rich condition for a long period of time (ramp-up). Figure 4:14b (Pd/Rh) reveals similar results, that for steady measurements high THC emissions were observed at high load points. By applying optimized oscillations, the THC emissions were significantly lowered. However, the THC emissions with oscillations were at least 2.5 times higher than the Pt/Pd/Rh catalyst at each operating point (except for the near idling point).

THC emissions (including near idling point) of both catalysts under oscillations were weighted according to the WHSC regulation [10]. The Pt/Pd/Rh catalyst led to 199 mg/kWh THC, while Pd/Rh catalyst resulted in 339 mg/kWh. The comparison demonstrated the benefit of the Pt/Pd/Rh catalyst. The weighted THC emissions for steady state measurements were 1423 and 1585 mg/kWh, respectively. The results suggest that the calibrated oscillation strategies played a key role in lowering THC emissions. The optimization of catalyst composition helped to further reduce THC emissions under oscillation conditions.

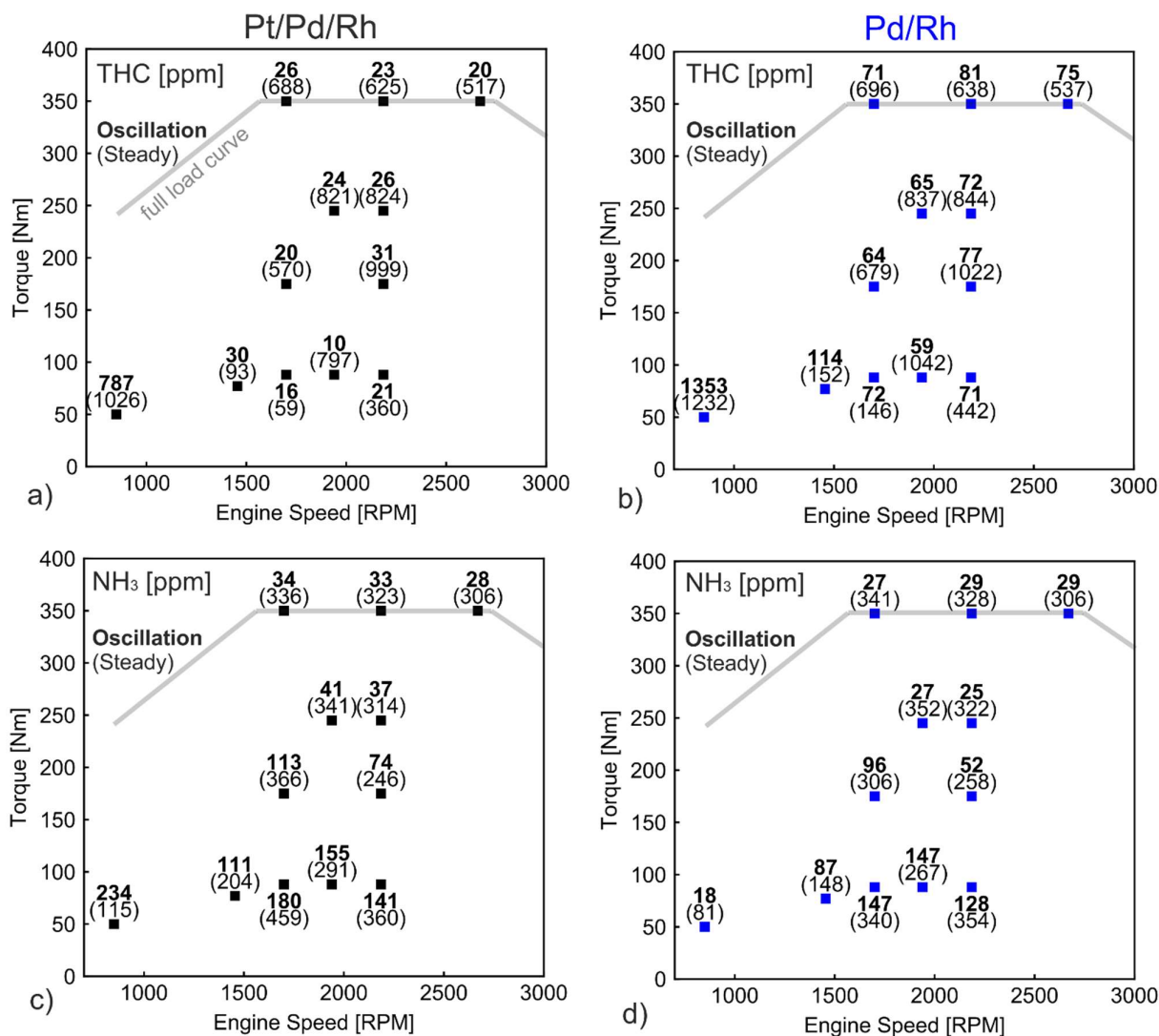


Figure 4:14 THC and NH₃ emission under steady and oscillations in WHSC operating points for a) and c) Pt/Pd/Rh catalyst; b) and d) Pd/Rh catalyst.

The weighted NO_x emission (not shown in Figure 4:14) for the Pt/Pd/Rh catalyst was 104 mg/kWh, while that of the Pd/Rh catalyst was 135 mg/kWh. Both values are well below the regulated emission of 400 mg/kWh in Euro 6 standard. The similarly low NO_x emissions imply that the oscillation period length are well suited for both catalysts, without large breakthrough of NO_x. For both catalysts, optimized oscillation also resulted in lower NH₃ emission compared with steady state results (Figure 4:14 c and d). This can be traced back to the precise λ control during oscillation, allowing large part of NH₃ being oxidized by OSC.

4.3 Conclusions

In this chapter, different characteristics of Pt, Pd and Rh as active catalytic compositions in natural gas engine exhaust were investigated through various targeted test procedures. Pt was found to be more active in methane direct oxidation (by oxygen) than Pd at mid to high temperatures (520–660°C). SR was activated at lower temperatures in the Pt/Rh catalyst than the Pd/Rh. At mid to high temperatures, however, the SR reaction in the Pt/Rh catalyst only lasted shortly was deactivated rapidly. The Pd/Rh catalyst kept SR active for longer time after transition from lean to rich. Regarding CH₄ direct oxidation under lean conditions, the activity of Pd was limited by the less active metallic Pd(0), which was either only slowly oxidized at mid temperatures or stayed unoxidized at high temperatures. The addition of Rh didn't affect the conversion of CH₄. However, Rh was crucial for high NO_x conversion and the selectivity toward N₂.

In view of the complementary functionalities of the different noble metals, a Pt/Pd/Rh catalyst was designed for testing on the engine test bench. Steady high THC conversion could be achieved by means of λ oscillations between lean and rich conditions. Under rich conditions, THC was effectively removed through SR, which occurred on highly active, regenerated catalyst surface. Under lean conditions, the accumulated carbonaceous species on the surface were removed by the excess oxygen. THC conversion increased with oscillation period length, until the period length was too long and resulted in fully filled/depleted OSC. The average NH_3 concentration was proved to depend on the oscillation center λ (λ_c) but was not affected by the length of the oscillation period. NH_3 emissions decreased with λ_c approaching 1.00. The optimized oscillation strategy was applied to various characteristic engine operating points, as defined by the WHSC. For most of the operating points, more than 97% of CH_4 conversion was reached under oscillatory conditions. The NH_3 emission was also reduced in comparison to steady state measurements.

Chapter 5 Investigation of special catalysts layout in combination with pressure-wave charger

Parts of this chapter are published in: N. Zsiga, M.A. Skopil, M. Wang, D. Klein, P. Soltic, *Comparison of Turbocharging and Pressure Wave Supercharging of a Natural Gas Engine for Light Commercial Trucks and Vans*, *Energies*. 14 (2021) 5306. <https://doi.org/10.3390/en14175306>.

In previous chapters, enhancement of methane conversion abatement under oscillation conditions has been proved and demonstrated. While methane emission reaches extremely low levels, NH_3 formed during oscillations have to be further reduced. This chapter assesses a novel aftertreatment setup, which involves further attempts to solve the problem of NH_3 emission, enabled by the installation of an unconventional pressure-wave charger. The setup consists of a Pd/Rh TWC upstream of the pressure-wave charger and an oxidation catalyst downstream. The special design allows a near stoichiometric, high temperature condition at the upstream TWC and oxygen excess conditions at the oxidation catalyst. This setup has a good potential for CO, H_2 and NH_3 abatement via oxidation following their formation in near stoichiometric conditions.

5.1 Experimentals

A special pressure-wave charger (Comprex) was used in this chapter. The first stage Pd/Rh TWC catalyst described in Chapter 2 was mounted upstream of the pressure-wave charger. A Pt oxidation catalyst (OC) originally used for diesel applications was cut into the same diameter as the second stage catalyst in Chapter 2. The length of the OC was 50mm. The OC was mounted downstream of the pressure-wave charger. In the pressure-wave charger, the pressure energy was transferred from the exhaust to the intake side by bringing the two fluids into direct contact for a very short time in long, thin channels [132]. The special design of the pressure wave charger resulted in a mixture of exhaust gas and inlet air in the exhaust duct downstream of the charger. This means that the gas feed was lean downstream of the charger. A scheme of the setup is shown in Figure 5:1a. The results were compared with the turbocharger setup described in Chapter 2, where two stages TWC were used in the aftertreatment system (Figure 5:1b).

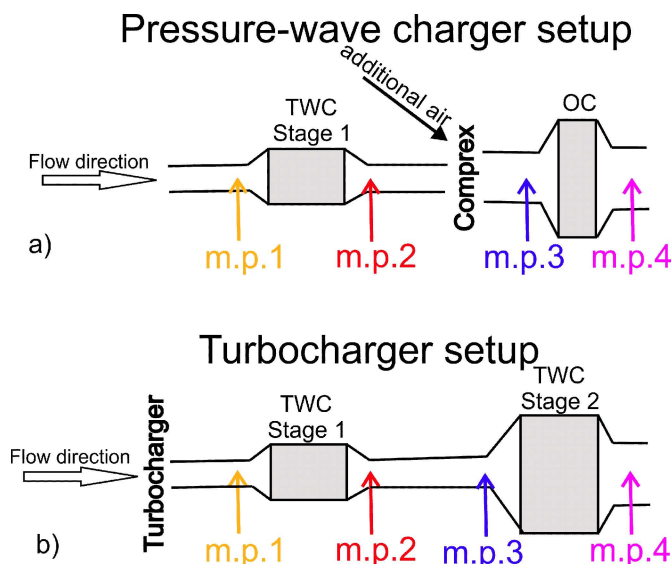


Figure 5:1 Simplified schemes of a) pressure-wave charger setup with one TWC and one OC and b) turbocharger setup with two TWC stages. Measurement points (m.p.1-m.p.4) are also included in the schemes.

Four measurement points were monitored in the setup, from m.p.1 to m.p.4 in Figure 5:1a. Concentrations at m.p.1 and m.p.2 were measured with the Horiba MEXA-74000 described in Chapter 2, while m.p.3 and m.p.4 were measured by the Horiba MEXA-74000, an AVL FTIR and an H-Sense mass spectrometry.

The catalyst performances were investigated under various steady and λ oscillating conditions at characteristic load points. Oscillation strategies were designed according to the knowledge gained in Chapter 3. The λ oscillation amplitude was kept at 0.025 and the oscillation center is at $\lambda_{\text{sensor}} = 1.00$. In addition, cold starts were recorded while the engine warmed up from stand still to the low load operating point 1000 rpm, 50 Nm.

5.2 Results and discussions

The first stage/upstream TWC inlet gas temperature at various operating points are shown in Figure 5:2a for both conventional turbocharger setup (temperatures listed in brackets) and the pressure-wave charger setup (temperature listed without brackets). Compared to conventional turbocharger setup, the TWC in the pressure-wave charger aftertreatment layout was subjected to exhaust gases of 25 to 90 °C higher temperature. The higher inlet temperature for the catalyst meant better conversion in the TWC under the same exhaust gas compositions. The TWC in the pressure-wave charger setup was mounted at the high pressure side of the charging device, which means that the residence time of hot exhaust gas is longer than traditional setups. The long residence time, together with the high temperature (50 °C at operating point 1000rpm, 50Nm) positively affected the warm up behaviors. Significantly faster increase of TWC inlet and outlet temperature under the pressure-wave charger setup (top plot Figure 5:2b) was observed. CO conversion rate of the first stage/upstream TWC during the cold start are plotted in bottom plot of Figure 5:2b. With the pressure-wave charger setup, the time to reach 50% conversion of CO was 14.0 s, while the turbocharger setup needed 91.7s (vertical line in Figure 5:2b). The pressure-wave charger setup shortened the lightoff time by a factor 6. As in real life scenario considerable emissions are resulted from the cold starts [133], the decrease of light-off time with the pressure-wave charger setup is a significant advantage in terms of total emissions.

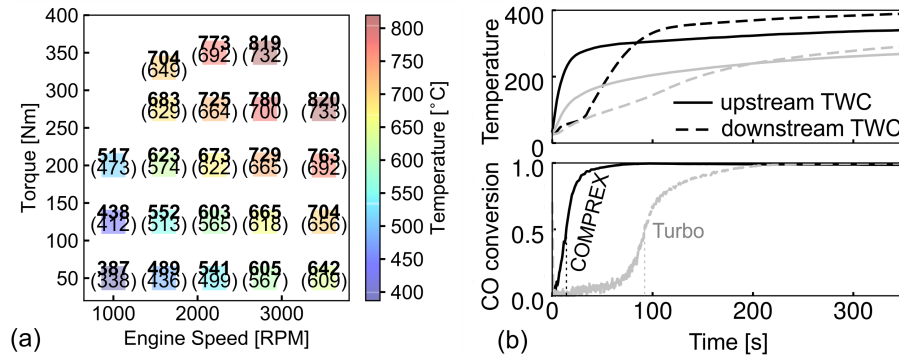


Figure 5:2 a) Temperature of m.p.1 for the conventional turbocharger (brackets) and the pressure-wave charger setup (without brackets), b) Temperature (top) and CO conversion rate (bottom) evolution during cold start for the pressure-wave charger setup (black) and turbocharger setup (grey).

The potential of pollutants conversion of the TWC in pressure-wave charger setup was further studied under steady and oscillating conditions with selected operating conditions (tabulated in Table 5:1). For determination of oscillation period lengths, the load point 1000 rpm 50 Nm was selected as the reference point. Upon shifting to $\lambda = 1.00 \pm 0.025$, OSC of the TWC was fully saturated/depleted after slightly below 8 s. According to the discussions in previous Chapters, the optimal oscillation lean/rich duration is slightly shorter than 8 s. Therefore, the oscillation period length was set at 14 s (7 s lean/rich duration) for 1000 rpm 50 Nm. In testing different engine operating points, the oscillation period lengths were adapted inversely proportional to the mass flow rate (the same as described in section 4.2.8). The conversion of major species under steady and oscillating conditions are plotted in Figure 5:3a. The results of oscillating conditions were averaged over oscillation cycles. It is clear that in combination with appropriate oscillation strategies, the THC conversion rate stayed above 65%, CO conversion rate above 70%, and NO_x was almost 100% converted. Compared to steady operation, oscillations strongly enhanced THC and CO conversions, while the engine out raw emissions (m.p.1, upstream TWC) for steady and oscillating operation were rather similar (Figure 5:3b). The oscillations, however, led to high H_2 concentration at m.p.2 in Figure 5:3c, most likely due to the activation of steam reforming [118]. Both steady and oscillating operations resulted in noticeable high concentration of NH_3 in Figure 5:3c.

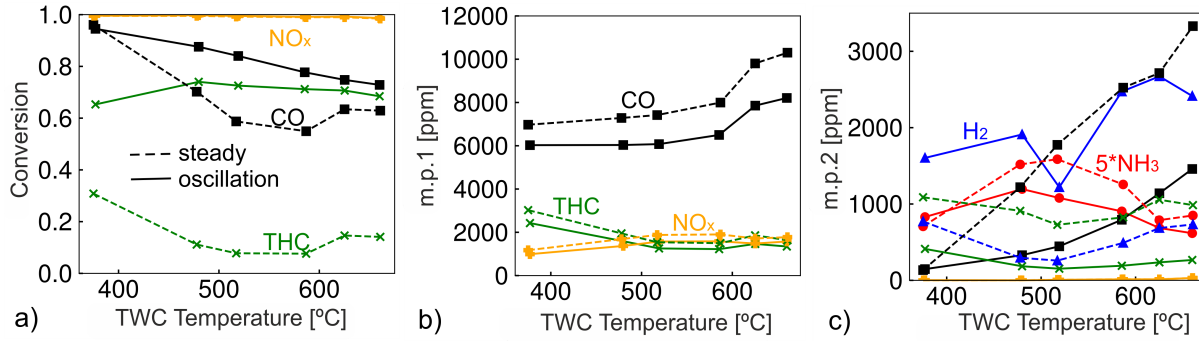


Figure 5:3 a) Conversion rates of NO_x , CO, THC in the TWC, b) concentration of CO, THC, NO_x at m.p.1, c) concentration of CO, THC, NO_x at m.p.2 during steady and oscillating operation.

Engine Speed (rpm)	Torque (Nm)	Temperature inlet TWC (°C)	Temperature inlet OC (°C)
1000	50	375	151
1600	50	477	198
1600	100	517	232
2200	97	586	297
2800	80	625	347
2800	117	660	397

Table 5:1 Engine operating points with corresponding temperature at inlet of TWC and OC.

As described in the section 5.1, the special design of the pressure-wave charger induces mixture of fresh air and exhaust gas in the OC. The unconverted CO, oscillation-induced excess H_2 and NH_3 can be removed by oxidation reactions with the additional oxygen in the OC. CH_4 (main content of THC in the exhaust) is notoriously difficult to be oxidized under lean conditions [49], and was therefore left out of the OC analysis. Figure 5:4a plots the conversions of H_2 , CO and NH_3 at the six operating points tabulated in Table 5:1. The conversion values in Figure 5:4a were not affected by the dilution due to incoming air, because both the concentrations at m.p.3 and m.p.4 were diluted. The OC inlet temperature was higher than 150°C even at the lowest load point (1000 Nm, 50 Nm), which results in near 100% conversion of CO and more than 80% conversion of H_2 under oscillating operation. NH_3 was hardly converted at this low temperature. Unsurprisingly, the NH_3 conversion increased over temperature. NH_3 started to be oxidized at above 200°C and reached more than 80% conversion rate at around 230°C with oscillations. At above 300°C , NH_3 conversion reached 100% with oscillations, while stabilized at around 80% under steady state. During oscillations, NH_3 oxidation was probably enhanced by the periodic oxidation of ceria compounds. As discussed previously, the OC used in our setup was designed for diesel applications, which has excellent oxidation properties toward CO and non-methane hydrocarbons. While oxidizing NH_3 , the selectivity toward N_2 was not optimized with such catalysts. Figure 5:4b plots N_2O , NO and NO_2 concentrations at m.p.4. The concentration values were the actual measured value, with the influence of dilution. The dilution factor was 1.79, 1.77, 1.72, 1.59, 1.48, and 1.38, respectively for the engine operating points listed in Table 5:1. The N_2O and NO_2 concentrations at m.p.3 were below the measurement limits (1 ppm) for all operating points (not shown). NO concentration at m.p.3 was below 15 ppm for all operating points (not shown). This means that all N_2O and NO_2 and the majority of NO measured at m.p.4 were formed in the OC during NH_3 oxidation. At temperatures below 230°C , N_2O was the main side product of NH_3 oxidation. Up to 75 ppm of N_2O was measured at m.p.4 under oscillating conditions. As temperature rose, NH_3 oxidation resulted in further oxidation products: both NO and NO_2 were measured starting from 300°C . At 400°C , NO and NO_2 became the major products of NH_3 oxidation, while less than 15 ppm of N_2O was formed. These results suggested that further catalyst screening is needed to achieve better selectivity toward N_2 .

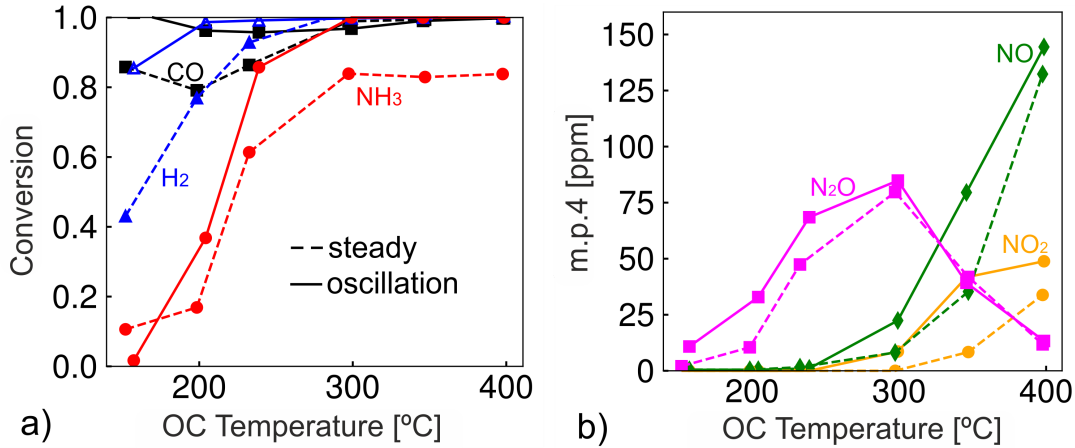


Figure 5:4 a) Conversion rates of H₂, CO, NH₃ in oxidation catalyst, b) concentration of N₂O downstream of TWC during steady and dithering operations.

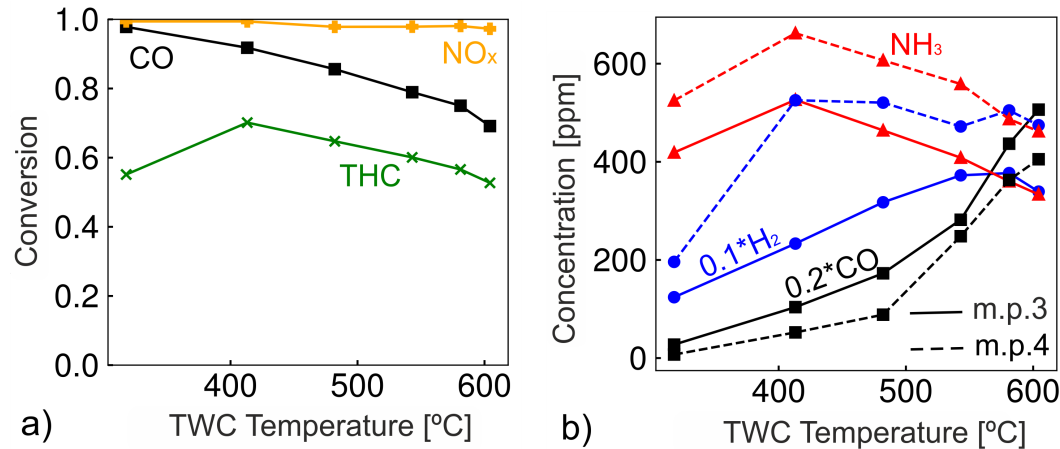


Figure 5:5 a) Conversion rates of NO_x, CO and THC in the first stage TWC under oscillating conditions, b) concentration of H₂, NH₃ and CO at m.p.3 and m.p.4 in the turbocharger setup.

The same oscillating strategy was implemented on the turbocharger aftertreatment setup at the same engine operating conditions, to compare with results of the pressure-wave charger setup. Figure 5:5a plots the conversion of NO_x, CO and THC under oscillating conditions in the first stage catalyst. The six operating points corresponds to those in Table 5:1. The conversions in Figure 5:5a were similar to the results shown in Figure 5:3a (solid lines). This means that even though the TWC was subject to different temperature and pressure conditions, the oscillation strategies were similarly efficient for both setups. In the turbocharger setup, O₂ was completely consumed in the first stage of TWC (not shown) and no additional air was introduced before the second stage TWC. Figure 5:5b plots the H₂, CO and NH₃ concentrations at m.p.3 and m.p.4. CO concentration decreased only slightly from m.p.3 to m.p.4. NH₃ and H₂ concentrations increased from m.p.3 to m.p.4, mostly likely due to SR. Without excess oxygen, the second stage catalyst aggravated the problem of NH₃ and H₂ emissions, while hardly affected the CO emission. These are in contrast to the OC catalyst in the pressure-wave charger setup, which oxidized remaining CO, H₂ and NH₃ at a large temperature ranges.

5.3 Conclusions

In this chapter, a novel aftertreatment setup in combination with a pressure-wave charger was investigated. The system consists of an upstream TWC subjected to high pressure and temperature and a downstream OC subjected to oxygen excess conditions. Due to its position, the TWC achieved a six times faster warmup in cold start conditions, in comparison to the close coupled TWC (stage 1)

in the turbocharger setup. Under oscillating conditions, the TWC converted more than 60% of the THC in both setups. Downstream of the TWC, in the pressure-wave charger, fresh air and exhaust mixed. The H_2 and NH_3 formed in the TWC as well as the remaining CO were oxidized by the excess O_2 in the downstream OC. The pressure-wave charger aftertreatment system had clear advantages over the two-stage TWC setup with conventional turbocharger, in which the under floor TWC (Stage 2) only aggravated the problem of NH_3 and H_2 emission. However, further catalyst screening for higher selectivity NH_3 of the oxidation catalyst is needed to reduce the formation of N_2O , NO and NO_2 .

Chapter 6 Conclusions and outlook

6.1 Achieved results

In this study, steady state and step transitions between oxygen-excess (lean) and oxygen-poor conditions (rich) have been studied performed on the engine test bench with Pd/Rh catalysts. Compared to steady state, a significantly enhanced methane conversion was observed shortly after the step transition from lean to rich conditions. The cause of this enhanced conversion was identified as activation of steam reforming (SR), which was normally deactivated under steady state. Following each transition, the reaction rate of SR decreased over time until full deactivation. The observed and analysed phenomena were validated on the model gas reactor with emulated exhaust gas. This excluded the explanation of sulfur poisoning for SR deactivation. The deactivation process was further studied with DRIFTS investigations. It was found that the slow deactivation process was related to carbonate accumulation on ceria sites.

After identifying the SR related temporary high methane conversions, the focus changed to achieving a sustainable high methane conversion. Implemented fast lean-rich oscillations resulted in activation of SR under rich conditions and regeneration of the surface carbonates under lean conditions. In this way, high methane conversion was sustained. A closer look into one oscillation period revealed a characteristic methane concentration profile (downstream of the catalyst) in the shape of 'W'. The concentration profile featured local maximums at both lean to rich and rich to lean transitions. Two local minimums were located in the lean and rich phase respectively. Four reaction stages could be identified, each corresponding to the period between local minimums and maximums. After the transition from lean to rich condition, SR was activated as the Ce^{4+} (CeO_2) was reduced to Ce^{3+} (Ce_2O_3). This was followed by a SR deactivation stage, during which carbonates begin to accumulate on the catalyst surface and block Ce^{3+} sites. The start of the third stage was marked by the transition from rich to lean condition. This was a SR enhancement stage. CO in the feed was immediately oxidized by the incoming excess oxygen, which reduced the competition between CH_4 and CO for active sites. At the same time, ceria compounds were still largely in reduced form. The fourth stage was marked by a decrease of methane conversion. As Ce^{3+} was gradually oxidized to Ce^{4+} , the surface started to be covered by adsorbed oxygen and CH_4 activation was inhibited. SR gave way to complete oxidation by oxygen. A simulation model was developed to validate the proposed reaction mechanism and to aid further analysis of the catalyst behavior. It was found that the optimal oscillation frequency was inversely proportional to the time needed for completely oxidizing OSC. Long oscillation periods allowed a larger part of the catalyst to participate in the deactivation/regeneration cycle, and therefore resulted in higher methane conversion. However, too long oscillation periods led to unwanted NO_x breakthrough. The best oscillation period was slightly below the time needed for complete oxidation/reduction of OSC.

Apart from identifying and implementing optimal operation strategies, the influence of catalyst composition was also studied. Catalysts with different combinations of Platinum-group metals were investigated. It was found that both Pt and Pd were able to activate SR after transition from lean to rich conditions. However, the SR deactivation happened much faster with Pt. On the lean side, comparing to Pt catalysts, Pd catalysts had low methane conversion at near stoichiometric conditions. This was related to Pd/PdO transition. Metallic Pd, which dominated the surface at near stoichiometric conditions, exhibited lower methane oxidation activity than PdO. The conversion increased as Pd was oxidized to PdO. In contrast, Pt stayed in its active metallic form and resulted in higher conversion at near stoichiometric conditions. Rh was not relevant for methane conversion but essential for NO_x reduction. Catalysts with Rh addition exhibited higher NO_x conversion and higher selectivity toward N_2 . Based on the complementary advantages of the three Platinum-group metals, a Pt/Pd/Rh catalyst was produced and investigated with quasi-steady state and transient procedures. The Pt/Pd/Rh catalyst encompassed advantages of all three metals. In addition, NH_3 emissions were analyzed with various oscillation parameters. The level of NH_3 emission was independent of oscillation periods but was strongly influenced by the average air to fuel ratio. The advantage of Pt/Pd/Rh catalyst was further confirmed following world harmonized stationary cycle tests.

Finally a special aftertreatment layout, in combination with a pressure-wave charger, was investigated. The special layout consisted of a Pd/Rh TWC upstream of the charger (under high pressure and temperature) and an OC downstream (operating under oxygen abundance). The design of the pressure-wave charger resulted in exhaust gas mixing with an amount of fresh air in the intake. The contact brought a small amount of air into the aftertreatment system and led to lean conditions at the OC. The aftertreatment system had significant advantage during cold starts, due to the TWC location upstream the charger. In addition, the setup had the advantage of removing methane at the upstream TWC via targeted oscillations and oxidizing the remaining CO, H_2 and NH_3 at the downstream

OC with the help of excess oxygen. However, the OC was highly unselective when oxidizing the NH_3 . Strong formation of N_2O (up to 75 ppm) was observed at low temperatures ($< 300^\circ\text{C}$). NO and NO_2 were observed as oxidation products at higher temperatures ($> 300^\circ\text{C}$). These suggest that, even though the special aftertreatment system had promising advantages, further studies on improving the NH_3 oxidation selectivity toward N_2 are needed.

6.2 Future development

Even though the current work has helped with advancing knowledge in catalytic abatement of methane and other hazardous pollutant emissions in natural gas engine exhausts, significant efforts are still needed to further understand the reaction pathways and to achieve near zero environmental impacts.

The palladium oxidation state has important impacts on conversion behaviors of TWCs. Under the typical temperature range of exhaust gases ($300 - 700^\circ\text{C}$), both the oxidation and the reduction of palladium are complex processes, involving many intermediate structures and states of palladium compounds. The engine test bench and the model gas reactor used in this study have their limitations in monitoring such processes. Future studies, in combination with XAS techniques, can enhance understandings of the exact role of different palladium states.

In studying characteristics of different metals, the alloy effect of Platinum-group metals have not been further studied. The formation of alloys can potentially affect oxidizability/reducibility of Platinum-group metals. An optimized metal distribution along the catalyst may also contribute in improving emission abatement characteristics. A thorough optimization of the catalyst compositions could be very interesting.

The formation of NH_3 is still an unsolved issue. As discussed, the emission of NH_3 during oscillation is highly dependent on average λ values. We have shown that an accuracy of 0.2% is needed to significantly reduce NH_3 emissions. However, the state of art λ sensor accuracy is 2%. The use of two different lambda sensors (one with an analog response the other with a step response) and suitable control strategies can improve the situation. In addition to sensor and control strategy updates, further optimization of catalyst compositions for lower NH_3 selectivity can provide further promising solutions.

References

- [1] N. Khanna, H. Lu, D. Fridley, N. Zhou, Near and long-term perspectives on strategies to decarbonize China's heavy-duty trucks through 2050, *Sci. Rep.* 11 (2021) 20414. <https://doi.org/10.1038/s41598-021-99715-w>.
- [2] P. Kluschke, T. Gnann, P. Plötz, M. Wietschel, Market diffusion of alternative fuels and powertrains in heavy-duty vehicles: A literature review, *Energy Reports*. 5 (2019) 1010–1024. <https://doi.org/10.1016/j.egy.2019.07.017>.
- [3] J.M. López, Á. Gómez, F. Aparicio, F. Javier Sánchez, Comparison of GHG emissions from diesel, biodiesel and natural gas refuse trucks of the City of Madrid, *Appl. Energy*. 86 (2009) 610–615. <https://doi.org/10.1016/j.apenergy.2008.08.018>.
- [4] F. Kiefer, K. Schröter, P. Dimopoulos Eggenschwiler, C. Bach, Significance of Synthetic Methane for Energy Storage and CO₂ Reduction in the Mobility, in: 21. Int. Stuttgarter Symp., Springer Fachmedien Wiesbaden, 2021: pp. 77–92. https://doi.org/10.1007/978-3-658-33521-2_6.
- [5] A. Gremminger, J. Pihl, M. Casapu, J.D. Grunwaldt, T.J. Toops, O. Deutschmann, PGM based catalysts for exhaust-gas after-treatment under typical diesel, gasoline and gas engine conditions with focus on methane and formaldehyde oxidation, *Appl. Catal. B Environ.* 265 (2020) 118571. <https://doi.org/10.1016/j.apcatb.2019.118571>.
- [6] O. Boucher, P. Friedlingstein, B. Collins, K.P. Shine, The indirect global warming potential and global temperature change potential due to methane oxidation, *Environ. Res. Lett.* 4 (2009) 044007. <https://doi.org/10.1088/1748-9326/4/4/044007>.
- [7] K. Houghton, J.T., Y. Ding, D.J. Griggs, M. Noguer, P.J. van der Linden, X. Dai, and C.A.J. (eds. . Maskell, IPCC, 2001: Climate Change 2001: The Scientific Basis. Contribution of Working Group I to the Third Assessment Report of the Intergovernmental Panel on Climate Change, 2001. <https://www.ipcc.ch/report/ar3/wg1/>.
- [8] M. Li, H. Tian, Z. Wei, Q. Zhang, B. Shen, Ammonia and nitrous oxide emissions of a stoichiometric natural gas engine operating with high caloric value and low caloric value fuels, *Fuel*. 285 (2021) 119166. <https://doi.org/10.1016/j.fuel.2020.119166>.
- [9] I. Mejía-Centeno, S. Castillo, G.A. Fuentes, Enhanced emissions of NH₃, N₂O and H₂ from a Pd-only TWC and supported Pd model catalysts: Light-off and sulfur level studies, *Appl. Catal. B Environ.* 119–120 (2012) 234–240. <https://doi.org/10.1016/j.apcatb.2012.02.030>.
- [10] European Parliament And The Council Of The European Union, Regulation (EC) No 595/2009 on type-approval of motor vehicles and engines with respect to emissions from heavy duty vehicles (Euro VI) and on access to vehicle repair and maintenance information and amending Regulation (EC) No 715/2007 and Directive 2007, 2009.
- [11] D. Thompson, T.D. Brown, J.M. Beér, NO_x formation in combustion, *Combust. Flame*. 19 (1972) 69–79. [https://doi.org/10.1016/S0010-2180\(72\)80087-7](https://doi.org/10.1016/S0010-2180(72)80087-7).
- [12] D.L. Mauzerall, B. Sultan, N. Kim, D.F. Bradford, NO_x emissions from large point sources: Variability in ozone production, resulting health damages and economic costs, *Atmos. Environ.* 39 (2005) 2851–2866. <https://doi.org/10.1016/j.atmosenv.2004.12.041>.
- [13] D.A. Pierpont, D.T. Montgomery, R.D. Reitz, Reducing Particulate and NO_x Using Multiple Injections and EGR in a D.I. Diesel, in: *SAE Tech. Pap.*, 1995: pp. 171–183. <https://doi.org/10.4271/950217>.
- [14] W. Mingrui, N. Thanh Sa, R.F. Turkson, L. Jinping, G. Guanlun, Water injection for higher engine performance and lower emissions, *J. Energy Inst.* 90 (2017) 285–299. <https://doi.org/10.1016/j.joei.2015.12.003>.
- [15] X. He, R.P. Durrett, Z. Sun, Late Intake Valve Closing as an Emissions Control Strategy at Tier 2 Bin 5 Engine-Out NO_x Level, *SAE Int. J. Engines*. 1 (2008) 2008-01-0637. <https://doi.org/10.4271/2008-01-0637>.
- [16] H. Lin, M. Wang, Y. Duan, Q. Fu, W. Ji, H. Cui, D. Jin, Y. Lin, K. Hu, O₃ Sensitivity and Contributions of Different NMHC Sources in O₃ Formation at Urban and Suburban Sites in Shanghai, *Atmosphere (Basel)*. 11 (2020) 295. <https://doi.org/10.3390/atmos11030295>.
- [17] S. Lee, U.H. Yi, H. Jang, C. Park, C. Kim, Evaluation of emission characteristics of a stoichiometric natural gas engine fueled with compressed natural gas and biomethane, *Energy*. 220 (2021) 119766. <https://doi.org/10.1016/j.energy.2021.119766>.
- [18] M. Vojtišek-Lom, V. Beránek, V. Klír, P. Jindra, M. Pechout, T. Voříšek, On-road and laboratory emissions of NO, NO₂, NH₃,

- N₂O and CH₄ from late-model EU light utility vehicles: Comparison of diesel and CNG, *Sci. Total Environ.* 616–617 (2018) 774–784. <https://doi.org/10.1016/j.scitotenv.2017.10.248>.
- [19] S.N. Behera, M. Sharma, Degradation of SO₂, NO₂ and NH₃ leading to formation of secondary inorganic aerosols: An environmental chamber study, *Atmos. Environ.* 45 (2011) 4015–4024. <https://doi.org/10.1016/j.atmosenv.2011.04.056>.
- [20] R.J. Levy, Carbon monoxide pollution and neurodevelopment: A public health concern, *Neurotoxicol. Teratol.* 49 (2015) 31–40. <https://doi.org/10.1016/j.ntt.2015.03.001>.
- [21] P. Dimopoulos Eggenschwiler, D. Schreiber, K. Schröter, Characterization of the emission of particles larger than 10 nm in the exhaust of modern gasoline and CNG light duty vehicles, *Fuel*. 291 (2021). <https://doi.org/10.1016/j.fuel.2020.120074>.
- [22] J. Alanen, E. Saukko, K. Lehtoranta, T. Murtonen, H. Timonen, R. Hillamo, P. Karjalainen, H. Kuuluvainen, J. Harra, J. Keskinen, T. Rönkkö, The formation and physical properties of the particle emissions from a natural gas engine, *Fuel*. 162 (2015) 155–161. <https://doi.org/10.1016/j.fuel.2015.09.003>.
- [23] B. Sharpe, R. Muncrief, Literature Review: Real-World Fuel Consumption of Heavy-Duty Vehicles in the United States, China, and the European Union, 2015. http://www.theicct.org/sites/default/files/publications/ICCT_HDV_FC_lit-review_20150209.pdf.
- [24] ICCT, China's Stage VI emission standard for heavy-duty vehicles (final rule), 2018. www.theicct.org/sites/default/files/publications/China_VI_Policy_Update_20180720.pdf.
- [25] Environmental Protection Agency (EPA), 40 CFR 86.007–11 - Emission standards and supplemental requirements for 2007 and later model year diesel heavy-duty engines and vehicles, 2003.
- [26] California Air Resources Board, Final Regulation Order California, 2020.
- [27] J.H. Lee, D.L. Trimm, Catalytic combustion of methane, *Fuel Process. Technol.* 42 (1995) 339–359. [https://doi.org/10.1016/0378-3820\(94\)00091-7](https://doi.org/10.1016/0378-3820(94)00091-7).
- [28] Z. Boukha, B. de Rivas, J.R. González-Velasco, J.I. Gutiérrez-Ortiz, R. López-Fonseca, Comparative study of the efficiency of different noble metals supported on hydroxyapatite in the catalytic lean methane oxidation under realistic conditions, *Materials (Basel)*. 14 (2021). <https://doi.org/10.3390/ma14133612>.
- [29] Y. Zhang, P. Glarborg, K. Johansen, M.P. Andersson, T.K. Torp, A.D. Jensen, J.M. Christensen, A Rhodium-Based Methane Oxidation Catalyst with High Tolerance to H₂O and SO₂, *ACS Catal.* 10 (2020) 1821–1827. <https://doi.org/10.1021/acscatal.9b04464>.
- [30] P.N. Plessow, F. Abild-Pedersen, Sintering of Pt Nanoparticles via Volatile PtO₂: Simulation and Comparison with Experiments, *ACS Catal.* 6 (2016) 7098–7108. <https://doi.org/10.1021/acscatal.6b01646>.
- [31] T.R. Johns, R.S. Goeke, V. Ashbacher, P.C. Thüne, J.W. Niemantsverdriet, B. Kiefer, C.H. Kim, M.P. Balogh, A.K. Datye, Relating adatom emission to improved durability of Pt-Pd diesel oxidation catalysts, *J. Catal.* 328 (2015) 151–164. <https://doi.org/10.1016/j.jcat.2015.03.016>.
- [32] A.I. Stadnichenko, V. V. Muravev, S. V. Koscheev, V.I. Zaikovskii, H.A. Aleksandrov, K.M. Neyman, A.I. Boronin, Study of active surface centers of Pt/CeO₂ catalysts prepared using radio-frequency plasma sputtering technique, *Surf. Sci.* 679 (2019) 273–283. <https://doi.org/10.1016/j.susc.2018.10.002>.
- [33] R. Burch, A. Ramli, A comparative investigation of the reduction of NO by CH₄ on Pt, Pd, and Rh catalysts, *Appl. Catal. B Environ.* 15 (1998) 49–62. [https://doi.org/10.1016/S0926-3373\(97\)00036-2](https://doi.org/10.1016/S0926-3373(97)00036-2).
- [34] C. Carrillo, T.R. Johns, H. Xiong, A. Delariva, S.R. Challa, R.S. Goeke, K. Artyushkova, W. Li, C.H. Kim, A.K. Datye, Trapping of mobile Pt species by PdO nanoparticles under oxidizing conditions, *J. Phys. Chem. Lett.* 5 (2014) 2089–2093. <https://doi.org/10.1021/jz5009483>.
- [35] X. Chen, J.W. Schwank, G.B. Fisher, Y. Cheng, M. Jagner, R.W. McCabe, M.B. Katz, G.W. Graham, X. Pan, Nature of the two-step temperature-programmed decomposition of PdO supported on alumina, *Appl. Catal. A Gen.* 475 (2014) 420–426. <https://doi.org/10.1016/j.apcata.2014.01.056>.
- [36] S. Colussi, A. Trovarelli, E. Vesselli, A. Baraldi, G. Comelli, G. Groppi, J. Llorca, Structure and morphology of Pd/Al₂O₃ and Pd/CeO₂/Al₂O₃ combustion catalysts in Pd-PdO transformation hysteresis, *Appl. Catal. A Gen.* 390 (2010) 1–10. <https://doi.org/10.1016/j.apcata.2010.09.033>.

- [37] S. Colussi, A. Trovarelli, G. Groppi, J. Llorca, The effect of CeO₂ on the dynamics of Pd-PdO transformation over Pd/Al₂O₃ combustion catalysts, *Catal. Commun.* 8 (2007) 1263–1266. <https://doi.org/10.1016/j.catcom.2006.11.020>.
- [38] S.K. Matam, M.H. Aguirre, A. Weidenkaff, D. Ferri, Revisiting the Problem of Active Sites for Methane Combustion on Pd/Al₂O₃ by Operando XANES in a Lab-Scale Fixed-Bed Reactor, *J. Phys. Chem. C* 114 (2010) 9439–9443. <https://doi.org/10.1021/jp1019697>.
- [39] X. Zheng, Y. Shi, X. Wang, N. Cai, Elementary reaction modeling of methane catalytic combustor: Effects of hysteresis in pd-based catalyst activity, *Combust. Sci. Technol.* 187 (2015) 1044–1064. <https://doi.org/10.1080/00102202.2014.1001843>.
- [40] S.K. Matam, G.L. Chiarello, Y. Lu, A. Weidenkaff, D. Ferri, PdO x /Pd at Work in a Model Three-Way Catalyst for Methane Abatement Monitored by Operando XANES, *Top. Catal.* 56 (2013) 239–242. <https://doi.org/10.1007/s11244-013-9960-1>.
- [41] Y.H.C. Chin, M. García-Diéguez, E. Iglesia, Dynamics and thermodynamics of Pd-PdO phase transitions: Effects of pd cluster size and kinetic implications for catalytic methane combustion, *J. Phys. Chem. C* 120 (2016) 1446–1460. <https://doi.org/10.1021/acs.jpcc.5b06677>.
- [42] D. Bounechada, G. Groppi, P. Forzatti, K. Kallinen, T. Kinnunen, Effect of periodic lean/rich switch on methane conversion over a Ce-Zr promoted Pd-Rh/Al₂O₃ catalyst in the exhausts of natural gas vehicles, *Appl. Catal. B Environ.* 119–120 (2012) 91–99. <https://doi.org/10.1016/j.apcatb.2012.02.025>.
- [43] T. Franken, M. Roger, A.W. Petrov, A.H. Clark, M. Agote-Arán, F. Krumeich, O. Kröcher, D. Ferri, Effect of Short Reducing Pulses on the Dynamic Structure, Activity, and Stability of Pd/Al₂O₃ for Wet Lean Methane Oxidation, *ACS Catal.* 11 (2021) 4870–4879. <https://doi.org/10.1021/acscatal.1c00328>.
- [44] P. Lott, P. Dolcet, M. Casapu, J.-D. Grunwaldt, O. Deutschmann, The Effect of Prereduction on the Performance of Pd/Al₂O₃ and Pd/CeO₂ Catalysts during Methane Oxidation, *Ind. Eng. Chem. Res.* 58 (2019) 12561–12570. <https://doi.org/10.1021/acs.iecr.9b01267>.
- [45] A.W. Petrov, D. Ferri, F. Krumeich, M. Nachtegaal, J.A. van Bokhoven, O. Kröcher, Stable complete methane oxidation over palladium based zeolite catalysts, *Nat. Commun.* 9 (2018) 2545. <https://doi.org/10.1038/s41467-018-04748-x>.
- [46] W. Qi, J. Ran, R. Wang, X. Du, J. Shi, J. Niu, P. Zhang, M. Ran, Kinetic consequences of methane combustion on Pd, Pt and Pd-Pt catalysts, *RSC Adv.* 6 (2016) 109834–109845. <https://doi.org/10.1039/c6ra21150j>.
- [47] Y.H. Chin, E. Iglesia, Elementary steps, the role of chemisorbed oxygen, and the effects of cluster size in catalytic CH₄-O₂ reactions on palladium, *J. Phys. Chem. C* 115 (2011) 17845–17855. <https://doi.org/10.1021/jp203324y>.
- [48] S. OH, Methane oxidation over alumina-supported noble metal catalysts with and without cerium additives, *J. Catal.* 132 (1991) 287–301. [https://doi.org/10.1016/0021-9517\(91\)90149-X](https://doi.org/10.1016/0021-9517(91)90149-X).
- [49] R. Hutter, L. De Libero, P. Elbert, C.H. Onder, Catalytic methane oxidation in the exhaust gas aftertreatment of a lean-burn natural gas engine, *Chem. Eng. J.* 349 (2018) 156–167. <https://doi.org/10.1016/j.cej.2018.05.054>.
- [50] D. Ferri, M. Elsener, O. Kröcher, Methane oxidation over a honeycomb Pd-only three-way catalyst under static and periodic operation, *Appl. Catal. B Environ.* 220 (2018) 67–77. <https://doi.org/10.1016/j.apcatb.2017.07.070>.
- [51] C. Coney, C. Stere, P. Millington, A. Raj, S. Wilkinson, M. Caracotsios, G. McCullough, C. Hardacre, K. Morgan, D. Thompsett, A. Goguet, Spatially-resolved investigation of the water inhibition of methane oxidation over palladium, *Catal. Sci. Technol.* 10 (2020) 1858–1874. <https://doi.org/10.1039/D0CY00154F>.
- [52] R. Gholami, M. Alyani, K. Smith, Deactivation of Pd Catalysts by Water during Low Temperature Methane Oxidation Relevant to Natural Gas Vehicle Converters, *Catalysts*. 5 (2015) 561–594. <https://doi.org/10.3390/catal5020561>.
- [53] H. Stotz, L. Maier, O. Deutschmann, Methane Oxidation over Palladium: On the Mechanism in Fuel-Rich Mixtures at High Temperatures, *Top. Catal.* 60 (2017) 83–109. <https://doi.org/10.1007/s11244-016-0717-5>.
- [54] S.M. Vesecky, J. Paul, D.W. Goodman, Catalytic Reduction of Nitrogen Oxides by Methane over Pd(110), *J. Phys. Chem.* 100 (1996) 15242–15246. <https://doi.org/10.1021/jp961644p>.
- [55] X. Weng, H. Ren, M. Chen, H. Wan, Effect of surface oxygen on the activation of methane on palladium and platinum surfaces, *ACS Catal.* 4 (2014) 2598–2604. <https://doi.org/10.1021/cs500510x>.
- [56] M.H. Halabi, M.H.J.M. De Croon, J. Van Der Schaaf, P.D. Cobden, J.C. Schouten, Low temperature catalytic methane steam

- reforming over ceria-zirconia supported rhodium, *Appl. Catal. A Gen.* 389 (2010) 68–79. <https://doi.org/10.1016/j.apcata.2010.09.004>.
- [57] J.G. Jakobsen, M. Jakobsen, I. Chorkendorff, J. Sehested, Methane Steam Reforming Kinetics for a Rhodium-Based Catalyst, *Catal. Letters.* 140 (2010) 90–97. <https://doi.org/10.1007/s10562-010-0436-7>.
- [58] S.D. Angeli, G. Monteleone, A. Giaconia, A.A. Lemonidou, State-of-the-art catalysts for CH₄ steam reforming at low temperature, *Int. J. Hydrogen Energy.* 39 (2014) 1979–1997. <https://doi.org/10.1016/j.ijhydene.2013.12.001>.
- [59] W. Kumsung, M. Chareonpanich, P. Kongkachuichay, S. Senkan, A. Seubsai, Single and bimetallic catalyst screenings of noble metals for methane combustion, *Catal. Commun.* 110 (2018) 83–87. <https://doi.org/10.1016/j.catcom.2018.03.022>.
- [60] R. Craciun, B. Shereck, R.J. Gorte, Kinetic studies of methane steam reforming on ceria-supported Pd, *Catal. Letters.* 51 (1998) 149–153. <https://doi.org/https://doi.org/10.1023/A:1019022009310>.
- [61] M.H. Halabi, M.H.J.M. De Croon, J. Van Der Schaaf, P.D. Cobden, J.C. Schouten, Intrinsic kinetics of low temperature catalytic methane-steam reforming and water-gas shift over Rh/Ce α Zr1- α O₂ catalyst, *Appl. Catal. A Gen.* 389 (2010) 80–91. <https://doi.org/10.1016/j.apcata.2010.09.005>.
- [62] R.B. Duarte, M. Olea, E. Iro, T. Sasaki, K. Itako, J.A. Van Bokhoven, Transient mechanistic studies of methane steam reforming over ceria-promoted Rh/Al₂O₃ catalysts, *ChemCatChem.* 6 (2014) 2898–2903. <https://doi.org/10.1002/cctc.201402388>.
- [63] R.B. Duarte, O. V. Safonova, F. Krumeich, M. Makosch, J.A. Van Bokhoven, Oxidation state of Ce in CeO₂-promoted Rh/Al₂O₃ catalysts during methane steam reforming: H₂O activation and alumina stabilization, *ACS Catal.* 3 (2013) 1956–1964. <https://doi.org/10.1021/cs400207c>.
- [64] S. Hilaire, X. Wang, T. Luo, R.J. Gorte, J. Wagner, A comparative study of water-gas-shift reaction over ceria-supported metallic catalysts, *Appl. Catal. A Gen.* 258 (2004) 271–276. <https://doi.org/10.1016/j.apcata.2003.09.026>.
- [65] S. Zhao, T. Luo, R.J. Gorte, Deactivation of the water–gas-shift activity of Pd/ceria by Mo, *J. Catal.* 221 (2004) 413–420. <https://doi.org/10.1016/j.jcat.2003.09.004>.
- [66] Q. Fu, W. Deng, H. Saltsburg, M. Flytzani-Stephanopoulos, Activity and stability of low-content gold–cerium oxide catalysts for the water–gas shift reaction, *Appl. Catal. B Environ.* 56 (2005) 57–68. <https://doi.org/10.1016/j.apcatb.2004.07.015>.
- [67] X. Liu, W. Ruettinger, X. Xu, R. Farrauto, Deactivation of Pt/CeO₂ water-gas shift catalysts due to shutdown/startup modes for fuel cell applications, *Appl. Catal. B Environ.* 56 (2005) 69–75. <https://doi.org/10.1016/j.apcatb.2004.04.026>.
- [68] C.H. Kim, L.T. Thompson, Deactivation of Au/CeO_x water gas shift catalysts, *J. Catal.* 230 (2005) 66–74. <https://doi.org/10.1016/j.jcat.2004.10.004>.
- [69] F. Watanabe, I. Kaburaki, N. Shimoda, A. Igarashi, S. Satokawa, Sulfur tolerance of noble metal catalysts for steam methane reforming, *J. Japan Pet. Inst.* 60 (2017) 137–145. <https://doi.org/10.1627/jpi.60.137>.
- [70] A. Gremminger, P. Lott, M. Merts, M. Casapu, J.D. Grunwaldt, O. Deutschmann, Sulfur poisoning and regeneration of bimetallic Pd-Pt methane oxidation catalysts, *Appl. Catal. B Environ.* 218 (2017) 833–843. <https://doi.org/10.1016/j.apcatb.2017.06.048>.
- [71] S. Cimino, L. Lisi, Impact of sulfur poisoning on the catalytic partial oxidation of methane on rhodium-based catalysts, *Ind. Eng. Chem. Res.* 51 (2012) 7459–7466. <https://doi.org/10.1021/ie201648e>.
- [72] P. Lott, M. Eck, D.E. Doronkin, A. Zimina, S. Tischer, R. Popescu, S. Belin, V. Briois, M. Casapu, J.D. Grunwaldt, O. Deutschmann, Understanding sulfur poisoning of bimetallic Pd-Pt methane oxidation catalysts and their regeneration, *Appl. Catal. B Environ.* 278 (2020). <https://doi.org/10.1016/j.apcatb.2020.119244>.
- [73] S.H. Oh, T. Triplett, Reaction pathways and mechanism for ammonia formation and removal over palladium-based three-way catalysts: Multiple roles of CO, *Catal. Today.* 231 (2014) 22–32. <https://doi.org/10.1016/j.cattod.2013.11.048>.
- [74] W. Ding, W. Li, First-principles study of NO reduction by CO on transition metal atoms-doped CeO₂(111), *Chinese J. Catal.* 35 (2014) 1937–1943. [https://doi.org/10.1016/S1872-2067\(14\)60169-8](https://doi.org/10.1016/S1872-2067(14)60169-8).
- [75] C. Wang, J. Tan, G. Harle, H. Gong, W. Xia, T. Zheng, D. Yang, Y. Ge, Y. Zhao, Ammonia Formation over Pd/Rh Three-Way Catalysts during Lean-to-Rich Fluctuations: The Effect of the Catalyst Aging, Exhaust Temperature, Lambda, and Duration in Rich Conditions, *Environ. Sci. Technol.* 53 (2019) 12621–12628. <https://doi.org/10.1021/acs.est.9b03893>.

- [76] I. Mejía-Centeno, A. Martínez-Hernández, G.A. Fuentes, Effect of low-sulfur fuels upon NH₃ and N₂O emission during operation of commercial three-way catalytic converters, *Top. Catal.* 42–43 (2007) 381–385. <https://doi.org/10.1007/s11244-007-0210-2>.
- [77] E.C. Adams, M. Skoglundh, M. Folic, E.C. Bendixen, P. Gabrielsson, P.A. Carlsson, Ammonia formation over supported platinum and palladium catalysts, *Appl. Catal. B Environ.* 165 (2015) 10–19. <https://doi.org/10.1016/j.apcatb.2014.09.064>.
- [78] E.C. Adams, M. Skoglundh, T. Elmqvist, P.A. Carlsson, Water–gas–shift assisted ammonia formation over Pd/Ce/alumina, *Catal. Today*. 307 (2018) 169–174. <https://doi.org/10.1016/j.cattod.2017.05.035>.
- [79] E.C. Adams, M. Skoglundh, P. Gabrielsson, M. Laurell, P.A. Carlsson, Ammonia formation over Pd/Al₂O₃ modified with cerium and barium, *Catal. Today*. 267 (2016) 210–216. <https://doi.org/10.1016/j.cattod.2016.01.012>.
- [80] Y. Renème, F. Dhainaut, P. Granger, Kinetics of the NO/H₂/O₂ reactions on natural gas vehicle catalysts-Influence of Rh addition to Pd, *Appl. Catal. B Environ.* 111–112 (2012) 424–432. <https://doi.org/10.1016/j.apcatb.2011.10.030>.
- [81] T. Zheng, B. Lu, G. Harle, D. Yang, C. Wang, Y. Zhao, A comparative study of Rh-only, Pd-only and Pd/Rh catalysts, *Appl. Catal. A Gen.* 602 (2020) 117649. <https://doi.org/10.1016/j.apcata.2020.117649>.
- [82] A. Holmgren, B. Andersson, Mass transfer in monolith catalysts - CO oxidation experiments and simulations, *Doktorsavhandlingar Vid Chalmers Tek. Hogsk.* 53 (1998) 2285–2298.
- [83] D.N. Tsinoglou, P.D. Eggenschwiler, T. Thurnheer, P. Hofer, A simplified model for natural-gas vehicle catalysts with honeycomb and foam substrates, *Proc. Inst. Mech. Eng. Part D J. Automob. Eng.* 223 (2009) 819–834. <https://doi.org/10.1243/09544070JAUTO1095>.
- [84] N. Mladenov, J. Koop, S. Tischer, O. Deutschmann, Modeling of transport and chemistry in channel flows of automotive catalytic converters, *Chem. Eng. Sci.* 65 (2010) 812–826. <https://doi.org/10.1016/j.ces.2009.09.034>.
- [85] J. Koop, O. Deutschmann, Detailed surface reaction mechanism for Pt-catalyzed abatement of automotive exhaust gases, *Appl. Catal. B Environ.* 91 (2009) 47–58. <https://doi.org/10.1016/j.apcatb.2009.05.006>.
- [86] F. Zeng, K.L. Hohn, Modeling of three-way catalytic converter performance with exhaust mixture from natural gas-fueled engines, *Appl. Catal. B Environ.* 182 (2016) 570–579. <https://doi.org/10.1016/j.apcatb.2015.10.004>.
- [87] G.P. Ansell, P.S. Bennett, J.P. Cox, J.C. Frost, P.G. Gray, A.-M. Jones, R.R. Rajaram, A.P. Walker, M. Litorell, G. Smedler, The development of a model capable of predicting diesel lean NO_x catalyst performance under transient conditions, *Appl. Catal. B Environ.* 10 (1996) 183–201. [https://doi.org/10.1016/0926-3373\(96\)00030-6](https://doi.org/10.1016/0926-3373(96)00030-6).
- [88] S.E. Voltz, C.R. Morgan, D. Liederman, S.M. Jacob, Kinetic Study of Carbon Monoxide and Propylene Oxidation on Platinum Catalysts, *Ind. Eng. Chem. Prod. Res. Dev.* 12 (1973) 294–301. <https://doi.org/10.1021/i360048a006>.
- [89] M. Li, S.A. Malamis, W. Epling, M.P. Harold, Steady state and lean-rich cycling study of a three-way NO_x storage catalyst: Modeling, *Appl. Catal. B Environ.* 242 (2019) 469–484. <https://doi.org/10.1016/j.apcatb.2018.09.094>.
- [90] D. Di Maio, C. Beatrice, V. Fraioli, S. Golini, F.G. Rutigliano, Development of a Dedicated CNG Three-Way Catalyst Model in 1-D Simulation Platforms, in: 2019: pp. 1–14. <https://doi.org/10.4271/2019-24-0074>.
- [91] G.S. Bugosh, V.G. Easterling, I.A. Rusakova, M.P. Harold, Anomalous steady-state and spatio-temporal features of methane oxidation on Pt/Pd/Al₂O₃ monolith spanning lean and rich conditions, *Appl. Catal. B Environ.* 165 (2015) 68–78. <https://doi.org/10.1016/j.apcatb.2014.09.058>.
- [92] H. Germann, S. Tagliaferri, H.P. Geering, Differences in Pre- and Post-Converter Lambda Sensor Characteristics, in: *SAE Tech. Pap.*, 1996. <https://doi.org/10.4271/960335>.
- [93] T.S. Auckenthaler, C.H. Onder, H.P. Geering, Modelling of a Solid-Electrolyte Oxygen Sensor, in: 2002. <https://doi.org/10.4271/2002-01-1293>.
- [94] J. Bretschneider, Berechnung des Luftverhältnisses von Luft-Kraftstoff-Gemischen und des Einflusses von Messfehlern auf Lambda, *Bosch Tech. Berichte*. 6 (1969) 177–186.
- [95] F. Can, X. Courtois, S. Royer, G. Blanchard, S. Rousseau, D. Duprez, An overview of the production and use of ammonia in NSR + SCR coupled system for NO_x reduction from lean exhaust gas, *Catal. Today*. 197 (2012) 144–154. <https://doi.org/10.1016/j.cattod.2012.07.032>.

- [96] P.A. Carlsson, E. Fridell, M. Skoglundh, Methane oxidation over Pt/Al₂O₃ and Pd/Al₂O₃ catalysts under transient conditions, *Catal. Letters*. 115 (2007) 1–7. <https://doi.org/10.1007/s10562-007-9057-1>.
- [97] D. Bounechada, G. Groppi, P. Forzatti, K. Kallinen, T. Kinnunen, Enhanced methane conversion under periodic operation over a Pd/Rh based TWC in the exhausts from NGVs, *Top. Catal.* 56 (2013) 372–377. <https://doi.org/10.1007/s11244-013-9982-8>.
- [98] X. Wang, R.J. Gorte, A study of steam reforming of hydrocarbon fuels on Pd/ceria, *Appl. Catal. A Gen.* 224 (2002) 209–218. [https://doi.org/10.1016/S0926-860X\(01\)00783-9](https://doi.org/10.1016/S0926-860X(01)00783-9).
- [99] C. Brinkmeier, Automotive three way exhaust aftertreatment under transient conditions: measurements, modeling and simulation, Universität at Stuttgart, 2006. <https://doi.org/http://dx.doi.org/10.18419/opus-1713>.
- [100] M. Bilal, S.D. Jackson, Ethanol steam reforming over Rh and Pt catalysts: effect of temperature and catalyst deactivation, *Catal. Sci. Technol.* 3 (2013) 754–766. <https://doi.org/10.1039/C2CY20703F>.
- [101] Y. Chen, C. Xie, Y. Li, C. Song, T.B. Bolin, Sulfur poisoning mechanism of steam reforming catalysts: an X-ray absorption near edge structure (XANES) spectroscopic study, *Phys. Chem. Chem. Phys.* 12 (2010) 5707. <https://doi.org/10.1039/b925910b>.
- [102] R.B. Duarte, F. Krumeich, J.A. Van Bokhoven, Structure, activity, and stability of atomically dispersed Rh in methane steam reforming, *ACS Catal.* 4 (2014) 1279–1286. <https://doi.org/10.1021/cs400979q>.
- [103] J.M. Zalc, V. Sokolovskii, D.G. Löffler, Are Noble Metal-Based Water–Gas Shift Catalysts Practical for Automotive Fuel Processing?, *J. Catal.* 206 (2002) 169–171. <https://doi.org/10.1006/jcat.2001.3465>.
- [104] Q. Zhang, S. Mo, J. Li, Y. Sun, M. Zhang, P. Chen, M. Fu, J. Wu, L. Chen, D. Ye, In situ DRIFT spectroscopy insights into the reaction mechanism of CO and toluene co-oxidation over Pt-based catalysts, *Catal. Sci. Technol.* 9 (2019) 4538–4551. <https://doi.org/10.1039/C9CY00751B>.
- [105] K. Tanikawa, C. Egawa, Effect of barium addition over palladium catalyst for CO-NO-O₂ reaction, *J. Mol. Catal. A Chem.* 349 (2011) 94–99. <https://doi.org/10.1016/j.molcata.2011.08.025>.
- [106] T. Baidya, P. Bera, Investigation of support effect on CO adsorption and CO + O₂ reaction over Ce_{1-x-y}M_xCu_yO_{2-δ} (M = Zr, Hf and Th) catalysts by in situ DRIFTS, *Catal. Struct. React.* 1 (2015) 110–119. <https://doi.org/10.1179/2055075815Y.0000000004>.
- [107] F. Solymosi, J. Raskó, The effect of chemisorbed oxygen on the stability of NCO on platinum, rhodium and palladium supported by silica, *Appl. Catal.* 10 (1984) 19–25. [https://doi.org/10.1016/0166-9834\(84\)85002-2](https://doi.org/10.1016/0166-9834(84)85002-2).
- [108] S. Chilukoti, F. Gao, B.G. Anderson, J.W.H. Niemantsverdriet, M. Garland, Pure component spectral analysis of surface adsorbed species measured under real conditions. BTEM-DRIFTS study of CO and NO reaction over a Pd/γ-Al₂O₃ catalyst, *Phys. Chem. Chem. Phys.* 10 (2008) 5510. <https://doi.org/10.1039/b806890a>.
- [109] G. Bamos, P. Bika, P. Panagiotopoulou, X.E. Verykios, Reactive adsorption of CO from low CO concentrations streams on the surface of Pd/CeO₂ catalysts, *Appl. Catal. A Gen.* 588 (2019) 117305. <https://doi.org/10.1016/j.apcata.2019.117305>.
- [110] M. Chrzan, D. Chlebda, P. Jodłowski, E. Salomon, A. Kołodziej, A. Gancarczyk, M. Sitarz, J. Łojewska, Towards Methane Combustion Mechanism on Metal Oxides Supported Catalysts: Ceria Supported Palladium Catalysts, *Top. Catal.* 62 (2019) 403–412. <https://doi.org/10.1007/s11244-019-01143-8>.
- [111] F. Solymosi, L. Völgyesi, J. Raskó, The effects of different supports on the formation and reactivity of surface isocyanate on Pd, Ir, Ru and Rh, *Zeitschrift Fur Phys. Chemie.* 120 (1980) 79–87. <https://doi.org/10.1524/zpch.1980.120.1.079>.
- [112] N.M. Martin, M. Skoglundh, G. Smedler, A. Raj, D. Thompsett, P. Velin, F.J. Martinez-Casado, Z. Matej, O. Balmes, P.A. Carlsson, CO Oxidation and Site Speciation for Alloyed Palladium-Platinum Model Catalysts Studied by in Situ FTIR Spectroscopy, *J. Phys. Chem. C* 121 (2017) 26321–26329. <https://doi.org/10.1021/acs.jpcc.7b07611>.
- [113] A. Kaftan, F. Kollhoff, T.-S. Nguyen, L. Piccolo, M. Laurin, J. Libuda, Sensitivity of CO oxidation toward metal oxidation state in ceria-supported catalysts: an operando DRIFTS-MS study, *Catal. Sci. Technol.* 6 (2016) 818–828. <https://doi.org/10.1039/C5CY00827A>.
- [114] A.L. Cámara, M. Monte, A. Martínez-Arias, J.C. Conesa, XPS and DRIFTS operando studies of an inverse CeO₂/CuO WGS catalyst: deactivating role of interfacial carbonates in redox activity, *Catal. Sci. Technol.* 2 (2012) 2436. <https://doi.org/10.1039/c2cy20399e>.

- [115] F.C. Meunier, D. Reid, A. Goguet, S. Shekhtman, C. Hardacre, R. Burch, W. Deng, M. Flytzani-Stephanopoulos, Quantitative analysis of the reactivity of formate species seen by DRIFTS over a Au/Ce(La)O₂ water-gas shift catalyst: First unambiguous evidence of the minority role of formates as reaction intermediates, *J. Catal.* 247 (2007) 277–287. <https://doi.org/10.1016/j.jcat.2007.02.013>.
- [116] F.C. Meunier, D. Tibiletti, A. Goguet, S. Shekhtman, C. Hardacre, R. Burch, On the complexity of the water-gas shift reaction mechanism over a Pt/CeO₂ catalyst: Effect of the temperature on the reactivity of formate surface species studied by operando DRIFT during isotopic transient at chemical steady-state, *Catal. Today*. 126 (2007) 143–147. <https://doi.org/10.1016/j.cattod.2006.10.003>.
- [117] C. Padeste, N.W. Cant, D.L. Trimm, Thermal decomposition of pure and rhodium impregnated cerium(III) carbonate hydrate in different atmospheres, *Catal. Letters*. 24 (1994) 95–105. <https://doi.org/10.1007/BF00807379>.
- [118] M. Wang, P. Dimopoulos Eggenschwiler, T. Franken, D. Ferri, O. Kröcher, Reaction pathways of methane abatement in Pd-Rh three-way catalyst in heavy duty applications: A combined approach based on exhaust analysis, model gas reactor and DRIFTS measurements, *Chem. Eng. J.* 422 (2021) 129932. <https://doi.org/10.1016/j.cej.2021.129932>.
- [119] L.S.F. Feio, C.E. Hori, S. Damyanova, F.B. Noronha, W.H. Cassinelli, C.M.P. Marques, J.M.C. Bueno, The effect of ceria content on the properties of Pd/CeO₂/Al₂O₃ catalysts for steam reforming of methane, *Appl. Catal. A Gen.* 316 (2007) 107–116. <https://doi.org/10.1016/j.apcata.2006.09.032>.
- [120] V. Marchionni, M. Nachttegaal, A. Petrov, O. Kröcher, D. Ferri, Operando XAS study of the influence of CO and NO on methane oxidation by Pd/Al₂O₃, *J. Phys. Conf. Ser.* 712 (2016) 2–6. <https://doi.org/10.1088/1742-6596/712/1/012051>.
- [121] A. Yamaguchi, E. Iglesia, Catalytic activation and reforming of methane on supported palladium clusters, *J. Catal.* 274 (2010) 52–63. <https://doi.org/10.1016/j.jcat.2010.06.001>.
- [122] X. Xu, K. Shuai, B. Xu, Review on Copper and Palladium Based Catalysts for Methanol Steam Reforming to Produce Hydrogen, *Catalysts*. 7 (2017) 183. <https://doi.org/10.3390/catal7060183>.
- [123] R.E. Hayes, S.T. Kolaczowski, P.K.C. Li, S. Awdry, Evaluating the effective diffusivity of methane in the washcoat of a honeycomb monolith, *Appl. Catal. B Environ.* 25 (2000) 93–104. [https://doi.org/10.1016/S0926-3373\(99\)00122-8](https://doi.org/10.1016/S0926-3373(99)00122-8).
- [124] D.N. Tsinoglou, G.C. Koltsakis, J.C. Peyton Jones, Oxygen Storage Modeling in Three-Way Catalytic Converters, *Ind. Eng. Chem. Res.* 41 (2002) 1152–1165. <https://doi.org/10.1021/ie010576c>.
- [125] S.H. Oh, J.E. Carpenter, Role of NO in inhibiting CO oxidation over alumina-supported rhodium, *J. Catal.* 101 (1986) 114–122. [https://doi.org/10.1016/0021-9517\(86\)90234-4](https://doi.org/10.1016/0021-9517(86)90234-4).
- [126] H. Xiong, K. Lester, T. Ressler, R. Schlögl, L.F. Allard, A.K. Datye, Metastable Pd ↔ PdO Structures During High Temperature Methane Oxidation, *Catal. Letters*. 147 (2017) 1095–1103. <https://doi.org/10.1007/s10562-017-2023-7>.
- [127] P. Gélin, M. Primet, Complete oxidation of methane at low temperature over noble metal based catalysts: a review, *Appl. Catal. B Environ.* 39 (2002) 1–37. [https://doi.org/10.1016/S0926-3373\(02\)00076-0](https://doi.org/10.1016/S0926-3373(02)00076-0).
- [128] M. Shelef, G.W. Graham, Why Rhodium in Automotive Three-Way Catalysts?, *Catal. Rev.* 36 (1994) 433–457. <https://doi.org/10.1080/01614949408009468>.
- [129] I. TAVAZZI, A. BERETTA, G. GROPPi, P. FORZATTI, Development of a molecular kinetic scheme for methane partial oxidation over a Rh/α-Al₂O₃ catalyst, *J. Catal.* 241 (2006) 1–13. <https://doi.org/10.1016/j.jcat.2006.03.018>.
- [130] V. Papetti, P. Dimopoulos Eggenschwiler, A. Della Torre, G. Montenegro, A. Onorati, A. Ortona, G. Koltsakis, Stationary heat and mass transfer phenomena in additive manufactured open cell polyhedral structures for automotive catalysis, *Chem. Eng. Sci.* 234 (2021) 116448. <https://doi.org/10.1016/j.ces.2021.116448>.
- [131] S. Roy, M.S. Hegde, S. Sharma, N.P. Lalla, A. Marimuthu, G. Madras, Low temperature NO_x and N₂O reduction by H₂: Mechanism and development of new nano-catalysts, *Appl. Catal. B Environ.* 84 (2008) 341–350. <https://doi.org/10.1016/j.apcatb.2008.04.008>.
- [132] N. Zsiga, M.A. Skopil, M. Wang, D. Klein, P. Soltic, Comparison of Turbocharging and Pressure Wave Supercharging of a Natural Gas Engine for Light Commercial Trucks and Vans, *Energies*. 14 (2021) 5306. <https://doi.org/10.3390/en14175306>.
- [133] J. Pielecha, K. Skobiej, K. Kurtyka, Testing and evaluation of cold-start emissions from a gasoline engine in RDE test at two different ambient temperatures, *Open Eng.* 11 (2021) 425–434. <https://doi.org/10.1515/eng-2021-0047>.

Curriculum Vitae

CONTACT INFORMATION	EMAIL: MOYU.WANG@EMPA.CH PHONE: +41 76 741 3849
PERSONAL INFORMATION	FULL NAME: MOYU WANG DATE OF BIRTH: 22.01.1993
EMPLOYMENT HISTORY	PHD CANDIDATE RESEARCHER <i>EMPA, DÜBENDORF, SWITZERLAND</i> 5/2019 – 07/2022 CFD SIMULATION ENGINEER <i>SEMCON, GÖTEBORG, SWEDEN</i> 10/2018 – 04/2019
EDUCATION	PHD CANDIDATE IN CHEMISTRY AND CHEMICAL ENGINEERING <i>EPF LAUSANNE, LAUSANNE, SWITZERLAND</i> 05/2019 – 07/2022 MASTER IN ENERGY SCIENCE AND TECHNOLOGY <i>ETH ZÜRICH, ZÜRICH, SWITZERLAND</i> 09/2015 – 08/2018 BACHELOR IN ENGINEERING PHYSICS <i>TSINGHUA UNIVERSITY, BEIJING, CHINA</i> 09/2011 – 07/2015